Numerical Damage and Fracture Simulations for Composite Launcher Structures

Using the Building Block Validation Approach

Camille Cheyrou

Technische Universiteit Delft

TU Delft Delft University of Technology

Challenge the future

Numerical Damage and Fracture Simulations for Composite Launcher Structures

Using the Building Block Validation Approach

by

Camille Cheyrou

in partial fulfillment of the requirements for the degree of

Master of Science
in Aerospace Engineering, Structures and Materials

at the Delft University of Technology

Student number:	4621034	
Supervisor:	Dr. ir. J. Fatemi	
Thesis committee:	Dr. S. R. Turteltaub,	TU Delft
	Dr. ir. R. C. Alderliesten,	TU Delft
	Dr. F. Talagani,	Airbus Defence and Space

This thesis is confidential and cannot be made public until December 31, 2023. Op dit verslag is geheimhouding van toepassing tot en met 31 december 2023.

This thesis was supported by Airbus Defence and Space Netherlands B.V. Their cooperation is gratefully acknowledged.

TU Delft Delft University of Technology

AIRBUS DEFENCE & SPACE

ABSTRACT

Furthering the understanding behind Carbon Fiber Reinforced Plastic (CFRP) technology for space launcher applications is one of the objectives of Airbus Defence and Space Netherlands B.V. (ADSNL). The company is in particular designing a composite version of Ariane 6's Vinci engine Thrust Frame (ViTF) and seeks to ensure its structural integrity. This requires that the predictive capabilities of the developed simulations be heavily scrutinized and assessed.

This Master thesis is carried out in order to investigate the Verification and Validation (V&V) of the numerical methodologies which are to be applied to the numerical failure assessment of CFRP composites. In particular, the study focuses on the Hashin intra-ply damage model and the surface-based cohesive inter-ply fracture model. Their performances are examined following a bottom-up Building Block Validation (BBV) approach, which is composed of different levels of calibration and validation of increasing structural complexity. The BBV pyramid developed for this study is based on a set of test results fully provided by Netherlands Aerospace Centre (NLR). It consists of five successive levels in which simulations built in Abaqus/Standard are compared to test data. The first and second levels of the BBV correspond to the Hashin damage model calibration and validation. It uses four independent coupon tests, namely two simple coupons compression tests, an in-plane shear test and an Open-Hole Compression (OHC) test. The fourth and fifth levels are used to calibrate and validate the inter-laminar cohesive surfaces model, using an inter-laminar shear test and the OHC test. The fifth level corresponds to the validation of a complex stiffened panel compression simulation. This study is limited to compressive behaviors. Uncertainty evaluations on the data and the models are excluded.

This approach leads to a successful calibration of the Hashin damage model and gives satisfactory results for the OHC damage simulation. The calibration of the inter-ply fracture model is successful as well using the available test data, however the prediction performances could not be assessed on the OHC test due to convergence issues. The stiffness degradation is too important and requires to use an explicit solver. Finally, the delamination onset prediction obtained for the more complex stiffened panel test is satisfactory. The outcomes of this study show the potential of the BBV approach, while outlining a number of key points. In particular, the test data suitability is proven to be critical in order to increase the confidence of each validation activity. The calibration steps show that a complete input optimization cannot be performed if the experimental tests are not diverse enough. In addition, it is of primary importance for the test set-up to be designed for comparison to analysis, and the BBV approach is not straightforward if the first failure models' validations are performed with a too complex test. This study leads to the proposition of an improved version of the validation process through the recommendation of a set of simple and adapted tests. Further work needs to be carried out in order to perform those tests and include models and test data uncertainties, without which failure model validation cannot be thoroughly assessed.

ACKNOWLEDGEMENT

This Master thesis would never have been possible without all the engineers, researchers, colleagues and friends who supported me in the past months. The period spent working on my project at Airbus Defence and Space was full of challenges and gave me the opportunity to meet incredible people. It concludes seven years of university in France and in the Netherlands of which I will have an indelible memory.

I would like to acknowledge first Javad Fatemi, my main supervisor from TU Delft and Airbus Defence and Space, who made this project possible. He believed in me and guided me through the many steps along the way. Thank you as well to my daily supervisor at Airbus Defence and Space, Farid Talagani, for giving me advice when I needed it the most and for teaching me all the methods which made my project successful. I would like to thank the two other members of the committee, Sergio Turteltaub and Rene Alderliesten without who I could not defend my thesis.

I am very grateful to our colleagues from NLR who provided me with all the experimental results and helped me through their interpretation.

I would also like to thank the other Airbus engineers, Gerard Poort, Finn van der Bas and Henk Cruijssen who helped me during my project and who I had very interesting discussions with.

A special thanks to the international office of my French university ENSTA ParisTech and in particular to Cécile Vigouroux, which offered me to go abroad and gave me the freedom to build my own path.

Furthermore, I must express my profound gratitude to my fellow interns and to the friends who supported me through this journey and with who I have spent an amazing time in the Netherlands. In particular, thank you to Agathe, Filippo and Nicolas who extensively proofread my final report.

Enfin, je remercie ma famille qui m'épaule depuis tant d'années et qui m'a toujours encouragée à viser le meilleur et à être profondément passionnée par ce que je fais. Je ne pourrais pas être celle que je suis sans vous trois.

Camille Cheyrou
Delft, November 2018

CONTENTS

List of Figures

LIST OF TABLES

List of Symbols

Damage Model

α	Coefficient determining the contribution of the shear stress to the fiber tensile initiation criterion
ν_{12}	Poisson ratio
σ_i	Component i of the stress tensor
D	Overall damage variable
D_i	Damage variables for the damage mode i
E_{11}	Longitudinal tensile modulus
E_{22}	Transverse tensile modulus
G_{ij}	Shear modulus in the plane ij
S_L	Longitudinal shear strength
S_T	Transverse shear strength
X_c	Longitudinal compression strength
X_t	Longitudinal tensile strength
Y_c	Transverse compression strength
Y_t	Transverse tensile strength
GC1	Longitudinal compressive fracture toughness
GC2	Transverse compressive fracture toughness
GT1	Longitudinal tensile fracture toughness
GT2	Transverse tensile fracture toughness

Fracture Model

K_{nn}	Normal stiffness coefficient
K_{ss}, K_{tt}	Tangential stiffness coefficients
X_6	Shear contact strength
X_{2t}	Tensile contact strength
G6	Shear fracture toughness
GT2	Transverse tensile fracture toughness

1

INTRODUCTION

1.1. GENERAL BACKGROUND

In the recent years, there has been a startling development of projects aiming to expand the commercial use of space [4]. The concerned markets encompass numerous industries and applications such as navigation, communication, weather and earth observation. The main challenge faced by large-scale space exploration and exploitation are the high costs of both the payload and launch. While cost reduction of the payload is facilitated by modern electronics and satellite miniaturization [5], launch cost reduction can be achieved through weight savings. Reducing the structural mass allows for either a decrease in fuel consumption or for an increase in payload mass. The high specific strength offered by Carbon Fiber Reinforced Plastic (CFRP) makes it an excellent candidate for the development of next-generation space launchers.

CFRPs are a family of laminated materials. They consist of stacked plies of carbon fibers saturated in a polymer matrix. The fibers carry the load by providing strength and stiffness, whilst the matrix bonds the fibers together and provides protection from the environment. The low weight of the matrix combined with the high strength of the fibers gives composite materials their superior lightweight properties. In addition, the assembly cost of such materials is reduced since a strictly limited amount of fasteners are required compared to metallic assemblies.

Unlike metals, CFRPs undergo failure due to an accumulation of damage and fracture which stem from the numerous phases present in the material. This complex failure mechanism includes delamination which occurs between the plies as well as numerous damage mechanisms within each ply. In order to develop safe CFRP structures, it is of primary importance to be able to reliably predict their failure. The fully experimental characterization approach is very expensive and often impractical due to severe mechanical and thermal loads. Moreover, the emergence of Automated Fiber Placement (AFP) technology creates variable stiffness designs of infinite diversity, resulting in unique CFRP components which require their own material characterization campaign [6]. Broad and time-consuming experimental testing would therefore have to be conducted for every components in order to ascertain their allowable strength. This explains why the modern approach coupling virtual and experimental testing is becoming preferable in terms of time and cost reduction.

1.2. FLPP3 PROGRAMME AND ARIANE 6

The European Future Launchers Preparatory Programme 3 (FLPP3) has for objective to cover a large scope of technological development as well as reduce recurring costs and risks for European next generations launchers. Amongst others, the program aims to extend knowledge about CFRP technology through designing, manufacturing and testing.

One of the focal points of the FLPP3 is the Ariane 6 European launcher. This rocket will be the newest member of the Ariane launch vehicle family and is designed to reduce production cost while preserving the reliability achieved with Ariane 5. It will exist in two configurations, with two and four solid rocket motors, in order to address commercial and institutional missions. The majority of the launcher's structure is to this day designed in aluminum.

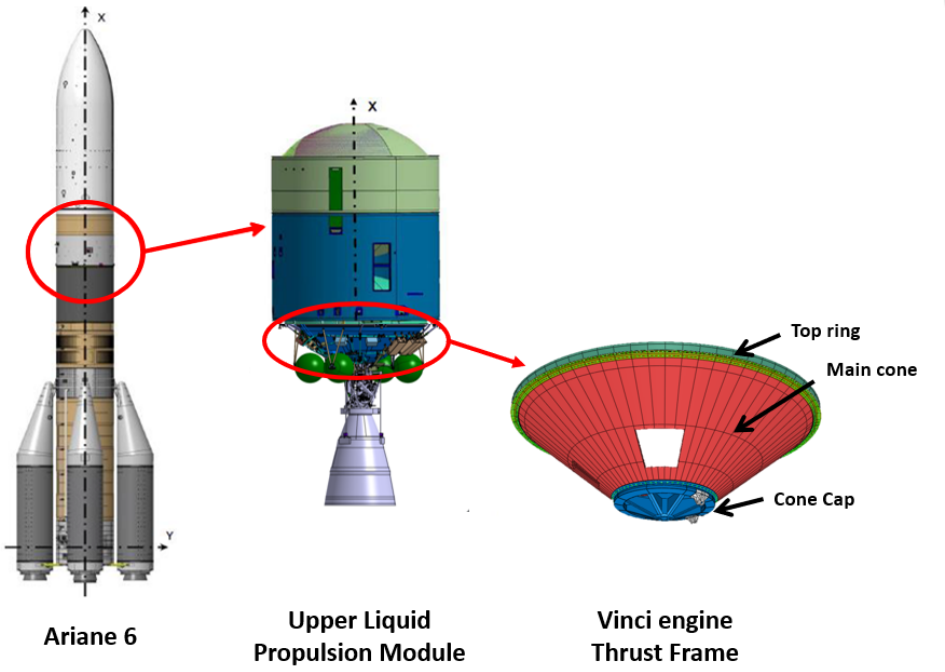

Figure 1.1: Location of the Vinci engine Thrust Frame (ViTF) on the Ariane 6 launcher.

In the frame of FLPP3, Airbus Defence and Space Netherlands B.V. (ADSNL) develops a composite version of Ariane 6's ViTF represented in Figure 1.1. One of the key elements to ensure the reliability of the ViTF is to develop accurate test-validated failure simulations for its CFRP structure. Test-validation is a method ensuring that analytical predictions are validated by test and that test plans are guided by analysis.

1.3. MASTER THESIS OBJECTIVE

This Master thesis is realized as a side project of the FLPP3 program at ADSNL. The main purpose is to investigate the Verification and Validation (V&V) of the numerical methodologies which will be applied for the numerical failure assessment of the laminated composites.

A general guidance for numerical V&V for models in computational solid mechanics was described by the American Society of Mechanical Engineers [2]. Verification is defined as the process of "addressing programming errors and estimating numerical errors", while validation is the "assessment of a model's predictive capability by comparing calculations with experiments". This thesis addresses the validation of numerical models through a structured framework called the Building Block Validation (BBV) approach [7]. The latter starts with experimentation and analysis of small samples to characterize the system while including the necessary activities of model calibration. Calibration of a model is defined as "changing various parts of the model, including the value of model inputs, so that the measured values are matched by equivalent simulated values" [8]. Subsequently, the BBV approach progresses to validate larger simulations of structures and combined loadings. It finally moves towards the validation of complicated sub-components and full-scale components.

A significant amount of failure theories and criteria which could be used in this study have been developed in the past decades. For simplicity, this work focuses on one intra-ply and one inter-ply failure models which are already implemented in Abaqus. The following Master thesis objective is subsequently formulated:

The objective of this Master thesis is to assess the validity of the numerical Hashin intra-ply damage model and surface-based cohesive inter-ply fracture model. This is achieved by performing a calibration and validation procedure, which compares finite element-based failure simulations to experimental test data, as part of a Building Block Validation approach.

All the CFRP material test data necessary for validation is provided by the Netherlands Aerospace Centre

(NLR). The readily implemented intra-ply damage model is based on the Hashin damage initiation criterion, which can be used for plane-stress finite elements. The inter-ply damage model is constituted of a surface-based cohesive model. The thesis work can be divided into the following sub-objectives:

- Build a BBV framework according to the available test data.
- Create finite-element failure simulations corresponding to the available experimental tests.
- Perform the consecutive activities of model verification, calibration and validation as prescribed by the defined BBV framework.
- Present quantitative and qualitative final validation results, followed by recommendations in order to propose an optimized failure model validation approach.

The presented objectives have the following restrictions in order to ensure they are achievable in the frame of a Master thesis:

- A single type of composite laminate is studied.
- The analyses do not take into account thermal loading.
- The validation steps take as sole input the test data provided by the NLR at the beginning of the study. Since all the data concerns compressive load cases, the scope of the numerical validation is restricted to compressive behavior.
- There is no stochastic or scatter consideration in the developed simulations and test data, which are henceforth deterministic.
- The numerical simulations are all implemented in Abaqus/Standard. Due to time and resource limitations, the use of Abaqus/Explicit is excluded.

1.4. THESIS LAYOUT

In order to fulfill the research sub-objectives, the thesis layout is presented as follows. Chapter 2 introduces the verification, calibration and validation approach. It presents the general BBV pyramid as well as the activities to be performed in each level of validation. These concepts are used to formulate the BBV scheme used in this study. The activities are divided in five main levels which are each performed in a separate chapter. Chapters 3 and 4 develop the calibration and validation of the intra-ply Hashin damage model, starting from input material data found in data-sheets and literature. Chapters 5 and 6 present the calibration and validation of the inter-ply fracture model based on cohesive surfaces. The BBV activities end in chapter 7 with the validation of a complex sub-assembly. It corresponds to a stiffened panel compression test, for which delamination is simulated using the inter-ply fracture model. From chapters 3 to 7, conclusions and specific remarks are progressively formulated concerning the necessary test setups and simulation procedures which would create a time-efficient, straightforward validation method. The final global conclusion and recommendations are provided in chapter 8.

A literature review was separately written which introduces the concepts of damage and fracture mechanics as well as the principles of failure simulations [9].

2

VALIDATION METHODOLOGY FOR NUMERICAL DAMAGE MODELS

Chapter 2 describes the methodology developed to assess the validity of the chosen numerical failure models. In section 2.1, the general principles of the BBV approach are presented for Solid Mechanics applications. Before defining the validation scheme for this study, the two considered failure models are presented in section 2.2. Section 2.3 details the steps of the BBV approach built for the two failure models, based on the available experimental data-set. Finally, the activities which will be repeated for each level of the selected validation procedure are presented in section 2.4.

2.1. BUILDING BLOCK VALIDATION APPROACH IN SOLID MECHANICS

In order to rely on the results obtained by numerical models, following a V&V procedure is fundamental. Structuring of V&V for Solid Mechanics models started a decade ago [2]. In particular, the procedure known as "certification by analysis supported by test evidence" is used by the large commercial transport aircraft industry to demonstrate compliance with regulatory agencies requirements [1]. It provides guidance for evaluating margins of safety concerning static strength, durability and damage tolerance of composite materials. This process is otherwise known as the BBV approach. More than just providing with a quantified model accuracy, this scheme optimizes as well the necessary experimental resources by ensuring that analytical predictions are validated by test and test plans are guided by analysis. It results in a time-efficient, cost-effective way of validating numerical models for complex simulations. This section describes the progression through a general BBV procedure, followed by the description of activities typically included in one specific BBV level.

2.1.1. GENERAL BBV PYRAMID

The validation process is composed of analyses and associated tests at several levels of structural complexity. It begins with small coupons and progresses through structural elements, sub-components, and finally the complete full-scale product. This principle is represented in Figure 2.1. Progressing upward on the pyramid, specimen complexity and cost increase, as well as the degree of specificity of the test, but the number of tests decreases.

The pyramid starts with the gathering of simple coupon tests in order to generate the material properties. Subsequently, analysis methods are calibrated by adjusting some modeling parameters. This is done by fitting the simulated behaviors to the experimental results. At the higher levels of the pyramid, tests of sub-component or full-scale components are used exclusively to validate the numerical models previously calibrated. Finally, the validated models can be used for predictions on new, intended complex loading cases. The whole BBV process is always performed within a scope of application, which means that the final validated models are only valid in the frame of their intended use.

2.1.2. TYPICAL ACTIVITIES PERFORMED IN THE STAGES OF A BBV APPROACH

Each level of the BBV pyramid is composed of a repetitive series of activities. Experimental testing is performed in parallel of mathematical modeling and numerical implementation, leading to the final calibration

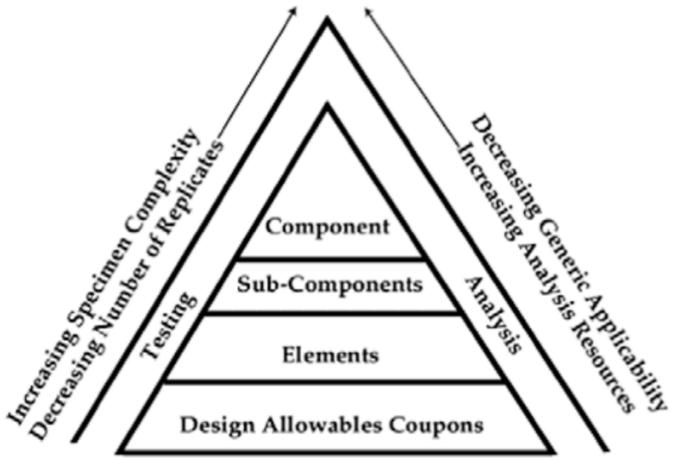

Figure 2.1: General BBV approach [1].

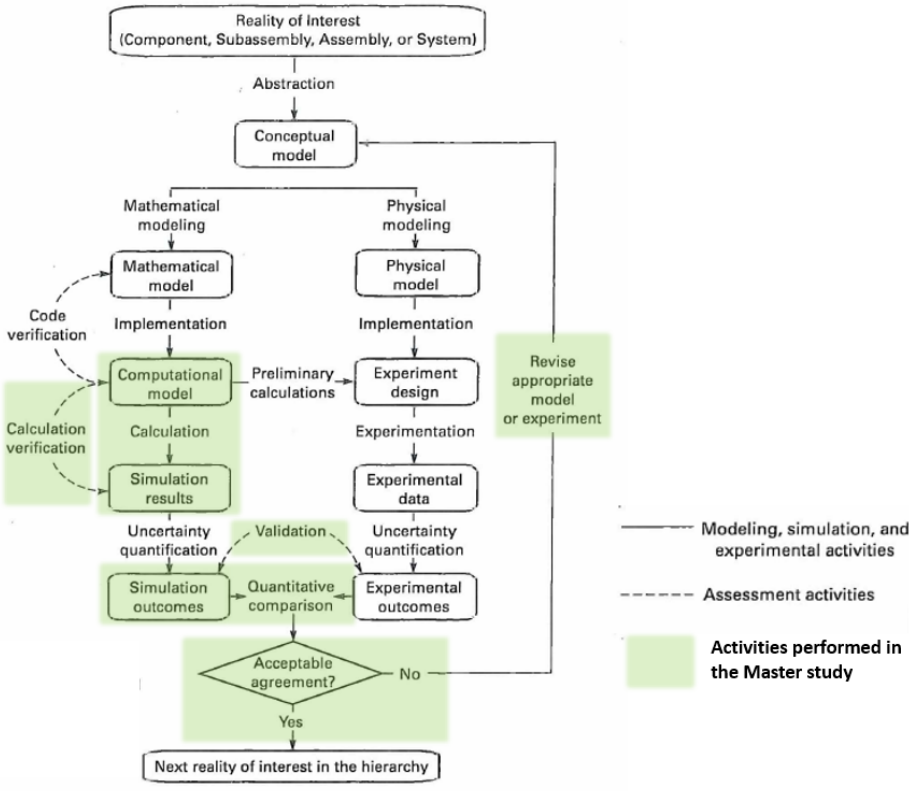

Figure 2.2: General activities and products of the V&V approach [2], together with the set of activities included in this Master thesis.

or validation activity. A detailed scheme of this procedure is shown in Figure 2.2 in the case of a validation step. In the present Master thesis, solely a part of these activities are performed and the rest of the information is provided by other parties. It is emphasized that each numerical model developed for this procedure must be subject to a verification before performing the calibration or validation activities. In addition, a meaningful validation must address uncertainties arising from both experimental and computational procedures [2].

In the present case, two types of damage and fracture numerical models are subject to validation. The first one is the Hashin model used to model intra-ply damage and the second represents inter-ply fracture through the use of cohesive surfaces. These models are described in the next section.

2.2. DAMAGE AND FRACTURE MODELS OF INTEREST

This section describes the two intra- and inter-ply damage and fracture models which are subject to the current BBV approach. The onset, propagation and stabilization of damage as they are implemented in Abaqus are detailed below. The information of this section is provided in the Abaqus Analysis User's Manual [10]. The subscripts "1" "2" and "3" correspond to the fiber direction and the two transverse directions, respectively. The names of the parameters cited throughout this section are given in Table A.1.

2.2.1. INTRA-PLY DAMAGE MODEL

The considered intra-ply damage model is implemented in Abaqus for elastic-brittle materials with anisotropic behavior. It is used in order to predict the onset and propagation of damage within a ply of composite material. The model is composed of three distinct modules: the undamaged linear-elastic response of the material, the damage initiation criterion and the damage evolution response.

ELASTIC BEHAVIOR

First, the undamaged linear response of the material has to be defined through a series of inputs. In the case of transversely isotropic materials such as fiber-reinforced composites, the following constants are required for plane-stress elements: E_{11}, E_{22},ν_{12}, G_{12}, G_{13}, G_{23}. The last two constants are required to model transverse shear deformations. In order to use solid elements, constants for orthotropic materials are necessary: E_{11}, E_{22}, E_{33}, ν_{12}, ν_{13}, ν_{23}, G_{12}, G_{13}, G_{23}.

ONSET OF DAMAGE

Damage initiation refers to the onset of degradation at a material point. The damage initiation criterion is based on Hashin's theory [11], [12]. This type of theory distinguishes between fiber and matrix failure modes, while using stress interaction terms. Four modes of damage initiation are taken into account: Fiber Tension (FT), Fiber Compression (FC), Matrix Tension (MT) and Matrix Compression (MC). The initiation onset is predicted in this study by the 1973 Hashin-Rotem criterion. Noting σ_i the stress component in direction i in a ply, T the tension and C the compression, the criterion is formulated as indicated in Table 2.1.

Failure mode	FT damage ($\sigma_1 > 0$)	FC damage ($\sigma_1 < 0$)	MT damage ($\sigma_2 > 0$)	MC damage ($\sigma_2 < 0$)
Criterion	$\sigma_1 = \sigma^u_{1T}$	$-\sigma_1 = \sigma^u_{1C}$	$\left(\frac{\sigma_2}{\sigma^u_{2T}}\right)^2 + \left(\frac{\sigma_{12}}{\sigma^u_{12}}\right)^2 = 1$	$\left(\frac{\sigma_2}{\sigma^u_{2C}}\right)^2 + \left(\frac{\sigma_{12}}{\sigma^u_{12}}\right)^2 = 1$

Table 2.1: Hashin-Rotem failure criterion.

The six strength inputs required in Abaqus to apply the initiation criterion are: X_t, X_c, Y_t, Y_c, S_L, S_T. Additionally, the parameter α determines in Abaqus the contribution of the shear stress to the fiber tensile initiation criterion. It has to be set to 0 in order to obtain the above-mentioned initiation criterion. This choice sets $S_T = Y_c/2$. The four Abaqus outputs for the damage initiation parameters are listed in Table B.1. It is important to note that this criterion can only be used with plane-stress elements.

DAMAGE PROPAGATION

Damage evolution is based on the assumption of a progressive degradation of material stiffness, leading to material failure. Throughout the damage evolution analysis, a set of damage variables D_i, which reflects the state of damage is each point for each damage mode, is updated. The D_i evolve such that the stress-displacement curve follows a a type of law called Traction-Separation Law (TSL). The stiffness matrix depends on the D_i and gets updated accordingly to the state of damage. Only bilinear TSL are used is this study and it is represented in Figure 2.3. The downward slope of the graph indicates a softening behavior once the damage criterion is met. The fracture process is completed when the traction reaches the value 0, which means as well $D_i = 1$. During unloading, the traction follows the line 0-B and D_i stays constant. The softening section of this law for each damage mode depends on the fracture toughness inputs GT1, GC1, GT2 and GC2. An element is finally removed from the analysis when damage variables for all failure modes at all material points reach 1. The four Abaqus damage variables outputs are listed in Table B.1.

Additionally, a viscous regularization can be added to the analysis in order to overcome the convergence difficulties. Such issues are very common for material models exhibiting stiffness degradation. With the

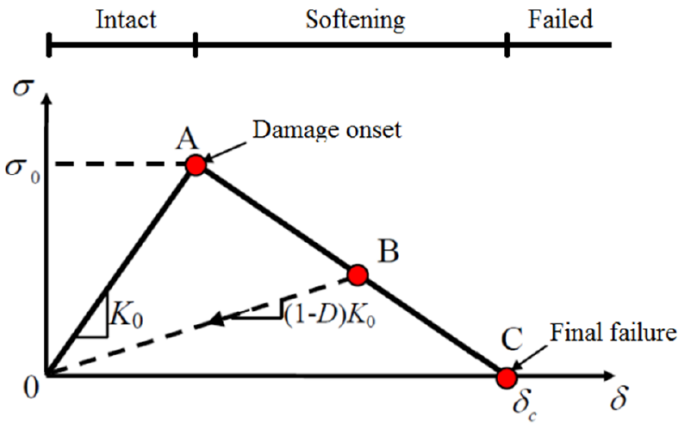

Figure 2.3: Illustration of the traction-separation bilinear law [3].

viscous regularization, a viscosity coefficient representing the relaxation time of the viscous system is added to the damage variables formulation. Therefore, the tangent stiffness matrix of the softening material is kept positive for sufficiently small time increments. The energy dissipated by viscous regularization ALLCD should remain small compared to the internal energy ALLIE, see Table B.1.

2.2.2. INTER-PLY DAMAGE MODEL

The inter-ply delamination model is implemented in Abaqus using a traction-separation behavior between two surfaces. It is intended to predict the onset and propagation of damage between two plies of composite material. As with the intra-ply damage model, the surface-based cohesive behavior is composed of three distinct modules: the initial linear-elastic response of the material, the fracture initiation criterion and the damage evolution response.

COHESIVE SURFACES

The cohesive surface interactions in Abaqus correspond to surface interaction properties that are assigned to a contact pair. Delamination is only evaluated at the interface between the two surfaces that are initially defined in contact. It is important to recognize that surface-based cohesive behavior is an interactive property and not a material one. Therefore, compared to a traditional material traction-separation law, separation is reinterpreted as the distance between the two surfaces, while stresses are based on the cohesive forces acting along the contact.

ELASTIC BEHAVIOR

Prior to damage, a linear elastic law is assumed between the two surfaces. The constitutive matrix is elastic and relates the normal and shear stresses to the normal and shear separations across the interface. In this study, the parameters describing the linear behavior are the uncoupled stiffness coefficients K_{nn}, K_{ss} and K_{tt}, which are either automatically calculated by the software or inputed by hand.

ONSET OF FRACTURE

The delamination is chosen to corresponds to a simple maximum stress criterion. This means that damage is assumed to initiate when the maximum normal or shear contact stress reaches the defined contact strength. The necessary inputs are X_{2t} and X_6. The Abaqus output for the damage initiation parameter is described in Table B.1.

FRACTURE PROPAGATION

Once damage initiates at the interface, failure of the cohesive bond is characterized by progressive degradation of the cohesive stiffness. An overall damage variable D corresponds to the total damage at a contact point. The evolution of that variable follows a bilinear TSL as presented in subsection 2.2.1. Additionally, the final failure of an element is chosen to be defined by fracture energy inputs GT2 and G6. This means that Abaqus ensures that the area under of the damaged response linear traction-separation law is equal to the

total fracture energy. Since the critical fracture energies along the first and the second shear directions are the same, the Benzeggagh-Kenane rule can be applied to calculate the total fracture energy. The expression of this energy is provided below [13]

$$G_n^C + (G_s^C - G_n^C)\left\{\frac{G_S}{G_T}\right\}^{\eta} = G^C, \quad G_S = G_s + G_t, \quad G_T = G_n + G_S \tag{2.1}$$

where η is a cohesive property parameter and G_n, G_s, G_t are the normal and shear contact fracture energies. The superscript C designates the critical energies values, which are input by the user. In the current case, $G_n^C = GT2$, $G_s^C = G_t^C = G6$. The cohesive property parameter η is fixed at the value of 1.45 throughout the study [6]. Once D reaches 1 at a node, no further cohesive constraints apply. Normal and shear contact behaviors are then enforced at the node. The Abaqus output for the overall damage variable is described in Table B.1.

Additionally, a viscous regularization can be defined for the cohesive surfaces. The purpose and mechanism of this regularization is the same as in subsection 2.2.1. The calibration and validation procedure which is built for the two failure models is described in the next section.

2.3. BBV PYRAMID FOR THE CONSIDERED FAILURE MODELS

The general structure of the BBV approach that is chosen for this study is developed in this section. It depends mainly on the available set of test data, which is presented in subsection 2.3.1. The construction of the BBV pyramid is described in subsection 2.3.2.

2.3.1. AVAILABLE SET OF TESTS

The material considered for this master thesis is a type of CFRP composed of a toughened epoxy resin and continuous, high performance, intermediate modulus carbon fibers. This material is of particular interest in the aerospace industry due to its good resistance against micro-cracking and good properties at low temperatures, which enables it to be used around the cryogenic tank of Ariane 6. The initial material data used for the calibration of the damage and delamination models are partially provided by the manufacturer and are summed up in Table A.1. Additional values are necessary, but as no information was communicated by the manufacturer, they were found in literature for similar materials.

A simple summary of the test results available for the validation process is provided in Table 2.2, together with their given names. NLR performed the integrality of these tests. The details of the test set-ups and results are provided in the following chapters.

Test	Test name	Description in	Available data
0° compression	Test 1	Section 3.1.1	Stress/strain curve
90° compression	Test 2	Section 3.1.2	Stress/strain curve
IPS	Test 3	Section 3.1.3	Load/shear strain curve
0° OHC	Test 4	Section 4.1	Load/displacement curve
ILS	Test 5	Section 5.1	Load/displacement curve
Stiffened panel compression	Test 6	Section 7.1	LVDT, strain gauges curves
			Aramis displacement fields
			Visual inspection

Table 2.2: Summary of the test data used in the BBV approach. All the tests are performed at ambient temperature. No uncertainty assessment is provided with the test results.

2.3.2. CONSTRUCTION OF THE BBV APPROACH

Each level of the pyramid should correspond either to the calibration or the validation of one failure model. As explained in section 2.1, the calibration levels require numerous different tests in order to calibrate each one of the numerical model's parameters. On the other hand, the validation levels imply to evaluate to what extent simulations effectively match experimental data for fewer, more complex tests.

Since there is one damage model and one independent fracture model to calibrate and which performance has to be assessed, at least four levels are required in the current approach. The fifth level corresponds to the simulation of a sub-assembly, which is expected to accurately correspond to test results if the calibration process was performed correctly. A summary of the different levels and their purpose is given in Table 2.3. The manner in which test data is divided between the levels is presented in the next paragraph.

Levels	Purpose	Test data from
Level 1	Hashin intra-ply damage model calibration	Test 1, 2, 3
Level 2	Hashin intra-ply damage model validation	Test 4
Level 3	Cohesive surfaces inter-ply fracture model calibration	Test 5
Level 4	Cohesive surfaces inter-ply fracture model validation	Test 4
Level 5	Cohesive surfaces model validation at a structural level	Test 6

Table 2.3: Summary of the five levels used in the current BBV approach.

The repartition of the different tests among the BBV pyramid levels is done according to the following logic:

- Test 5 is the only one which shows a single failure mode, namely delamination. It is easier to calibrate a failure model when using test data which shows unmixed failure modes. Therefore, test 5 is used for level 3.
- Tests 1, 2 and 3 are the three simplest samples available. The longitudinal and transverse compression tests are expected to have fiber- and matrix-dominated behaviors, respectively. Test 3, on the other hand, is meant to show the in-plane shear behavior of the material. These tests therefore appear to be relatively independent and cover the three main behaviors of a fiber-reinforced material. They are assigned to level 1.
- Test 4 is complex because of the presence of a central hole and the number of plies stacked together. The stress concentrations present at the hole during compression generate a three-dimensional response. Both delamination and intra-ply damage are observed on the final specimen. This test has to be used for level 2 and level 4 due to the lack of test data. This choice makes the validation approaches more complex: only the intra-ply damage model is included in simulations of level 2, even if delamination is present in the experimental test. This implies an unavoidable behavior mismatch during level 2. On the other hand, both damage and fracture models can be included during level 4 simulation and represent more accurately the test results. However, two difficulties arise: first, the cohesive surfaces performance cannot be validated independently from the intra-ply damage model. Second, a revision of the level 1 calibration may be necessary if important discrepancies between simulation and test are observed in level 4.
- Test 6 is a panel-level test, which can be used to validate complex numerical simulations once the damage and fracture models are validated. The observed failure mode corresponds to delamination of stringers from skin at the stringers run-out. Therefore, test 6 is used in level 5, with the objective to validate a simulation using the cohesive surfaces.

The distribution of the different tests are listed in Table 2.3 and represented in Figure 2.4. The available test data integrally corresponds to compression testing. Therefore, the scope of the current validation approach is limited to the prediction of intra- and inter-ply damage for laminated parts composed of the current CFRP, under compression testing. Since no uncertainty assessment is provided with the test results, the accuracy evaluation expected at the end of the validation process cannot be fully performed. Simple indications will be given on the final predictions errors of each model. The focus of this study is additionally to go through the BBV approach as much as the available test data permits it and identify the critical aspects of the procedure, while pointing out the limits of the data-set. The next section presents, in a general manner, the series of activities conducted in each level of the current BBV approach.

2.4. ACTIVITIES PERFORMED IN THE CURRENT BBV CONTEXT

This section describes the procedure used in each level of the BBV approach, from the pre-processing to the post-processing phases. Not all the activities usually performed during a V&V procedure are done in this

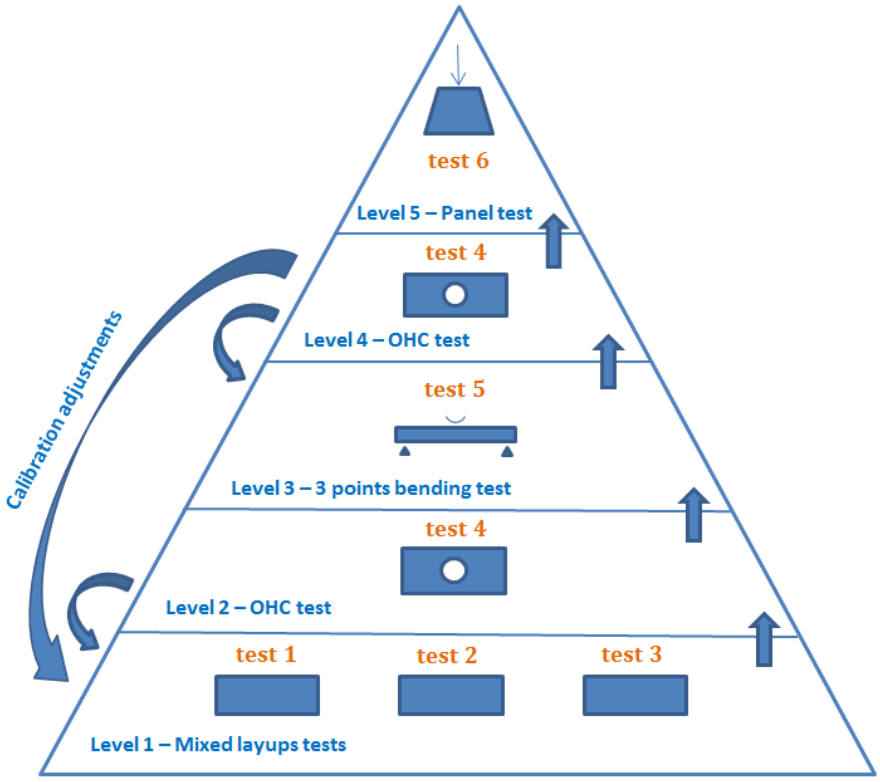

Figure 2.4: BBV pyramid used in this study for the validation of failure models.

study, as pointed out in Figure 2.2. A summary of the sequence of activities included in the frame of this Master thesis is represented in Figure 2.5. It is described as following:

- For each level of the pyramid, the first activity is to gather a number of inputs listed in Figure 2.5. The material data either comes from Table A.1 or from the calibrated/validated values chosen in the previous level. Subsequently, the first model is built. This constitutes most of the pre-processing phase. The models are built in Abaqus/Standard 2016.

- Once the first version of the numerical model is built, it has to be verified through a series of simulations. This necessitates the modification of certain parameters such as the mesh density until the model behaves as expected. For example, it involves checking that the mesh density is low enough to have a converged behavior. Before each validation simulation, a few parameters are modified, which corresponds to a pre-processing activity. Afterwards, looking at the output and assessing the validity of the numerical response constitutes a post-processing activity.

- Finally, the verified model is used to produce results comparable to the available test data. This corresponds either to the calibration or validation activity, which is the final post-processing phase. A metric or criterion has to be used to judge the validity of the simulations. As stated in the previous subsection, the accuracy cannot be precisely evaluated in the current context. Simple metrics are used in this study and they only aim to give an indication about the accuracy achievable with a model. The used metrics are mainly the error percentage in stiffness and final strength between simulations and tests. The indicative allowable error is based on the estimated uncertainties in the model and in the tests. In the current case, the experimental curves do not include scatter, and the simulations are deterministic. An order of idea of the experimental scatter on strength is based on results provided by NLR, which repeated the experiments only 5 to 6 times in each case: tests 1, 2 and 4 have a deviation in strength of 5% with respect to the mean value. The deviation is 7% for test 5. When a calibration or a validation in performed in this report, the metric therefore takes into account this variability in experimental results. This leads to the indicative, general strength allowable error of 10% for tests 1, 2, 4 and 5.

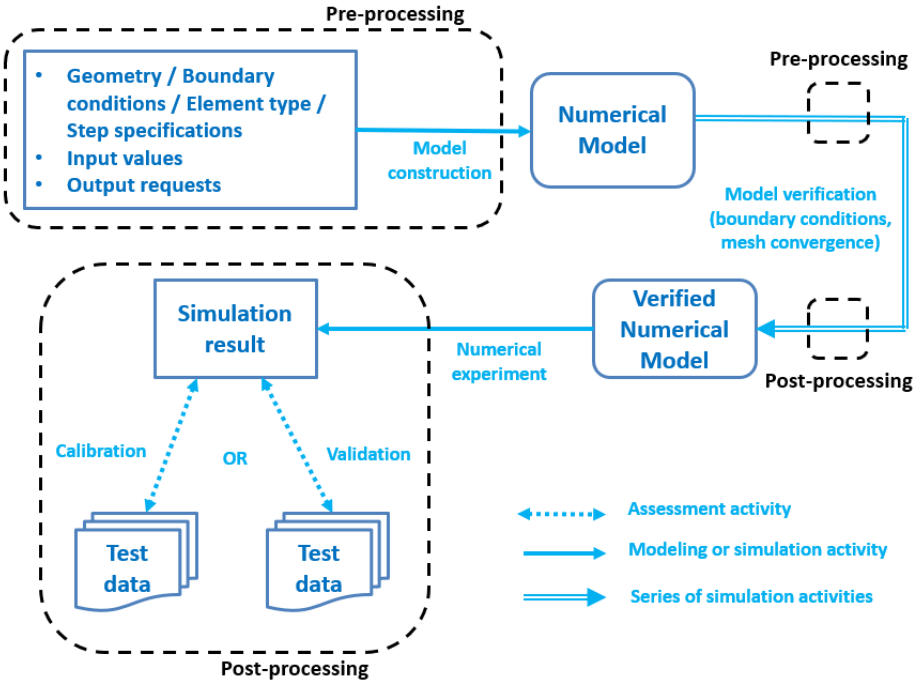

Figure 2.5: Activities involved in this study when performing a level of validation or calibration. The input material data either comes from literature or from the previous BBV level.

- If the validation is confirmed, the activities are over for the current level and progression can be made to the next level. Otherwise, a modification of the model or test set-up has to be performed. If this is not successful, it is necessary to review the previous calibration steps of the BBV pyramid. The validation tests can be failed for three reasons: the model is too simple compared to reality, the solution of the simulation model differs dramatically from the ideal solution, calibration of the input values is not accurate enough or the real system was not tested correctly [14].

The simulations are all started and post-processed by hand. That is because the current failure BBV process is new. Therefore, it is important to understand the sensitivity of the designed simulation results to the inputs, specifically to the damage and fracture models parameters. Another option during calibration would be to build an automated optimization algorithm which would find the set of material parameters leading to the best curve fit. However, this solution would not allow any insight into the dependency between the different tests. With the chosen method at all steps during the BBV approach, the effects of poor modelization can be segregated from the effects of poor calibration. A deep understanding of the damage and failure models specificities is thereby obtained.

Following the context and validation approach defined for this study, the next five chapters contain the test data, models and calibration or validation of each level of the BBV pyramid.

3

Level One: Calibration of the Damage Model

This chapter describes the process of calibration corresponding to level 1 of the BBV approach presented in section 2.3. The purpose of this level is to optimize the Hashin damage model inputs in Abaqus by ensuring that the simulation results correspond to the experimental data provided by NLR. Section 3.1 presents the experimental tests and results which are made available for this thesis study. The corresponding numerical models are given in section 3.2, followed by the description of the calibration process in section 3.3. Finally, a conclusion is given in section 3.4 and recommendations are given in section 3.5.

3.1. Level One Test Data

The set of tests to be used for the first level of the BBV approach are tests 1, 2 and 3 listed in table 2.2. Their final response curves are used for the calibration procedure. Because of slipping of the specimens in their tabs when the test is initiated, the load-strain or load-displacement curves include an initial non-linear strain or displacement. Since this effect does not provide any useful information and is not to be modeled in the finite elements analyses, the data curves are linearly extrapolated to remove that effect.

3.1.1. Data for Test One: Longitudinal Compression Test

The first available test for damage calibration is referred to as test 1. It is a 0° compression test with layup $[0/+45/0/-45]_{4S}$, named ETF layup. Dimensions of the test sample are given in Figure 3.1, with the reference coordinates A. The test is conducted using the ASTM D3410-03 standard [15], with a NASA short block compression test fixture [16]. The area in contact with the fixture is represented in the figure in brown. The lateral tabs do not clamp firmly the specimen, as defined for this test fixture [15]. The tests are performed in a 300kN Instron test machine, under displacement rate control.

The stress-strain curve which is available for test 1 comes from the measurements made by an extensometer attached to the fixed and the movable parts of the test bench as represented in Figure 3.1. The load cell indicates the total force being resisted by the test specimen. Both displacements and forces are measured in the longitudinal direction (axis x). Stresses and strains are derived by dividing the force by the specimen cross-sectional area and dividing the displacement by the specimen length, respectively. The linearly extrapolated result curve is given in Figure 3.2.

3.1.2. Data for Test Two: Transverse Compression Test

The second available test, called test 2, corresponds to the exact same test procedure as test 1, with a material orientation pivoted by 90°. The dimensions and orientations are represented in Figure 3.1, with the reference coordinates B. The linearly extrapolated result curve is given in Figure 3.3. An example of 90° compression specimen after testing is shown in Figure 3.4. For this study, the observed delamination is assumed to occur after reaching the maximum load.

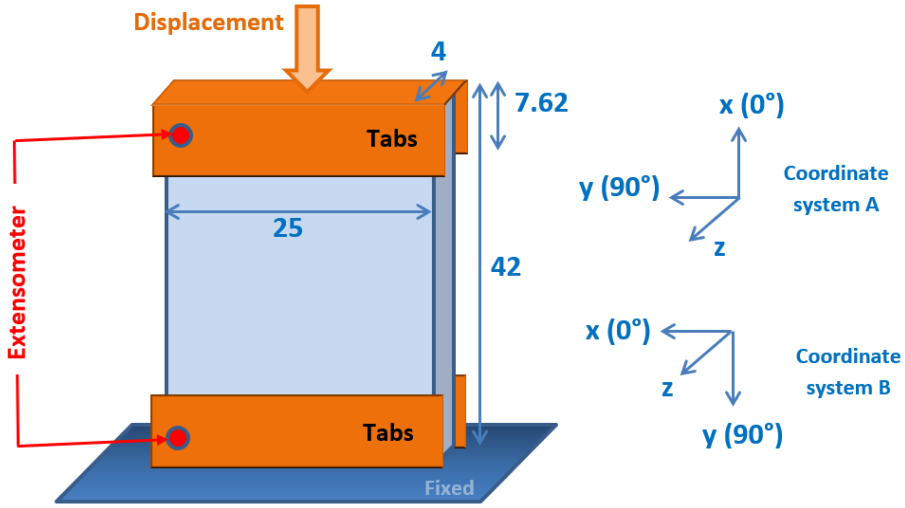

Figure 3.1: Experimental setup of the 0º and 90º compression tests, lengths are in mm.

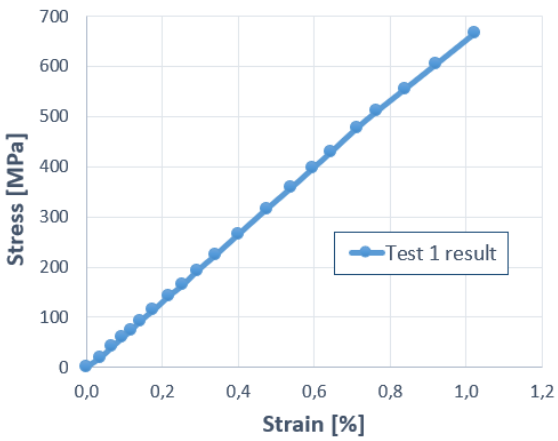

Figure 3.2: Stress-strain curve of the 0º compression test, extrapolated at the origin.

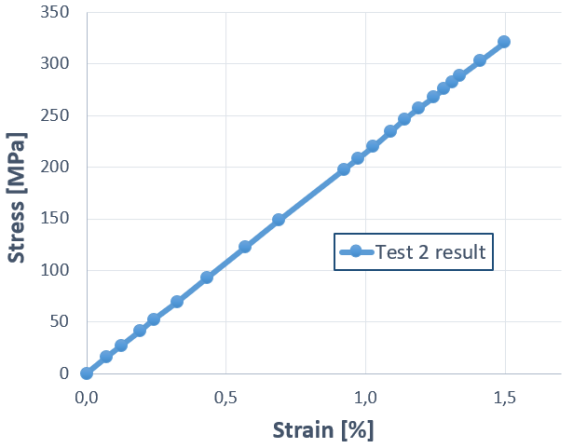

Figure 3.3: Stress-strain curve of the 90º compression test, extrapolated at the origin.

3.1.3. DATA FOR TEST THREE: IN-PLANE SHEAR TEST

Test 3 is the last available test. It is an IPS test carried out according to the standard ASTM D3518 [17]. This 0° tension test is performed with the layup $[+45/-45]_{4S}$. Dimensions of the sample are given in Figure 3.6, where the area in contact with the fixture is represented in brown. The tests are performed in a 100 kN Instron test machine, under displacement rate control.

The longitudinal deformation is measured with a 50 mm MTS extensometer and the transverse deformation is measured with a 25 mm clip gauge. The measurement points on the sample are represented in Figure 3.6. Two strains are deduced by dividing the deformation by the corresponding original dimension of the specimen: ϵ_1 in longitudinal direction and ϵ_2 in transverse direction. Finally, the specimen shear strain is calculated with the formula $\gamma = \epsilon_1 - \epsilon_2$. The load signal is measured by the load cell included in the machine and the shear strain yield the experimental curve given in Figure 3.7. ASTM D3518 advises not to look at strains further than 5%, after which fiber scissoring would violate the assumption that the fibers are oriented at 45° [17]. An example of IPS specimen after testing is shown in Figure 3.5. The numerical models created to simulate the three tests are described in the next section.

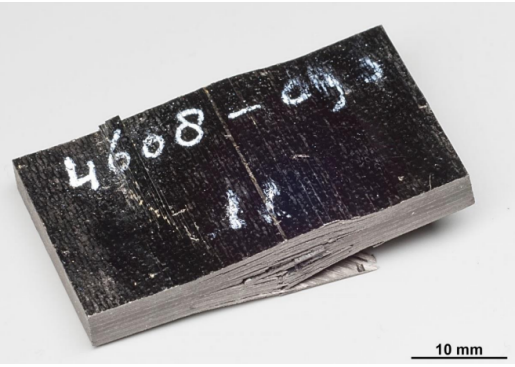

Figure 3.4: Example of 90º compression specimen after testing.

Figure 3.5: In-Plane Shear (IPS) specimen after testing.

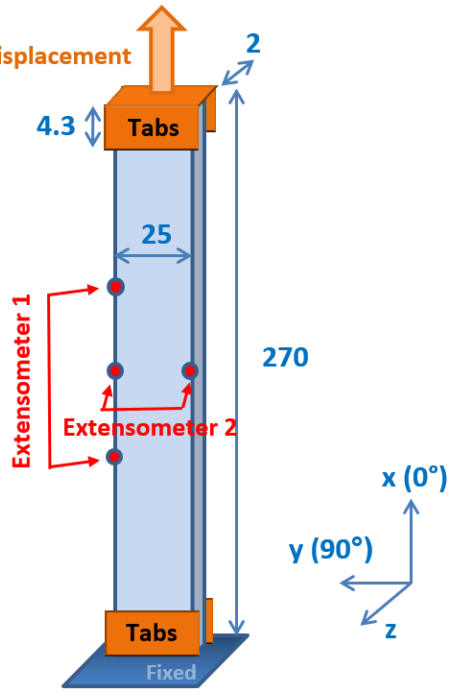

Figure 3.6: Experimental setup of the IPS test, lengths are in mm.

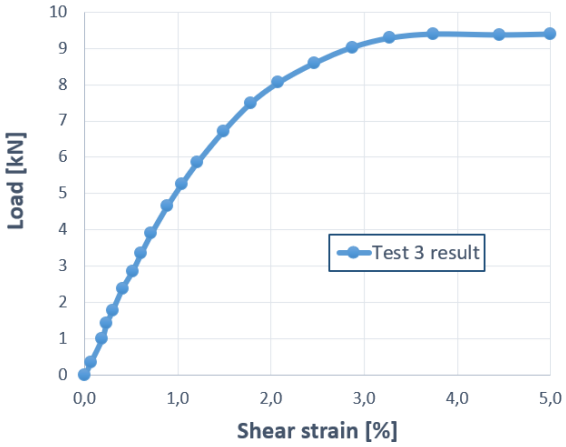

Figure 3.7: Load-strain curve of the IPS test, truncated at 5% strain.

Model	Region	Motion
Test 1 Figure 3.8, coordinate system A	Surfaces A and B	$U_z = 0$
	Edge C	U_x applied (<0)
	Edge D	$U_x = 0$
	Point E	$U_y = 0$
Test 2 Figure 3.8, coordinate system B	Surfaces A and B	$U_z = 0$
	Edge C	U_y applied (>0)
	Edge D	$U_y = 0$
	Point E	$U_y = 0$
Test 3 Figure 3.9	Surface A	U_x applied (>0) Other motions fixed
	Surface B	All motions fixed

Table 3.1: Summary of the boundary conditions and displacements applied to the models of tests 1, 2 and 3, together with the reference figures defining the different regions and orientations. U designates a translational degree of freedom.

3.2. NUMERICAL MODELS FOR LEVEL ONE TESTS

In order to perform the Hashin damage model calibration, the three numerical models corresponding to tests 1, 2 and 3 are developed using the Finite Elements Method (FEM). All the simulations are displacement-controlled and take as inputs the parameters listed under "Damage model initial inputs" of Table A.1.

3.2.1. TEST ONE AND TEST TWO NUMERICAL MODELS

The two numerical models developed in this subsection correspond to the longitudinal and transverse compression tests whose test set-ups are described in subsections 3.1.1 and 3.1.2.

GEOMETRY AND ELEMENTS

Test 1 and test 2 definitions differ only in their material orientation, as explained in section 3.1. The coupon dimensions of Figure 3.1 are used for the numerical model. In order to use the Hashin damage module, the choice of finite element has to be made between conventional shells, continuum shells, or membranes. In the present case, membrane elements are not suitable. Since the samples geometries are very simple, the traditional conventional shell elements are used. The composite layup is defined in a single section of shell elements, using Abaqus composite modeller.

With these two models, the output stress is obtained by taking the total vertical reaction force on edge C and dividing by the laminate's cross-sectional area. The strain is obtained by looking at the vertical displacement of one node on edge C and dividing by the initial length of the specimen.

BOUNDARY CONDITIONS

The boundary conditions have to reproduce the testing conditions. Using the conventions of Figure 3.1, with the reference coordinates A, the NASA short block fixture imposes the displacement in the x-direction to be zero for the bottom part of sample, whereas a negative displacement is applied to the upper part of the sample. This type of fixture does not completely clamp the specimen in the y and z directions, which is why the best equivalent boundary conditions are those represented in Figure 3.8 and summarized in Table 3.1. These boundary conditions are demonstrated in section 3.3 to give satisfactory results.

MESH DEPENDENCY

The mesh applied to the test 1 and test 2 models should be fine enough to give converged results, while it should be as coarse as possible to remain computationally efficient. Three simulations are run with elements of size 0.8 mm, 0.5 mm and 0.3 mm, and no difference in the resulting stress-strain curves is observed. It is concluded that for the numerical models of test 1 and 2, the simulations are not mesh-sensitive. The final mesh for performing the calibration is chosen to be 0.8 mm. This mesh is represented in Figure 3.8.

3.2.2. TEST THREE NUMERICAL MODEL

This numerical model corresponds to the IPS experiment described in subsection 3.1.3.

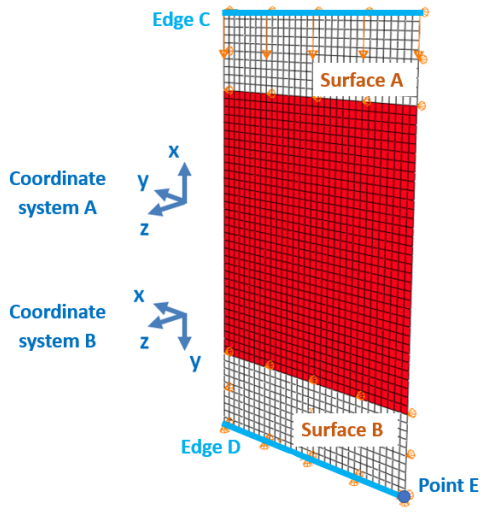

Figure 3.8: Numerical models and boundary conditions of test 1 and test 2.

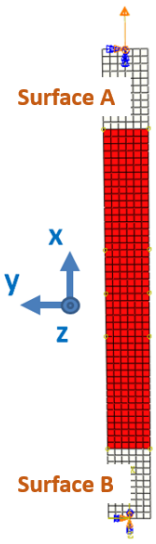

Figure 3.9: Numerical model and boundary conditions of test 3.

GEOMETRY AND ELEMENTS

The numerical model for test 3, which corresponds to the IPS experiment, has the dimensions of the test coupon described in Figure 3.6. It is defined with a layer of conventional shell elements for the same reasons as in section 3.2.1.

The final load-strain curves are obtained by looking both at the total reaction force at the displaced ends control point and the vertical displacement of this point. Strain is obtained by dividing the displacement by the total initial length of the specimen.

BOUNDARY CONDITIONS

For this experiment, the real boundary conditions consist in two ends firmly gripped by tabs. During the pull test, one end is fixed while the other undergoes a uniform displacement in the x direction. The resulting equivalent boundary conditions are shown in Figure 3.9 and are listed in Table 3.1.

MESH DEPENDENCY

A mesh sensitivity study is performed for this model, using elements size of 0.5 mm, 2 mm and 4 mm, and no difference is observed in the load-strain curves. Finally, the mesh chosen for this model has elements of 4 mm and is shown in Figure 3.9. Once the models built for the three tests used in level 1, the calibration process can start. It is described in the next section.

3.3. HASHIN DAMAGE MODEL CALIBRATION

This section describes the intra-ply damage model calibration approach and the final inputs. First, the elastic material parameters are optimized in order to calibrate the linear response of the material. This phase is described in subsection 3.3.1. The damage-related material parameters are subsequently optimized in order to calibrate the damage response in subsection 3.3.2.

3.3.1. LINEAR RESPONSE OPTIMIZATION

The first step to calibrate the Hashin damage model consists of optimizing the linear response of the three models described in section 3.2. Therefore for this activity, the damage initiation and propagation modules are disabled in Abaqus. A description of the way intra-ply damage is implemented in the software is given in 2.2.1. Since one ply of material is orthotropic and that plane stress shell elements are used in the model, the required inputs determining the elastic material response are E_{11}, E_{22}, ν_{12}, G_{12}, G_{13} and G_{23}. No specific material information is given on the out-of plane shear moduli. Since the level 1 tests do not involve any out-of-plane loading, it is decided to set $G_{12} = G_{13} = G_{23} = G$ for simplicity. Moreover, ν_{12} is removed from the

list of optimization parameters since its value usually varies very little around the default one. Additionally, having four parameters to optimize for only three tests would make the problem indeterminate. In the end, E_{11}, E_{22}, and G are the three elastic parameters that have to be optimized. As the response curves are linear, the calibration consists in matching the experimental elastic stiffness.

INITIAL RESULTS

The initial elastic responses before calibration are represented in Figures 3.10, 3.11 and 3.12, with the legend "default values". The clear mismatches between simulations and test results motivate the calibration step. The different elastic inputs have to be optimized in order to fit the test results.

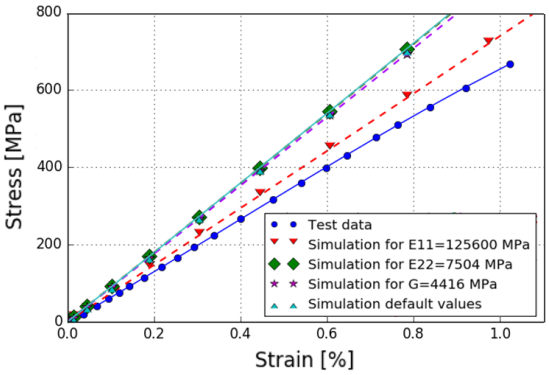

Figure 3.10: Original linear response of the test 1 model and responses for a reduction of 20 % in the independent elastic parameters.

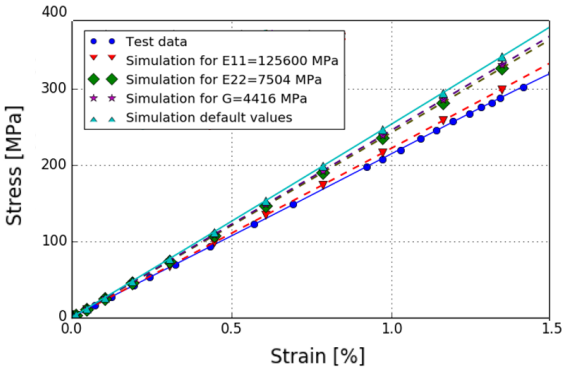

Figure 3.11: Original linear response of the test 2 model and responses for a reduction of 20 % in the independent elastic parameters.

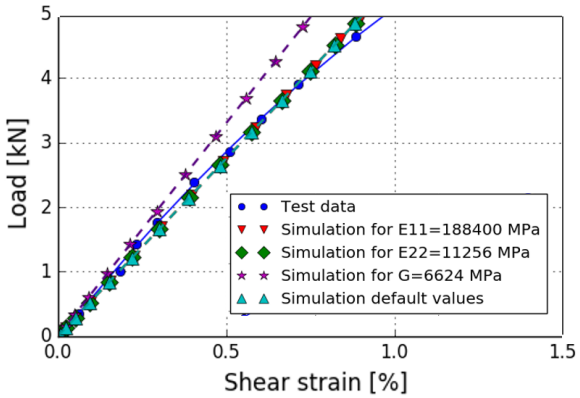

Figure 3.12: Original linear response of the test 3 model and responses for an increase of 20 % in the independent elastic parameters.

SENSITIVITY ANALYSIS

A sensitivity analysis to the three input parameters is performed on the three models. This analysis consists in observing the change in material response when making the parameters vary by a percentage around the initial value. The initial material inputs are given in Table A.1. The simulated responses for a variation of -20% of the three material parameters are given in Figures 3.10, 3.11 and 3.12. It can be observed that for each test, the material response is very sensitive, slightly sensitive or not sensitive to one parameter variation. The sensitivities of the models 1, 2 and 3 are summarized in Table 3.2.

ELASTIC PARAMETERS CALIBRATION

The calibration consists in obtaining a response curve for which the stiffness is similar to the experimental curve. Results of experimental tests have a certain scatter which should be taken into account in the optimization criterion. However, since no uncertainty evaluation is available for the current experimental data,

Parameter \ Model	Test 1 model	Test 2 model	Test 3 model
E_{11}	+	+	0
E_{22}	0	-	0
G	-	-	+

Table 3.2: Sensitivity of the level 1 models to the elastic parameters. +: variation of stiffness above 10% , -: variation of stiffness between 1 and 10%, 0: variation of stiffness below 1%.

the calibration is simply performed visually and a more precise criterion is not necessary.

From Table 3.2 is deduced an efficient way to optimize each parameter in order to have the models linear responses matching the experimental data. First, test 3 model is only sensitive to the variations of G, therefore G is optimized to calibrate test 3 model's linear response. Afterward, test 1 simulations can only be calibrated using E_{11}, therefore leaving test 2 simulations to be calibrated using E_{22}. This procedure is followed by modifying the parameters by hand and running the simulations using a python script. The final calibrated linear parameters are gathered in set 1:

$$E_{11,calib} = 0.71 \cdot E_{11}^0 = 111470 \text{ MPa} \tag{3.1a}$$

$$E_{22,calib} = 1.07 \cdot E_{22}^0 = 10037 \text{ MPa} \tag{3.1b}$$

$$G_{calib} = 1.10 \cdot G^0 = 6072 \text{ MPa} \tag{3.1c}$$

These results are satisfactory in the sense that usually, the coefficients of variation in material data are around 5 to 20% [18]. The values of set 1 therefore do not deviate excessively from the manufacturer's data. The calibrated linear responses can be seen at the initiation of the failure curves in Figures 3.13, 3.14 and 3.15.

3.3.2. DAMAGE INITIATION AND PROPAGATION OPTIMIZATION

The second step in the calibration process has for purpose to optimize the damage initiation and propagation behaviors of the three level 1 models. The Hashin theory together with the damage initiation and propagation modules of Abaqus are explained in subsection 2.2.1. The initiation of damage depends on the six strength parameters X_t, X_c, Y_t, Y_c, S_L, S_T, while propagation depends on the four fracture toughnesses GT1, GC1, GT2 and GC2. The useful damage outputs given by Abaqus are listed in Table B.1.

INITIAL RESULTS

The response curves for the level 1 models obtained when turning on the damage behavior are plotted from Figure 3.13 to Figure 3.15. The parameters used are the default ones, listed in Table A.1, except for the elastic parameters which have been calibrated and take the values of expressions (3.1). All damages are uniform per type of ply.

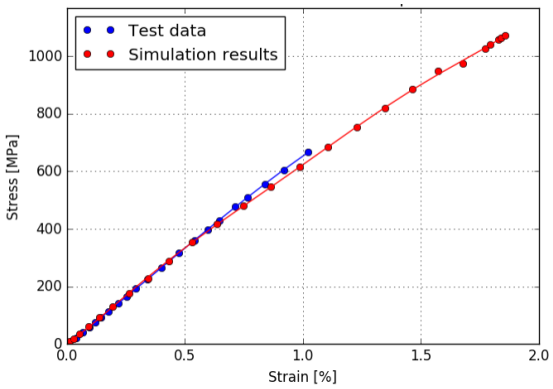

Figure 3.13: Full failure analysis response of the test 1 model, using the optimized elastic parameters from expression (3.1).

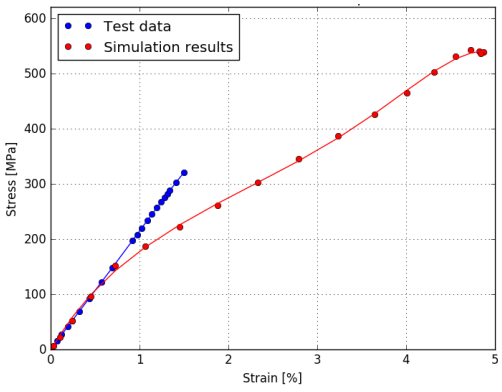

Figure 3.14: Full failure analysis response of the test 2 model, using the optimized elastic parameters from expression (3.1).

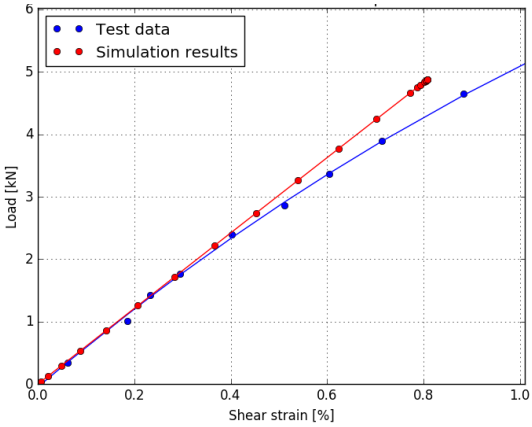

Figure 3.15: Full failure analysis response of the test 3 model, using the optimized elastic parameters from expression (3.1).

SENSITIVITY ANALYSIS

In order to efficiently optimize all the damage input parameters for the considered material, the sensitivity to these parameters is investigated for each of the three models. In addition, knowing precisely which parameters influence the results will allow to review the level 1 calibration, if it turns out to be necessary. This could happen if the validation results of the subsequent validation levels are not satisfactory.

First, the sensitivity to the strength parameters is investigated. These parameters modify the displacement at which damage starts in the fibers or in the matrix. After damage initiation, the behavior is not linear anymore and some elements progressively degrade until final failure. The strengths parameters sensitivity is presented in detail in appendix C. It is summarized in Table 3.3.

Model / Parameter	Test 1 model		Test 2 model		Test 3 model
	MC	FC	MC	FC	MT
Y_c, S_T	-	-	Yes	-	-
S_L	Yes	-	Yes	-	Yes
Y_t	-	-	-	-	-
X_c	-	Yes	-	Yes	-
X_t	-	-	-	-	-

Table 3.3: Strength parameters influence on the damage initiation of the level 1 models, depending on the damage mode. Yes: significant influence.

Some comments are made concerning the damages involved in all three simulation. For the model of test 1, the damage modes occurring during the analysis are MC in the 45° plies as well as FC in the 0° plies. MC damage occurs first and total failure is reached as soon as the FC damage starts, meaning that the material with damaged fibers looses very fast all of its load-carrying capacity. For the model of test 2, the damage modes occurring during the analysis are MC in the 0° plies and in the 45° plies, as well as FC in the 45° plies. Similarly to the test 1 model, MC damage occurs first, and total failure is reached as soon as the FC damage starts. For the test 3 model, the damage initiation and evolution is the same in all the plies. The only significant damage mode is the MT one. Total failure occurs as soon as MT damage initiates, which means that there is an instantaneous loss of load-bearing capability. Therefore, the simulation yields only linear curves, while the experimental load-strain curve is not linear. This is due to the fact that in reality, plasticity occurs in the material during this test and that this phenomena is not taken into account in the material model used here. Since the non-linearity starts in the material when matrix damage starts, the calibration is done by fitting the maximum simulated strength with the experimental onset of non-linearity [19].

The sensitivity results of Table 3.3 lead to two remarks. First, the parameters Y_t and X_t have no influence on any of the simulations. This was expected, as test 1 and 2 are compressive tests, while test 3 only involves material shearing. Tensile behavior validation is out of the scope of this master thesis. The second remark is

that the final failure load of each model depends on one specific strength parameter. This gives the possibility to precisely steer the final failure in the simulations.

Next, the influence of the fracture toughness parameters on the results is investigated. It is expected that GT1 and GT2 do not influence any of the simulations result. This is because test 1 and test 2 do not fail in tension and test 3 simulation has a linear behavior followed by a sudden catastrophic failure, which makes the influence of any fracture toughness null. This supposition is confirmed by a set of simulations in which the values of GC1, GC2, GT1 and GT2 are increased for the three models. For the test 1 model, a modification of 20% in GC1 or GC2 does not have any visible influence on the response curve. For the test 2 model, a modification of 20% in GC1 does not have a significant influence. A modification of 20% in GC2 increases the stiffness during damage by less than 5% and reduces the final strain by 4%. These influences are small compared to the increase in fracture toughnesses. Moreover, an increase in fracture toughness does not seem to lead to a predictable variation in the shape of the stress-strain curve. These aspects make the calibration of GC1 and GC2 difficult. Since the available test data itself is subject to scatter, it is decided not to calibrate the fracture toughness parameters during the current phase of the BBV approach.

PARAMETERS CALIBRATION

As represented in Table 3.3, some strength parameters influence several responses at the same time and there is no straightforward calibration strategy which comes out. The approach presented in this section starts with fitting the test 1 model response, followed by fitting the responses of tests 2 and 3. The calibration procedure consists in obtaining a response curve for which the damaged stiffness and final strength are similar to the experimental curve. As explained in section 2.4, even without good uncertainty evaluation, the indicative allowable error in strength is based on the data scatter provided by NLR. This allowable error is 10% for tests 1 and 2. For the test 3 model, no data scatter is available and determining accurately the experimental onset of non-linearity (which is used for calibration) is not possible in this study. Therefore, the error in the model's maximum stress is expected to be higher.

First, the test 1 curve fit is performed, starting with Figure 3.13. According to Table 3.3, two damage input parameters influence the simulations response; S_L and X_c. As explained, S_L influences the onset of non-linearity of the response curve. X_c directly influences the final failure strain, since the latter occurs as soon as fiber damage is initiated. The experimental curve appears to be quasi-linear up until fracture. The damage onset is very difficult to detect and it is therefore easier to start by optimizing the final failure, which means modifying the value of X_c. A good result is obtained by taking a calibrated value of $X_{c,calib} = 0.54 \cdot X_c^0 = 1133$ MPa. After analyzing the curve of Figure 3.2, it seems that nonlinearity starts around strain 0.7%. This means that S_L should be optimized such that damage in the matrix starts for the same strain value. This is achieved by taking $S_{L,calib} = 1.20 \cdot S_L^0 = 67$ MPa. The final simulated response is given in Figure 3.16, in red. All the final errors in strength obtained after calibration are gathered in Table 3.4.

The second step consists in optimizing the test 2 model response. Damage initiation in the matrices of the two types of plies depends on the values of S_L and S_T, while final failure depends on X_c. S_L and X_c were optimized with the previous model and are not modifiable without impacting the calibration of test 1. The simulation results for test 2 are shown in Figure 3.17.

The simulated and experimental curves are close in final strength but differ significantly in final strain. It is remarkable that during damage progression, the stiffness degradation is more significant for the simulation using the Hashin model than for the experimental curve. The amount of slope reduction once damage is initiated cannot be controlled, as it is built in Abaqus [10]. One way to improve the results in strain would be to lower X_c, which is not possible here. Otherwise, increasing the value of S_L and S_T could be beneficial to increase the portion of linear behavior, which would fit the experimental curve better. S_L is a parameter influencing all the tests, it is therefore preferable not to modify it at this stage. An indicative simulation is run increasing S_T by 70%, leading to a very small improvement in the strength value. Moreover, increasing only S_T by a large amount compared to the other strength parameters could be nonphysical, therefore S_T is not modified.

To conclude the calibration strategy, using the values of S_L and X_c previously optimized, the result of test 3 is given in Figure 3.18. This result depends only on S_L. The objective with this test is to have the final strain of the simulation occurring at the same time as the non-linearity onset in the experiment. For the models of

tests 1, 2 and 3, the strength errors are all reasonable given the present context.

Therefore, the final set of strength parameters is called set 2 and corresponds to

$$X_{c,calib} = 0.54 \cdot X_c^0 = 1133 \text{ MPa} \tag{3.2a}$$
$$S_{L,calib} = 1.20 \cdot S_L^0 = 67 \text{ MPa} \tag{3.2b}$$
$$S_{T,calib} = S_T^0 = 46 \text{ MPa} \tag{3.2c}$$
$$Y_{c,calib} = 2 \cdot S_{T,calib} = 91 \text{ MPa} \tag{3.2d}$$

A second calibration approach was attempted, which is presented in appendix D. It starts with fitting test 2 followed by tests 1 and 3. The associated errors are not satisfactory, as summarized in Table 3.4. Moreover, the final set of inputs obtained with that method is less close to the initial data set than expression (3.2). In conclusion, the set 2 of strength parameters appears to be the best compromise for the level 1 calibration.

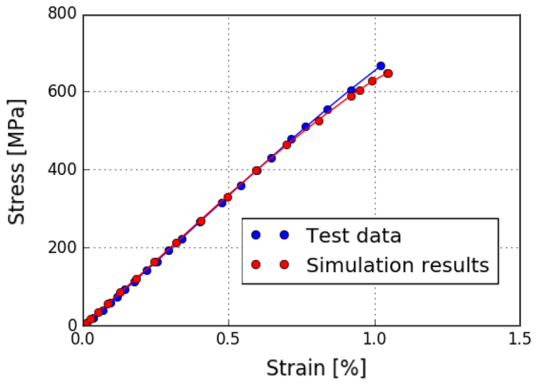

Figure 3.16: Response of the test 1 model with the calibrated elastic parameters and, in the first calibration approach, $X_{c,calib} = 1133$ MPa, $S_{L,calib} = 67$ MPa.

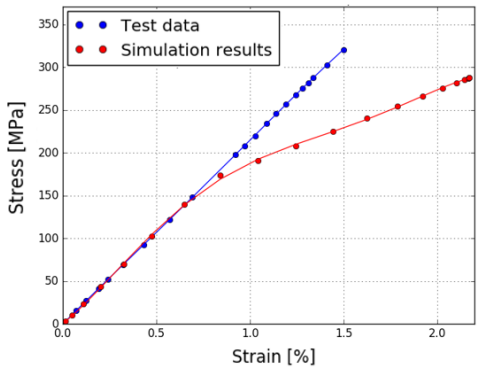

Figure 3.17: Response of the test 2 model with the calibrated elastic parameters and, in the first calibration approach, $X_{c,calib} = 1133$ MPa, $S_{L,calib} = 67$ MPa.

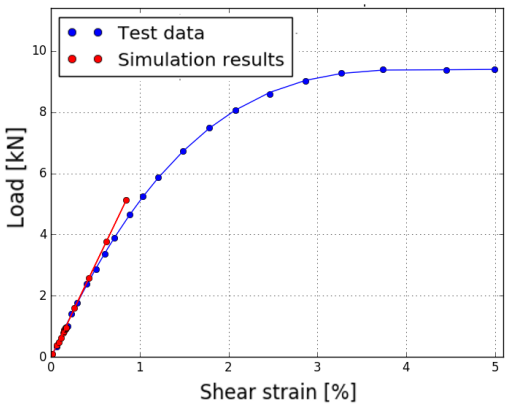

Figure 3.18: Response of the test 3 model with the calibrated elastic parameters and, in the first calibration approach, $X_{c,calib} = 1133$ MPa, $S_{L,calib} = 67$ MPa.

Calibration approach	Model	Final strength error
Non-optimized strength inputs	Test 1	+60%
	Test 2	+70%
	Test 3	+24%
Main approach subsection 3.3.2	Test 1	-3%
	Test 2	-10%
	Test 3	+25%
Alternative approach appendix D	Test 1	-28%
	Test 2	-9%
	Test 3	+110%

Table 3.4: Errors in predicted strengths for tests 1, 2 and 3 obtained with two calibration approaches

3.4. CONCLUSION

This chapter described the calibration of the Hashin damage model. It required to optimize the material's elastic, strength and fracture toughness input data. For that purpose, the experimental response curves of two mixed layups compression tests and an IPS test were confronted to the three corresponding simulations. The influence of the elastic parameters on the numerical responses was clearly segregated from the influence of the strength parameters. This allowed a calibration process in two phases. The first phase focused on the sensitivity to the elastic parameters and a subsequent inputs optimization was performed. The second phase focused on the sensitivity to the strength parameters followed by the best calibration strategy. Knowing the models dependencies over the various inputs additionally facilitates a potential re-calibration. The calibrated stiffness parameters of expression (3.1) yielded negligible errors in test 1 to 3 elastic responses. The strength input calibration yielded expression (3.2) with acceptable errors in final strengths for test 1, 2 and 3, which means that the calibration was successfully performed. Since the three available tests have a very brittle behavior, no influence of the fracture toughness inputs was observed and their optimization was therefore impossible.

It was remarkable that the stiffness predicted for test 2 was low after matrix damage initiation. This parameter is not modifiable since it is inherent to the damage theory. It was as well pointed out that in addition to the absence of reliable information concerning data scatter, the occurrence of intra-ply and inter-ply damage in the test specimens is not precisely known. It is therefore possible that some delamination occurs before final failure, which would make the simulations strengths slightly under-predicted in the case of test 1 and 2.

The description of the calibration process made in this chapter makes it clear that the quality and quantity of available experimental data is primordial to perform a good optimization. The next section discusses the experimental result modifications which would have been required to improve the level 1 procedure of the BBV approach.

3.5. RECOMMENDATIONS FOR LEVEL ONE

Following the conclusion of this chapter, specific recommendations are given on the test data which would make the intra-ply damage model calibration more straightforward.

3.5.1. EVALUATION OF UNCERTAINTY

A major improvement would be achieved in evaluating the calibration results if uncertainties were evaluated both in the models and in the experiments. This aspect is out of the scope of this study and should be central in the future work. It was pointed out that evaluating errors cannot be meaningful without knowing at least the data scatter. This advice is applicable to the totality of the tests used throughout this report. The following recommendations are based on the Guide for Verification and Validation in Computational Solid Mechanics [2].

First, uncertainty must be estimated in the model. The aleatory uncertainty, corresponding to the uncer-

tainty intrinsically linked to the system, includes for example the variation in geometry, material properties, loading environment and assembly procedures. The variability can be propagated throughout the simulation using probabilistic analysis, using for example Monte-Carlo simulation [20]. This yields a quantified distribution in the simulation output quantities. Estimating simulations reliability is another possibility [21].

A scatter is as well present in the validation of the test results. Performing redundant measurements on different specimens enables the evaluation of that scatter, and is common practice. The scatter can come from the variability in the specimen's manufacturing defects, material properties, boundary conditions, gauges calibration and installation, and data acquisition. It is recommended to formulate uncertainties with the data mean value and standard deviation or distribution. Estimating both model and test uncertainties before validation is essential to draw appropriate conclusions about the model's predictive accuracy.

3.5.2. RECOMMENDED SET OF TESTS

The input strengths calibration could be achieved by fitting independent tests strengths. Difficulties arise when two tests are mainly influenced by the same inputs. A recommendation to calibrate all the strength parameters would therefore be to use simple, unidirectional material coupon tests having a single failure mode each: 0° tension (for X_t), 0° compression (for X_c), 90° tension (for Y_t) and 90° compression (for Y_c). The two latter are given if it is desired to extend the work scope to tensile behavior calibration. The advantage is that a single type of coupon would be required for the four types of tests. Additionally, the current IPS test enables to calibrate S_L in a satisfactory way. Using these five tests would as well allow to easily calibrate the elastic parameters, since the matrix- and fiber-dominated response would be segregated.

Calibrating the fracture toughness parameters is not possible if the coupon tests have a brittle behavior. These four parameters influence the energy dissipation after damage initiation. A possibility to explore could be to calibrate them by using the response curves of cycling tests. As described in the Abaqus manual [10], the damaged stiffness matrix of an element depends on the damage parameters D_i, which themselves evolve such as the equivalent stress in the damaging material follows a TSL law. The area under this TSL is defined by the fracture toughness inputs. Therefore, estimating the stiffness reduction during a cycling test could enable to back-calculate the corresponding inputs of material fracture energy.

3.5.3. TEST SET-UP

An additional remark is made concerning the experimental outputs. This recommendation is valid for any test conducted in a BBV approach. The quantities have to be measured on the specimens themselves, in order to avoid mixing the test bench own deformation or slippage with the sample deformation. For example, test 1 and 2 displacement outputs have to be extrapolated at their origin in order to get rid of the spurious initial softening behavior which adds to the uncertainty. Using extensometers or strain gauges on the sample outer plies constitutes a simple improvement. In addition, knowing if and when delamination occurs during a composite compression test is primordial to calibrate an intra-ply damage model. Therefore, it is recommended to record a video of the test to determine the sequence of events and adapt the calibration procedure.

The next chapter is dedicated to level 2 of the BBV pyramid, where the validation of the intra-ply damage model is described.

4

Level Two: Validation of the Damage Model

This chapter describes the process of validation corresponding to level 2 of the BBV approach presented in section 2.3. The purpose of this level is to assess the accuracy of the results obtained with the calibrated Hashin damage model of chapter 3, modeling an Open-Hole Compression (OHC) test. Section 4.1 presents the OHC experimental test set-up and results. The corresponding numerical model is described in section 4.2. The numerical results are analyzed in section 4.3. Finally, a conclusion is given in section 4.4 along with recommendations which can be found in section 4.5.

4.1. Data for Test Four: Open-Hole Compression Test

The test used for the damage and fracture validation procedures is a 0° OHC test, called test 4. It has the ETF layup $[0/+45/0/-45]_{4S}$. Dimensions of the test sample are given in Figure 4.1. The test is conducted using the ASTM D6484 standard [22], with a NASA short block compression test fixture which is similar to the one used for test 1 and 2 [16]. The test is performed in an 300 kN Instron test machine, under displacement rate control. Force and displacement are measured in the same way as in test 1 in subsection 3.1.1, which yields the linearly extrapolated load-displacement curve in Figure 4.3. As shown in Figure 4.2, the failure modes observed on the final specimen are a combination of intra- and intra-ply damages. The moment at which inter-ply damage initiates during the test is not known. The next section describes the corresponding OHC test model.

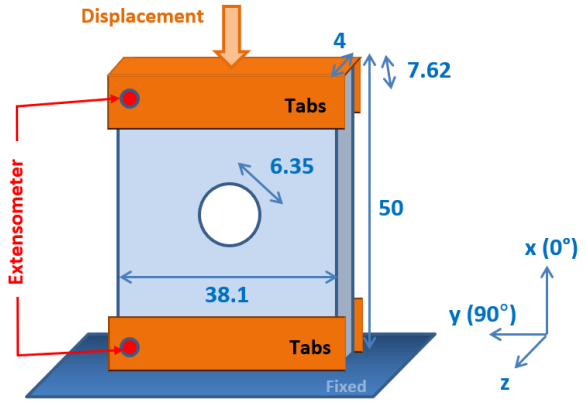

Figure 4.1: Experimental set-up of the OHC test, lengths are in mm.

Figure 4.2: OHC specimen after testing

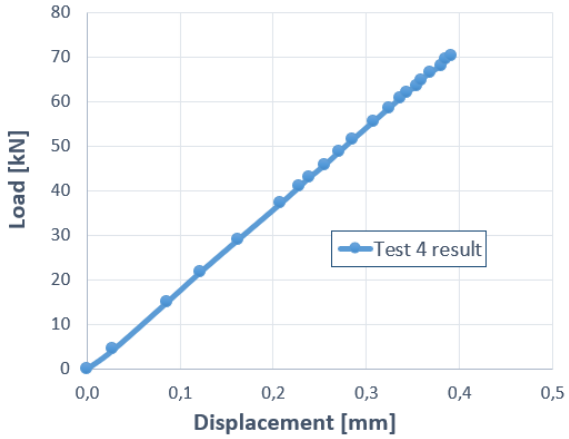

Figure 4.3: Load-displacement curve of the OHC test, extrapolated at the origin.

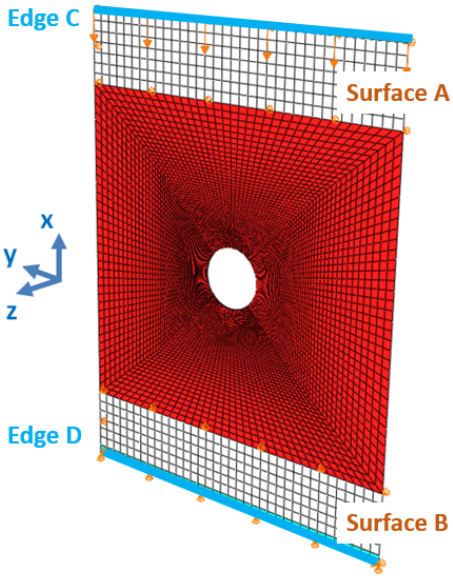

Figure 4.4: Numerical model and boundary conditions of the OHC test for level 2 validation.

4.2. NUMERICAL MODEL FOR LEVEL TWO OHC TEST

In order to perform the validation approach of the Hashin damage model, the OHC numerical model is developed. It takes as inputs the optimized values of expressions (3.1) and (3.2).

4.2.1. GEOMETRY, BOUNDARY CONDITIONS, ELEMENTS

The OHC model, including only intra-ply damage modelization, is very similar to the one made for test 1 in section 3.2.1. Apart from the plate dimensions and the presence of a hole, the experimental set-up is the same. In particular, the boundary conditions are modeled the same way and are given in Table 3.1. Since the current simulation has for purpose to validate the damage model, the same elements are used. Therefore, one layer of conventional shell elements still represents all the plies through the thickness. Three integration points are defined through the thickness of each composite layer.

The final reaction force is obtained with the total vertical reaction force on edge C in Figure 4.4. The final displacement is obtained from the vertical displacement of one of the edge C nodes.

4.2.2. MESH DEPENDENCY

It is observed that the final stiffness and strength of the specimen strongly depend on the mesh size. The explanation for this phenomenon is given in this section together with a mesh convergence study.

ORIGIN OF THE DEPENDENCY

In the current case, the finer is the mesh, the stiffer the response. This is due to the fact that a coarse mesh cannot capture accurately the stress concentrations present around the hole. Moreover, as discussed by Chen at al. [23], when a single depth of shell elements is used, the predicted strength of the material also depends on the mesh refinement. The finer is the mesh, the stronger the specimen. The strength prediction overall higher than the experimental data. This stems from the assumption of a perfect bond between the plies. Without inter-ply failure, the deformation of the damaged elements are constrained by the neighboring plies, therefore transferring the load to the adjacent elements and causing an over-prediction of the laminate's bearing capacities. Refining the mesh leads to further constraining the deformation of the failed elements, resulting in a smaller volume of damaged region and a larger strength.

It is nonetheless decided to ensure the mesh converges with respect to the resulting stiffness and not with the strength value. This decision stems from the fact that the OHC failure process has a great complexity and undergoes mixed-more failure, as it is explained in section 2.4. Since the simulations created in the current chapter do not take delamination into account, the comparison to test data can only give an idea of

the Hashin model performance. Level 4 includes inter-ply delamination and is more likely to yield results comparable to the test data. Another reason not to investigate the strength convergence are the time and the computational power required to perform full failure simulations with this model. The number of these simulations is therefore kept as low as possible.

MESH CONVERGENCE PARAMETER

The approach for mesh dependency is therefore to make sure that the stress concentrations around the hole in the linear regime are sufficiently well captured. This permits to correctly predict the linear stiffness and damage initiation. The convergence study is done with respect to the strain concentration factor $K = \epsilon_{max}/\epsilon_{nominal}$. The maximum strain in the 0° direction corresponds to ϵ_{max}, while $\epsilon_{nominal}$ is the global strain in the 0° direction, calculated from the displacement at the loaded edge divided by the initial specimen length. This concentration factor is defined only during the linear response. It is preferable over the stress concentration factor in this precise case because strain is identical through the plies, whereas stress is not. The strategy to obtain an acceptable value of K without using too much computational power starts by looking at the convergence of K with mesh refinement. Subsequently, a custom mesh is created which possesses a K value judged close enough to the converged value.

MESH CONVERGENCE STUDY

Using a number of different homogeneous meshes, ranging from a size of 1.6 mm to 0.14 mm, the value of K is extracted and plotted versus the inverse of the mesh size in Figure 4.5. Considering the inverse of the mesh size permits to visualize the convergence behavior. The available computational power does not allow

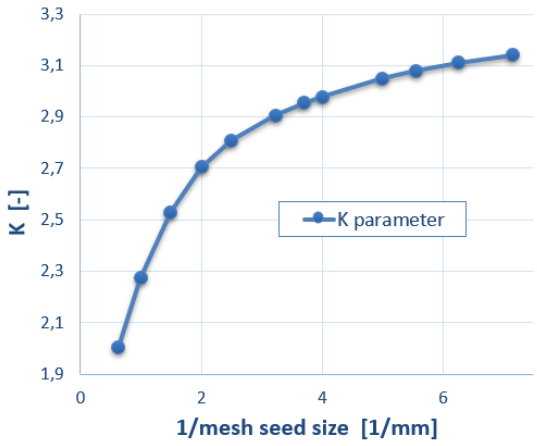

Figure 4.5: Strain concentration factor K of the OHC model versus the inverse of mesh seed size.

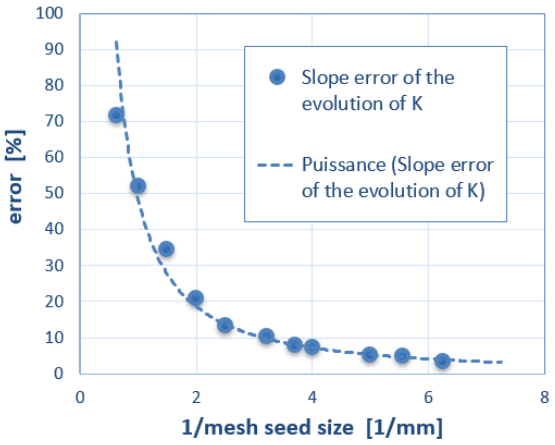

Figure 4.6: Error in slope for the evolution of K in the OHC model, versus the inverse of mesh seed size.

to have results for mesh seeds smaller than 0.14 mm for the whole specimen, and no theoretical evolution of K is known for this test. The degree of convergence for each data point has therefore to be estimated. For that purpose, the slope of K is calculated at each data point in Figure 4.5, using the previous and current data point coordinates. This gives an overestimation of the slope and ensures conservativeness. This slope, noted S, should tend towards 0 during convergence. The relative error in slope is estimated with the formula $err = \frac{S_{simu} - S_{conv}}{S_{conv}+1} \cdot 100 = S_{simu} \cdot 100$. The evolution of error with mesh refinement is presented in Figure 4.6. The maximum error in slope which is judged acceptable with respect to the available computational power is 5%. This corresponds to a value of K above 3.1.

A new custom mesh is designed to give a value of K above 3.1, while using a limited number elements. Since the stress concentrations occur at the hole edge and that having a converged K value means capturing accurately the stress concentration, the mesh has to be fine around the hole. On the contrary, the mesh can be coarsened far from the hole. It is preferable to keep square-like elements for the accuracy of the finite-elements calculation. The hole edge is seeded with elements of size 0.14 mm, and the fixture areas with elements of 1.1 mm. The mesh is represented in Figure 4.4. Running a simulation with this mesh, $K = 3.21$ is obtained, therefore satisfying the convergence criterion, while the computational time required is reduced

from two hours to one minute. The custom mesh is kept for the validation procedure, which is performed in the next section.

4.3. HASHIN DAMAGE MODEL VALIDATION

This section describes the numerical results obtained with the intra-ply damage model. The simulations conducted in this level have for purpose to evaluate the performance of the linear material response and the Hashin damage model on a new, more complex loading case. Damage initiation and propagation modules are re-activated in Abaqus. First, the simulation results are presented with the default inputs in subsection 4.3.1. Subsection 4.3.2 presents the results obtained with set of calibrated values.

4.3.1. INITIAL RESULTS

The simulation results using the default parameters of Table A.1 yields the result of Figure 4.7. Both a mismatch in initial stiffness and final load are observed. The errors are given in Table 4.1. This response is used as a basis to observe the influence of the calibration.

Simulated response	Error in stiffness	Error in Strength
Default parameters	+41%	+74%
Result of set 1 & set 2	+7%	+7%

Table 4.1: Errors in predicted stiffness and strength for the OHC model, using the default, set 1 and set 2 inputs.

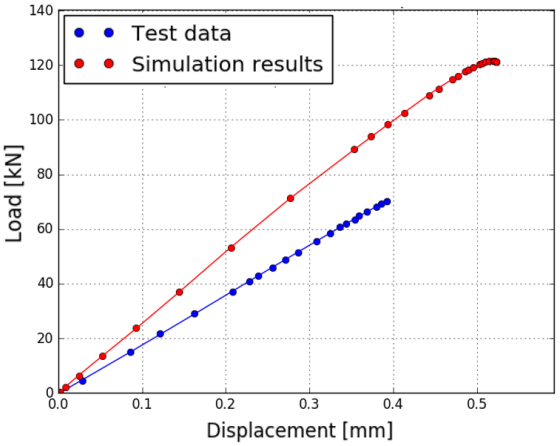

Figure 4.7: OHC model's response in level 2, using the default input parameters.

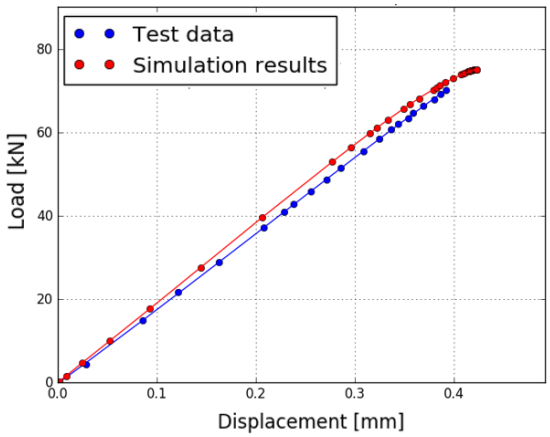

Figure 4.8: Response of the OHC model in level 2, using set 1 and 2 of parameters.

4.3.2. PERFORMANCE OF THE CALIBRATED PARAMETERS

The response obtained for the input sets 1 and 2 from expressions (3.1) and (3.2) is plotted in Figure 4.8 and the errors are summarized in Table 4.1. Compared to the initial result of subsection 4.3.2, the improvement in both strength and stiffness prediction is significant. The remaining strength error stays within the indicative limit of 10% which was fixed for the OHC strength in section 2.4. Since no scatter data is available for the stiffness of this OHC test, an indicative allowable error of 15% is taken from literature [24]. The simulated linear stiffness respects that criterion. The overestimation of strength is satisfactory in the sense that adding delamination to the models in level 4 is expected to lower this value.

In addition, appendix D shows the OHC result using the alternative set of inputs which was not selected during calibration. As expected, the results for this input set are not satisfactory.

To conclude this level, the final set of input parameters is composed of set 1 and set 2:

$$E_{11,calib} = 0.71 \cdot E_{11}^0 = 111470 \text{ MPa} \tag{4.1a}$$
$$E_{22,calib} = 1.07 \cdot E_{22}^0 = 10037 \text{ MPa} \tag{4.1b}$$
$$G_{calib} = 1.10 \cdot G^0 = 6072 \text{ MPa} \tag{4.1c}$$
$$X_{c,calib} = 0.54 \cdot X_c^0 = 1133 \text{ MPa} \tag{4.1d}$$
$$X_{t,calib} = X_t^0 = 2505 \text{ MPa} \tag{4.1e}$$
$$S_{L,calib} = 1.20 \cdot S_L^0 = 67 \text{ MPa} \tag{4.1f}$$
$$S_{T,calib} = 1.20 \cdot S_T^0 = 46 \text{ MPa} \tag{4.1g}$$
$$Y_{c,calib} = 2 \cdot S_{T,calib} = 91 \text{ MPa} \tag{4.1h}$$
$$Y_{t,calib} = Y_t^0 = 76 \text{ MPa} \tag{4.1i}$$
$$GT1, GC1, GT2, GC2: \quad \text{unmodified} \tag{4.1j}$$

4.4. CONCLUSION

This chapter described the validation approach of the material's linear behavior and the Hashin damage model. It consisted in estimating the errors in predicted stiffness and strength for an OHC test. The numerical model developed for this activity is strongly mesh-dependent, and mesh convergence was studied. The final mesh is a biaised mesh refined around the hole, which yields an error in strain concentration factor evolution below 5% and yields a satisfactory computational efficiency. The final simulation results obtained with the calibrated sets of inputs from expressions (3.1) and (3.2) satisfy the criteria which were defined for the stiffness and strength errors. The OHC damage simulation in this BBV step is therefore successful based on the current indicative allowables.

A significant amount of delamination is visible on the final experimental sample. The choice of using the OHC test for the current intra-ply damage validation is not optimal, but was unavoidable given the lack of available test data. It is expected that adding the delamination to the analysis in level 4 should yield a reduction in strength. Therefore, the strength results are over-predicted on purpose in the current chapter which only included an intra-ply damage model. In addition, in order to be able to easily revise the calibration of the Hashin strength parameters during level 4, a short input parameters sensitivity analysis is conducted in appendix E. The next section discusses possible improvement of the test data used for level 2 of the BBV approach.

4.5. RECOMMENDATIONS FOR LEVEL TWO

Following the conclusion of this chapter, uncertainty quantification presented in subsection 3.5.1 are recommended. In addition, one main recommendation is given with respect to the test data which would make the intra-ply damage model validation complete and straightforward.

4.5.1. RECOMMENDED SET OF TESTS

The available OHC test sample used to perform the level 2 validation activity shows clear delamination after failure. The presence of the stress concentrations around the hole most likely triggers inter-ply fracture before total failure. For that reason, using this test to validate the intra-ply damage model alone is not adapted. This issue constitutes the main limitation of the current validation step. As explained in appendix E, a few input parameters which were not strictly calibrated in chapter 3 still maintain a certain degree of freedom. A decision concerning these parameters can only be taken once the model includes delamination in level 4 of the BBV approach, which makes the whole BBV approach intricate.

It would therefore be more appropriate to have experimental coupon tests which show little or no delamination. Since unidirectional laminates were recommended to be used in the calibration process (see section 3.5), the validation can be performed with a few coupons having different ply orientations. In the scope of compression tests, test 1 and 2 would be, for example, two good candidates for the validation level. This is because their responses depend on all the strength input parameters involved in compression testing. Any other pair of compression tests having a simple mixed layup, one having a fiber-dominated behavior and one having a matrix-dominated behavior, can be considered.

The next chapter describes the level 3 of the BBV pyramid. It corresponds to the calibration of the inter-ply fracture model.

5

Level Three: Calibration of the Fracture Model

This chapter describes the calibration of the cohesive fracture model used to simulate delamination. It corresponds to the level 3 of the BBV approach presented in section 2.3. In section 5.1, the Inter-Laminar Shear (ILS) experimental test and results used for the calibration activity are presented in detail. The corresponding numerical model is described in section 5.2. The calibration is performed in section 5.3. Finally, a conclusion is drawn in section 5.4 and recommendations are provided in section 5.5.

5.1. Data for Test Five: Three-Point Bending Test

The test used for fracture calibration is called test 5. It is a three points bending test for the ETF' layup defined by $[0/0/+45/0/-45/0/+45/0/0]_S$. The test is conducted using the ASTM D2344 standard [25], in a 100 kN Instron test machine, under displacement rate control. Dimensions of the specimen and pins are shown in Figure 5.1. ETF' layup is used rather than ETF layup in an attempt to ensure that the specimen fails between the 0° plies at the center of the laminate. However, examination of the failed specimen reveals that delamination still occurs in between the 45° and 0° plies. There is no other visible failure mode other than inter-ply fracture, as represented in Figure 5.3.

Displacement is measured on the movable nose with an extensometer as sketched in Figure 5.1. Load is measured by the force-sensing device included in the test bench. This yields the curve shown in Figure 5.2, which is extrapolated at the origin to remove the initial spurious softening.

Unlike the other experimental tests used in this Master thesis, the three points bending load-displacement curve is used only to extract the final failure load value. It was found out during the calibration process that the experimental and simulated response curves could not be fitted with the linear parameters which were validated in chapter 4. After investigating the source of this mismatch by improving the numerical model and performing several sensitivity studies, it was concluded with NLR that the mismatch mostly stems from the ILS test set-up. First, the displacement was measured in the bench, meaning that the deformations of the test head and support rig themselves are included in the measure. Even if this part is very stiff, it is large and small strains can lead to significant measured displacements in the bench head. Additionally, there are local indentations in the loading head and support which are as well included in the final displacement. Measuring accurate displacements within the specimen is almost impossible for this test and is not common practice, therefore, since no estimation of the test rig deformation and local indentations are available, the measured displacement cannot be compared to simulations. The final load, however, can still be used.

5.2. Test Five Numerical Model

In order to perform the calibration of the delamination model, the three-point bending test numerical model is developed. This model only includes the fracture considerations and no damage behavior is defined. This is justified by the fact that the failure triggered by three-point bending happens mainly due to shear in-between the plies and not inside the layers. This assumption is confirmed by the result of test 5 provided by NLR. The

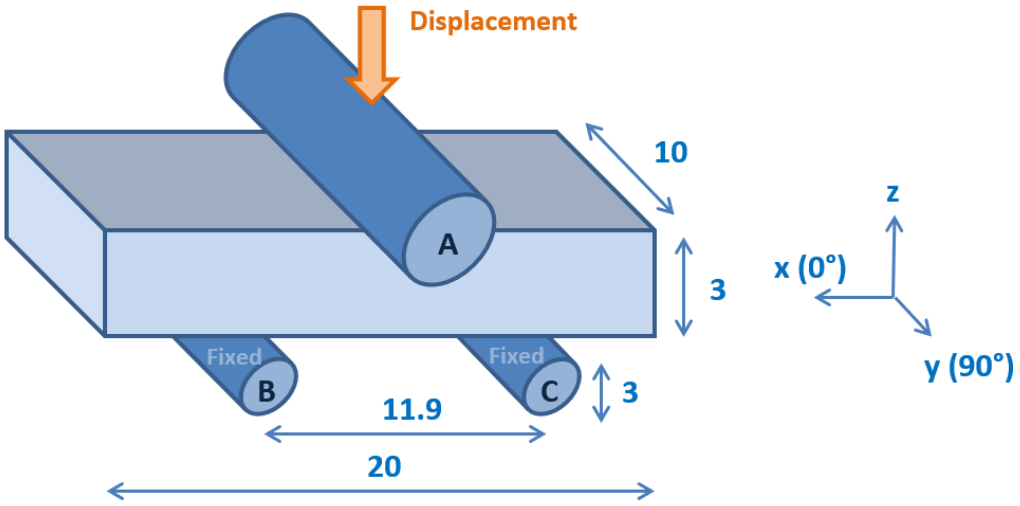

Figure 5.1: Experimental set-up of the ILS test.

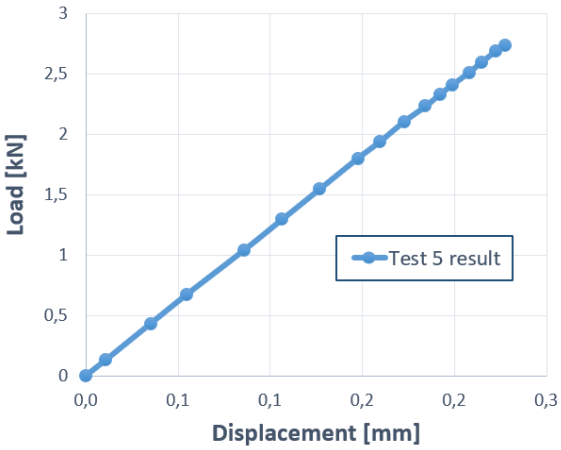

Figure 5.2: Load-displacement curve of the ILS test, extrapolated at the origin.

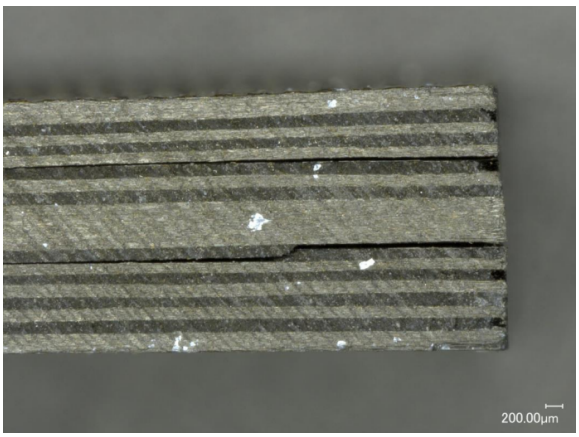

Figure 5.3: ILS specimen after testing.

fracture model to be calibrated consists in a cohesive contact model included in Abaqus which is used in the contact interaction definition between each ply of the composite. Cohesive contact is preferred to cohesive elements because there does not really exist an interface thickness between the plies. The layers, which are for example co-cured together, are simply bonded by their matrix over a thin region. The contact model is additionally simpler to implement and more computationally effective [10]. In the following subsections, the type of elements, the contact properties, the cohesive behavior, the boundary conditions and the mesh are described.

5.2.1. GEOMETRY, ELEMENTS AND DEFAULT INPUTS

The sample geometry corresponds to the one described in Figure 5.1, with each layer modelled separately. The layup is represented in section 5.1. The elements constituting the layers have to remain plane-stress elements, since the Hashin criterion imposes this condition and is to be included in level 4. The choice has therefore to be made between conventional shell elements and continuum shell elements. The continuum shells discretize an entire three-dimensional body, while conventional shells discretize a reference surface. Continuum shells include the effects of transverse shear deformation and thickness change, they can be stacked through thickness and they allow for the prediction of transverse stresses. For simplicity of modeling, continuum shells are therefore preferred over conventional shells. It makes the stacking of numerous

plies and definition of plies interaction more straightforward. In order to validate the choice of shell elements for the current loading case, which is a mix of bending and shear deformations, results for both solid and shell elements are compared in subsection 5.2.5, once the other models features are chosen.

The elastic material data used for the simulations are the validated values of expression (3.1). The cohesive surface model, which is explained in subsection 2.2.2, requires to input K_{nn}, K_{ss}, K_{tt}, X_{2t}, X_6, GT2 and G6. The bilinear TSL is defined by the maximum stress criterion, since the strength of the interface can be interpolated as being the strength of the matrix material. Therefore, it is assumed that $X_{2t}^0 = Y_t$ and $X_6^0 = S_L$. The initial values are listed in Table A.1. The formula to calculate K_{nn}, K_{ss} and K_{tt} depends on the material elastic behavior. A formula is proposed by Moslemi and Khoshravan [26]. The magnitude of the penalty stiffness has to be high enough to avoid interpenetration of the crack surfaces, but low enough to avoid numerical convergence issues. The assumption is made that the penalty stiffnesses for all modes of fracture are considered to be the same, meaning $K_{nn} = K_{ss} = K_{tt} = K$. The formula used to calculate the penalty stiffness is:

$$K = \alpha\left(\frac{E_3}{t}\right) \tag{5.1}$$

Where α is a parameter larger than one, E_3 is the Young's modulus of the interface in the transverse direction and t is the sub-laminate's thickness. Moslemi and Khoshravan advise to take $\alpha = 50$, therefore having E_3 is small enough compared to $K \times t$ in order to ensure that the effective elastic properties of the material will not be affected by the cohesive face. Since the interface between the plies is constituted by matrix material, E_3 corresponds to the calibrated matrix material's Young's modulus E_{22} from expression (4.1). The parameter t corresponds to the thickness of a ply, which yields in the present case $t = 0.167$ mm. Finally, $K_{nn} = 3 \cdot 10^6$ MPa.

5.2.2. CONTACT DEFINITION

Once the plies are modelled individually, the contact between each ply has to be defined. The definitions given in this section are provided by the Abaqus manual [10]. First, a contact discretization method is required. The surface-to-surface contact discretization method consists in enforcing contact conditions in an average sense on areas around the slave nodes. Therefore, each contact constraint will predominantly consider one slave node but will also consider adjacent slave nodes. In the node-to-surface formulation each slave node on one side of a contact interface interacts with a point of projection on the master surface on the opposite side of the contact interface. Surface-to-surface is recommended for situations in which normal directions of contacting surfaces are opposite. Both formulations are tried for the current model and no differences are observed. Since it is less computationally costly, the node-to-surface definition is chosen.

A tracking approach also has to be selected in order to account for the relative motion of two interacting surfaces. Two possibilities are offered by Abaqus/Standard: the finite-sliding approach and the small-sliding approach. Finite-sliding contact is the most general tracking approach and permits arbitrary relative separation, sliding, and rotation of the contacting surfaces. In small-sliding, the groups of nodes involved with individual contact constraints are fixed throughout the analysis, which means that one should be sure that the sliding between the two surfaces remains very limited. During a three-point-bending test, the layers tend to slide with respect to each other, this is why delamination is the main failure mode. Therefore, it is safer to choose the finite-sliding approach.

5.2.3. BOUNDARY CONDITIONS

Several types of boundary conditions were investigated. The need for an investigation stems from the fact that the interaction between the loading pin and the laminate itself corresponds to a surface which is not exactly a line and the influence of the exact modelization of the pin is unknown. The representation of the set-up can be seen in Figure 5.1. Three different possible sets of boundary conditions are proposed in Appendix F: the solid cylinders conditions, the analytical rigid conditions, and the equivalent conditions. The comparison is a complex matter due to the fact that several parameters influence the results; when running a simulation, the result depends on boundary conditions, but also on the mesh size and the elements' definition.

In order to choose a set of boundary conditions, simulations are run for an uniform mesh of 0.8 mm, with a laminate composed of SC8R elements. The shell structure shows a high amount of hourglassing around

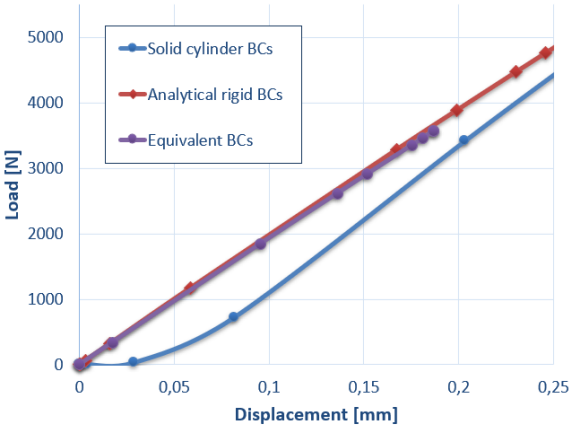

Figure 5.4: Load-displacement curves of the ILS model for the three types of boundary conditions, using a mesh seed of 0.8 mm on each ply. BCs: Boundary Conditions.

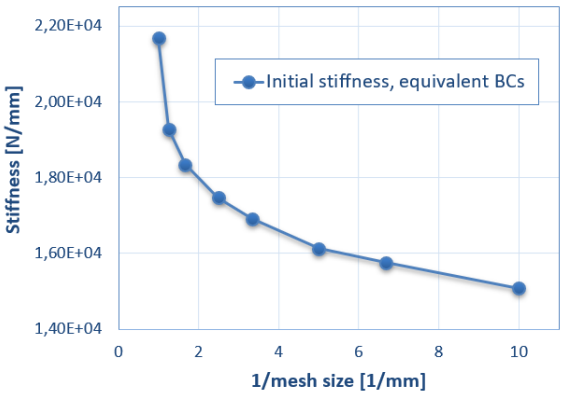

Figure 5.5: Stiffness of the ILS model versus the inverse of mesh refinement using equivalent boundary conditions. BCs: Boundary Conditions.

the displacement zone for all types of boundary conditions. Therefore, the enhanced hourglassing control is applied to the laminates elements for all the simulations. It is later justified that this choice does not modify significantly the stiffness results. The material responses are plotted using the three types of boundary conditions detailed in Appendix F. The results are presented in Figure 5.4.

The solid cylinders boundary conditions yield a converging simulation. On the other hand, the analytical rigid cylinders' boundary conditions yield simulations which cannot converge for a displacement above 0.26 mm. The analysis with the equivalent boundary conditions stops before 0.18 mm. In an attempt to see if the coarse mesh is the source of this convergence difficulty, additional simulations are run for the last two types of boundary conditions with a small mesh seed of 0.3 mm. All the simulations abort for a very low value of applied displacement, therefore these boundary conditions are not adopted to model this test. In addition, for the model using equivalent boundary conditions, Figure 5.5 shows that the stiffness does not converge with mesh refinement in the limit of the available computational power. These remarks lead to the choice of the boundary conditions with cylinders made of solid elements.

Figure 5.4 shows that the solid cylinders' boundary conditions present a nonlinear behavior at the start of the analysis. This is justified by the use of a contact, which takes some initial displacement to be properly established. This effect is enhanced by the large mesh size as it is shown in subsection 5.2.4. It is not considered an issue as long as the nonlinear part of the curve is ignored.

5.2.4. MESH DEPENDENCY

The mesh convergence has to be proven on the laminate, using the selected boundary conditions. The convergence metrics is defined in percentage difference of linear stiffness, in the same way as in chapter 4.

A series of simulations are submitted with a decreasing mesh size. The memory access permits to go down to an uniform mesh seed size of 0.3 mm. Since the critical areas in terms of mesh are the contact zones with the cylinders, a way to go down in mesh size is to refine the mesh in all the plies below and above the cylinders' contact zones, and keep a seed size of 0.3 mm elsewhere. The different structural responses are shown as a function of mesh size in Figure 5.6. For coarse meshes, the response does not show linear behavior before 0.06 mm displacement, therefore no elastic stiffness is defined in these cases. The evolution of elastic stiffness versus the inverse of mesh size is shown in Figure 5.7. A stiffness convergence is observed. It is decided that the convergence criterion is to have an error in stiffness below 3% with respect to the biased mesh 0.3-0.05 mm stiffness, which is a converged mesh. So far, the coarser satisfactory mesh is therefore the biased mesh 0.3-0.2 mm. The structure's stiffness is 16950 N/mm ± 3%. The maximum error of 3% is very low compared to usual practice [24], but is affordable with the available computational power.

In order to make the calibration of the fracture model more efficient, the mesh has to be made as coarse as possible while still having a converged stiffness. A series of biased meshes having less elements are cre-

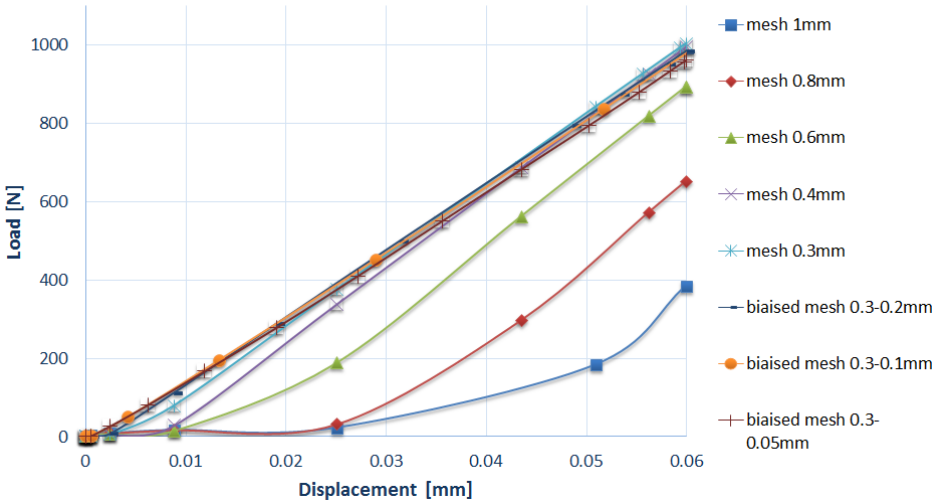

Figure 5.6: Load-displacement curves of test 5 model for different mesh sizes.

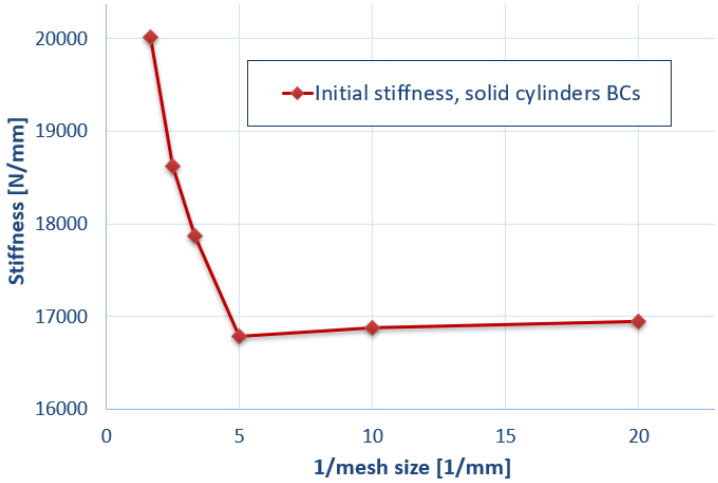

Figure 5.7: Stiffness of the test 5 model versus the inverse of mesh refinement.

ated, with elements of 0.2 mm at the critical locations but having bigger elements elsewhere. This choice stems from the fact that the model is mainly mesh sensitive around the boundary conditions contacts. For this study, the fracture model in between the plies is activated. This permits to identify the unacceptable meshes which undergo hourglassing in the elements under the loading nose, despite the hourglass control applied, when damage occurs. To sum up, the mesh which is sought for has less elements than the 0.3-0.2 mm one, has a relative error on stiffness lower than 3% with respect to the 0.3-0.05 mm mesh, and does not hourglass before final failure. Table 5.1 summarizes the performances of several new meshes which are investigated. The coarser mesh which does not show hourglassing while having an error in stiffness below 3% is the 0.6-0.2 mm mesh. This mesh halves the number of required elements and is therefore adopted.

5.2.5. VERIFICATION OF THE CHOICE OF ELEMENTS

In order to verify the choice of shell elements for this model, an additional cross-check with solid elements is performed. The current three-point bending test on a short specimen creates a mix of shear and bending loads on the structure. Abaqus manual warns that the transverse shear stiffnesses, or linear elastic stiffnesses of the shell in response to pure transverse shear strains, are computed for shell elements with a correction factor 5/6. This modelization is adapted to orthotropic homogeneous shells and are is particular invalid when shell section directions are not the principal bending directions.

Mesh size	Number of elements per ply	Error on linear stiffness	Hourglassing during full analysis
0.4-0.2mm	1750	0.50%	NO
0.5-0.2mm	1200	0.44%	NO
0.6-0.2mm	1080	0.53%	NO
0.7-0.2mm	850	1.11%	YES
0.8-0.2mm	644	1.31%	YES
0.9-0.2mm	546	1.33%	YES
1.1-0.2mm	374	3.57%	YES

Table 5.1: Summary of the test 5 model errors on stiffness and observed hourglassing effect, for different mesh seeds.

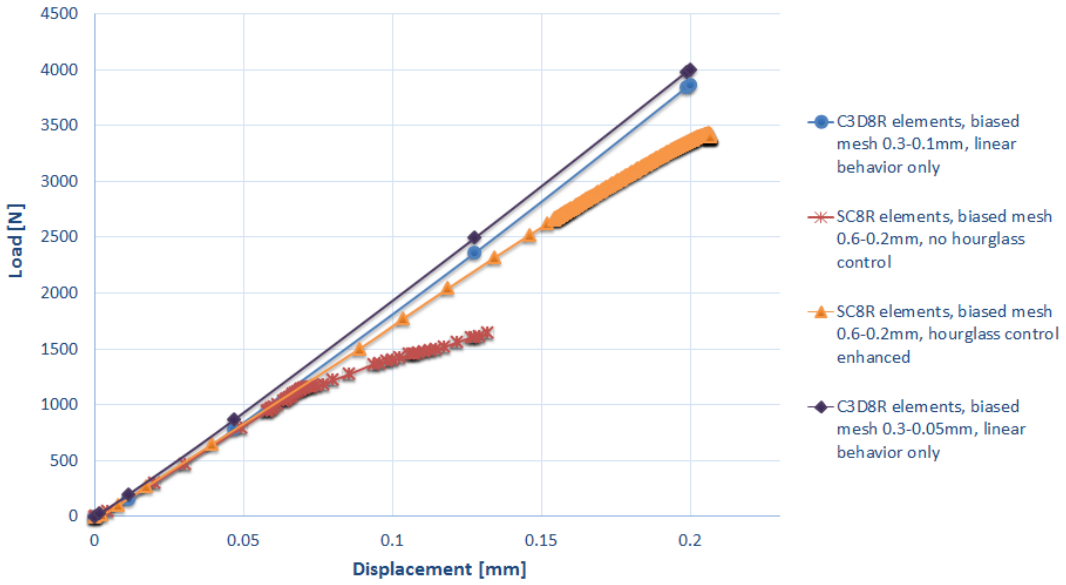

Figure 5.8: Linear response of the test 5 model with solid elements and total failure analyses with continuum shell elements.

A simple way to make sure the shell elements behave as expected in this specific test is to compare the converged linear stiffness obtained in the previous paragraph with the converged stiffness of the solid elements. For that purpose, the model is rebuilt with C3D8R elements. Disabling the fracture propagation, simulations are run for the mesh sizes: 0.3-0.1 mm and 0.3-0.05 mm. The results are plotted in Figure 5.8. The two curves have a slope difference of 0.2%; the mesh of the solid elements models is therefore considered as converged. The figure shows that the initial linear stiffness of both the solid elements and the continuum shell models is the same. In conclusion, the choice of continuum shell elements for the current model is justified.

The shell response for the optimum mesh is also shown in Figure 5.8 without activating hourglass control: since the initial slope of this curve is the same as the slope obtained with hourglass control, hereby justifying the for reliability of the computations done with enhanced hourglass control.

5.2.6. FINAL MODEL

As a conclusion, the model built for test 5 is composed of continuum shell composite layers with a cohesive contact between each of them. The boundary conditions are constituted of solid pins in contact with the laminate. It is necessary to apply hourglass control to the shell elements. The optimal mesh is biased and refined below the contact with the cylinders, with a size of 0.6-0.2 mm. The final model is represented in Figure 5.9. The calibration of the inter-laminar fracture model is performed in the next section.

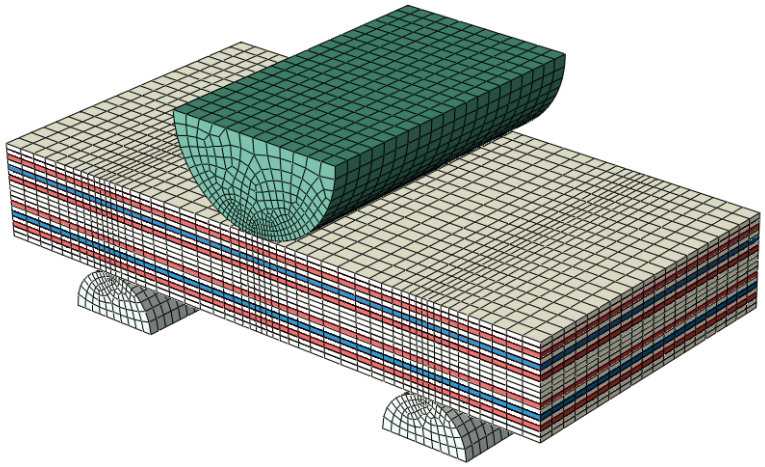

Figure 5.9: Final ILS numerical model, colored by parts.

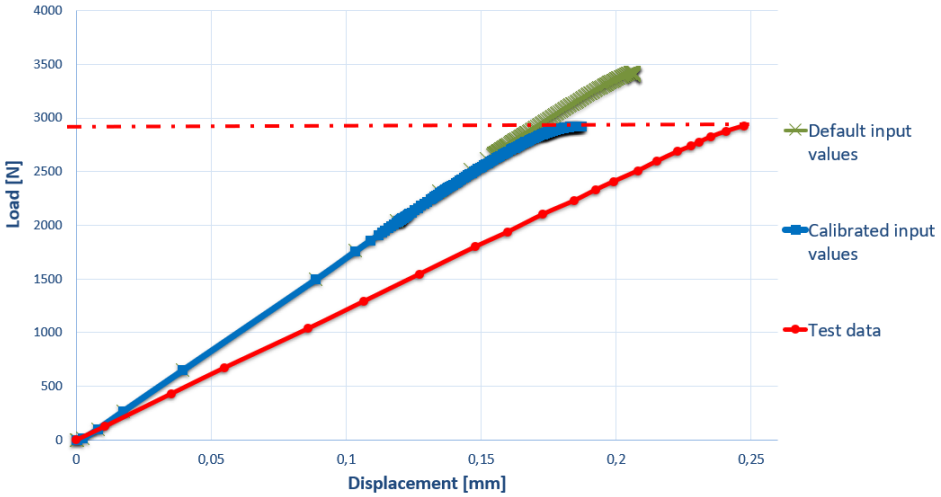

Figure 5.10: Results of the 5 together with the default and calibrated simulation results.

5.3. INTER-LAMINAR FRACTURE MODEL CALIBRATION

This section describes the calibration of the inter-ply fracture model. It is explained in section 5.1 that the test data provided only a failure load, since the measured displacement is not comparable to simulation results. Therefore, the calibration metrics are formulated in percentage of difference in the total strength. The calibration criterion is set to a maximum error of 15% in strength (see section 2.4) with respect to the maximum load value obtained from the test results of 2930 N/mm. Among the model input parameters listed in subsection 5.2.6, only X_{2t}, X_6, GT2 and G6 have to be optimized.

5.3.1. INITIAL RESULTS

Using the linear input parameters determined in chapter 4 and the initial contact inputs defined in Table A.1, the green response curve in Figure 5.10 is obtained. In this simulation, the maximum load is overestimated by 17%. In order to improve this result, the influence on the simulation of the contact input parameters other than K is studied. The model shows sensitivity exclusively to G6 and X_6, as it is expected for a bending test. Therefore, a modification of both these parameters can be performed to calibrate the fracture behavior.

5.3.2. INPUT PARAMETERS CALIBRATION

A short sensitivity analysis is conducted on G6 and X_6. At first, the shear fracture toughness G6 is modified alone. G6 has to be reduced in order to obtain the desired result. Since G6 defines the area underneath the

curve of the contact shear TSL, reducing too much its value would lead to a positive slope during the softening phase, which is physically impossible and leads to convergence issues. The minimum value of G6 appears to be $0.7 \cdot G6^0$, with $G6^0$ given in Table A.1. Even with this reduced value, the maximum load of the ILS simulation is not decreased enough to reach the experimental result.

A second series of numerical simulation is performed, fixing $G6$ at its initial value and reducing the value of X_6. A value of $0.8 \cdot X_6^0$ yields a fracture load of 2924 MPa, which means an error of 0.1% with respect to the experimental value. This result is represented by the blue curve in Figure 5.10. The error is negligible compared to the 10% indicative error allowable defined in section 2.4 and the strength value of $0.8 \cdot X_6^0$ is adopted. A composite solution reducing both G6 and X_6 would be possible, but more experimental results would be required to determine this type of solution.

Finally, the set 3 of optimized cohesive surface inputs is:

$$K = 3 \cdot 10^6 \text{ MPa} \tag{5.2a}$$
$$X_{6,calib} = 0.8 \cdot X_6^0 = 64 \text{ MPa} \tag{5.2b}$$
$$X_{2t,calib} = X_{2t}^0 = 76 \text{ MPa} \tag{5.2c}$$
$$\text{G6}_{calib} = \text{G6}_{calib}^0 = 0.79 \text{ N/mm} \tag{5.2d}$$
$$\text{G2t}_{calib} = \text{G2t}_{calib}^0 = 0.22 \text{ N/mm} \tag{5.2e}$$

5.4. CONCLUSION

This chapter described the calibration of the inter-ply fracture model, which is cohesive surface-based model. Its input parameters had to be optimized using a three-point bending test. The numerical model developed to correspond to the ILS test was complex. First, the layers were independently modeled and the cohesive surfaces had to be used at each interface. Additionally, it was proven that satisfactory results can be obtained if the pins are models by solid elements and are in contact with the specimen. The model is as well sensitive to mesh refinement and a convergence study was performed, followed by a verification of the chosen type of element.

Four interface strength and toughness parameters were subject to the optimization. The biggest limitation encountered in this BBV level concerned the improper test data: due to the position of the displacement sensor, spurious displacements, slips and test bench deformations were included in the output which therefore was unusable for comparison. The calibration was thereby performed using solely the final experimental strength. Since the three-point bending test fails under pure inter-laminar fracture, only the shear strength input could be calibrated. The final set of inputs is expression (5.2), and the error made in predicted strength is negligible. The next section provides recommendations to improve the fracture calibration procedure.

5.5. RECOMMENDATIONS FOR LEVEL THREE

Following the conclusion of this chapter, two main recommendations are formulated which could make the calibration of the surface-based cohesive behavior more complete and straightforward. The remark made on uncertainty quantification in subsection 3.5.1 is still valid here.

5.5.1. TEST SET-UP

As mentioned in section 5.1, the ILS test displacement measurements were not adapted for comparison with analysis. The first recommendation therefore concerns the position of the displacement or strain sensors, completing the remarks already made in subsection 3.5.3. The sensors must be placed on the specimen when possible or on the fixture which is the closest to the specimen. The amount of fixtures' relative slippage and test bench deformations included in the measurement is therefore limited. For the current three-point bending test, the displacement is recommended to be measured between the loading nose and the support, as close as possible to the specimen. Linear Variable Differential Transformers (LVDTs) could also be used. Otherwise, a strain measurement can be performed by placing two gauges on the laminate's surfaces.

5.5.2. RECOMMENDED SET OF TESTS

Since the three-point bending test triggers shear between the plies, this test is relatively well adapted to calibrate the shear-related inputs X_6 and G6. In order to calibrate the mode 1-related inputs X_{2t} and G2t, a test involving only mode 1 delamination should be used. For example, a double cantilever beam test would be adapted [27]. Two ILS and two double cantilever beam tests differing in layers orientation could constitute a valid set of tests for the calibration procedure. This corresponds to the minimum number of tests to create a determined problem and be able to calibrate the four input parameters. Additionally, it is recommended to keep the laminates' layups as simple as possible. This enables to identify more clearly the delamination onset and growth. The ILS test can for example be constituted of 0° plies and a minimum number of 45° plies in the center, as delamination is expected to occur at the interface between the 0° and the 45° plies.

The next chapter develops the validation procedure for the same cohesive surface-based fracture model.

6

Level Four: Validation of the Fracture Model

This chapter describes the level 4 of the BBV approach which is presented in section 2.3. The accuracy of the cohesive fracture model calibrated in chapter 5 is assessed using the OHC test of section 4.1.

As explained in section 2.3, this test is chosen among the set of available experimental data for the presence of its central hole which creates stress concentrations at free edges and therefore promotes delamination. However, intra-laminar damage is present as well and both damage and fracture must be modeled for this level. Morever, the damage model was partially validated with the same OHC test in chapter 4 and the quality of the results obtained in that chapter can only be fully assessed in comparison to the current complete model. This constitutes extra activities to perform. For this reason, the current validation step which models both mechanisms actually consists of a loop: the contribution of delamination to the failure process should be first identified in the current simulations, and this information should be used to make sure of the coherence of the results obtained in level 2. If necessary, the level 1 calibration process has to be refined. Afterwards, the inter-ply fracture model can be validated.

As detailed in the subsequent paragraphs, this strategy could not be conducted as expected due to difficulties in simulations convergence which could not be resolved within an acceptable time-frame. The test data is presented in section 4.1 and the numerical model developed for the current level is described in section 6.1. Subsequently, the validation procedure is detailed in section 6.2 where a convergence issue is identified and analyzed. Finally, a conclusion on the level 4 validation is drawn in section 6.3 and recommendation are provided for this chapter in section 6.4.

6.1. Test Four Numerical Model

This section describes the OHC numerical model used for the current level 4 validation. It takes as a basis the numerical model which is successfully used in level 2 and is described in section 4.2. The inputs correspond to expressions (4.1) and (5.2). The experimental OHC test which is to be compared to the model is presented in section 4.1.

6.1.1. Geometry, Boundary Conditions, Elements

In order to include delamination, it is necessary to modify the section 4.2 model and implement separately each layer of the composite layup, so that the cohesive zone contact can be used in-between each layer. The OHC specimen has 32 plies, which means modeling 32 different parts in the assembly and 31 cohesive surfaces. The plies are still made of continuous shell elements in order to be able to apply the Hashin damage model to each of them. The modified model and boundary conditions can be seen in Figure 6.1, and are detailed in Table 6.1. Hourglassing is detected in the different plies of the model, therefore the enhanced hourglass control is applied to each part.

The final reaction force is obtained by taking the total vertical reaction force on surface C in Figure 6.1. The final displacement is obtained with the vertical displacement of one of the surface C nodes.

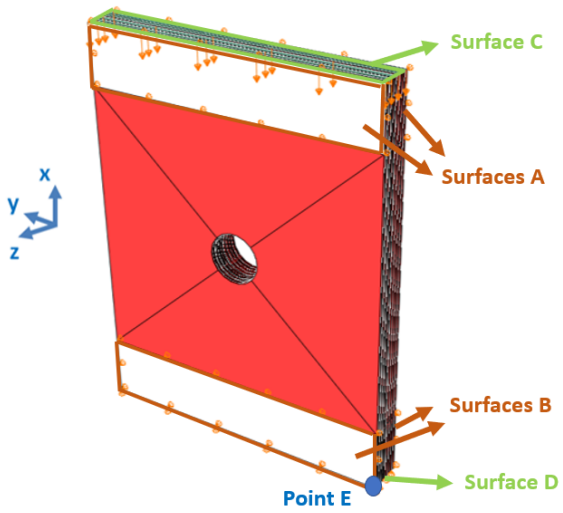

Figure 6.1: Numerical model and boundary conditions of the OHC test for level 4 validation.

Model	Region	Motion
OHC test for level 4 Figure 6.1	Surfaces A and B	$U_z = 0$
	Surfaces C	U_x applied (<0)
	Surfaces D	$U_x = 0$
	Point E	$U_y = 0$

Table 6.1: Summary of the boundary conditions and displacement applied to the OHC model in level 4. U designates a translational degree of freedom.

6.1.2. MESH DEPENDENCY

At first, the intra-ply damage model is not activated and the different plies are tied together in order to isolate the linear response of the specimen. As in subsection 4.2.2, the mesh convergence study is performed on the linear response. This phase is part of the model verification. The mesh convergence is evaluated in the like in subsection 4.2.2, using the strain concentration factor K evolution with mesh refinement.

Given the size of the model, there is too much computational power required for a simulation with a mesh seed smaller than 1 mm. Since stress concentrations are present around the hole, the results are expected to be mainly sensitive to mesh size in this region. Therefore, it is considered to used a biased mesh. A short series of simulations permits to verify that a mesh seed of 2 mm far from the hole and 1 mm around the hole gives the same result as an uniform mesh of 1 mm on the whole part. Therefore, it is assumed that introducing a bias with a smaller minimum mesh size is a good approximation of the results which would be achieved with the same uniform fine mesh. With the available resources, meshes down to 0.13 mm can be created around the hole. The K convergence results are shown in Figure 6.2, together with the convergence results which were obtained in subsection 4.2.2. Despite the differences in the level 2 and level 4 models, the mesh convergence follows a similar trend. The convergence error is defined the same way as in subsection 4.2.2. The error as a function of the mesh size for the present case is shown in Figure 6.3.

Taking the same mesh convergence criterion as in level 2, the acceptable error is under 5%. In the current case, this corresponds to obtain a strain concentration factor above $K = 3.1$, which means a biased mesh with a mesh seed size around the hole below 0.16 mm. The OHC model being built, the fracture and damage behavior are re-activated in order to perform the level 4 validation presented in the next section.

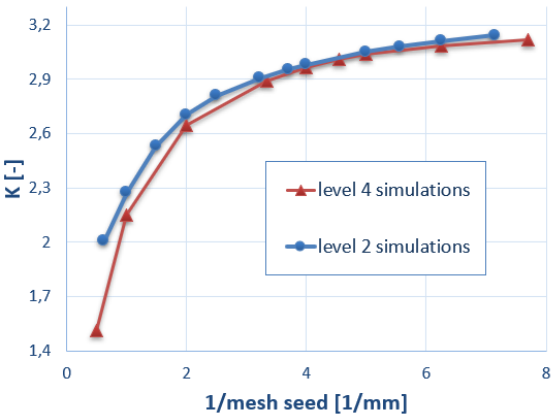

Figure 6.2: Strain concentration factor K of the OHC model versus the inverse of mesh seed size.

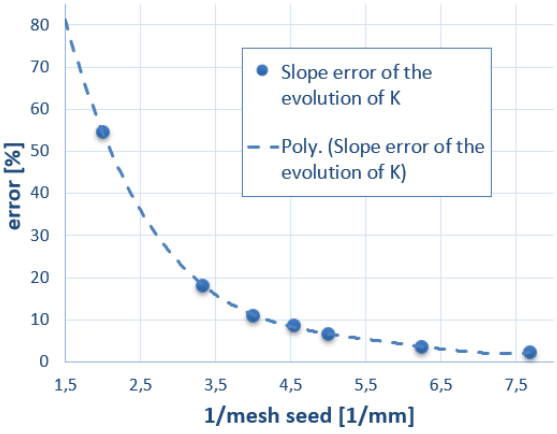

Figure 6.3: Error in slope for the evolution of K in the OHC model versus the inverse of mesh seed size.

6.2. CONVERGENCE ISSUES IN THE LEVEL FOUR VALIDATION PROCEDURE

This section describes the surface-based cohesive model validation approach. A convergence issue was observed during this procedure and is analyzed in the current section, together with a number of attempts to solve the problem.

6.2.1. INITIAL VALIDATION APPROACH

The purpose of level 4 is to evaluate the quality of both the calibrations performed in chapters 3 and 5, on a complex specimen. The current validation step therefore has to follow a specific procedure in order to clearly identify the contribution of damage and fracture in the final failure simulation. The preliminary step consists in making sure that the same results are obtained with the level 2 model (see section 4.2) and the current model when activating only intra-ply damage. Adopting a converged mesh, intra-ply initiation and propagation options are activated in each ply. The plies are simply tied together and fracture is not yet modelled. The failure simulation results are shown in Figure 6.4. The figure shows that the linear response of the level 4 simulation is 17% stiffer than the level 2 response and the simulation stops prematurely. The next subsections detail the origin of the convergence issue.

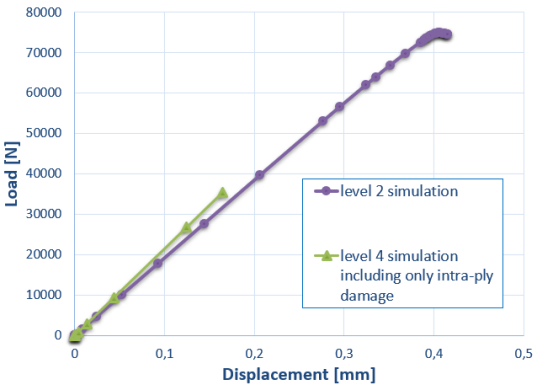

Figure 6.4: Load-displacement curves of the OHC model for level 4 and level 2 damage simulations.

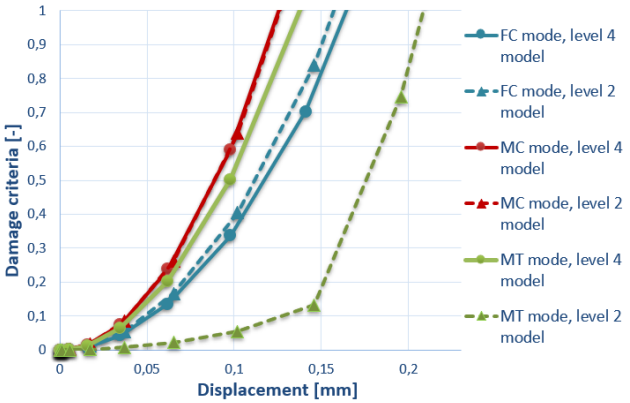

Figure 6.5: Damage criteria evolution of the OHC model for level 4 and level 2 damage simulations.

6.2.2. ANALYSIS OF THE CONVERGENCE ISSUE

In order to identify the differences between level 2 and level 4 simulations, which should give close results, the evolution of the damage initiation parameters are compared. The different damage outputs analyzed in this section are listed in Table B.1. The critical damage modes during the OHC test are FC in the 0° plies as well as MC and MT in the 45° plies. The evolution of the maximum values of the initiation parameters is shown in

Figure 6.5.

First, a significant difference is observed between the two models. The FC and MC damage initiations occur at the same time for both models, however there is a significant difference for the MT damage initiation. The model from level 4 undergoes matrix damage in the 45° plies before the same happens for the level 2 model. This stems from the fact that shear stresses around the hole are locally higher in the level 4 model. Since it is formed of multiple tied layers, an effect of local expansion or contraction is possible in the out-of-plane direction, especially for the outer layers. It results in a change in stress repartition at the location where damage is expected to occur, therefore this phenomena affects directly the damage initiation prediction. The deformation observed around the hole for the level 4 model appears to be more physically plausible than the ones obtained with the level 2 simulation.

From Figures 6.4 and 6.5, it is clear that the simulation for level 4 stops when the FC initiation parameter reaches 1. This means that convergence issues appear as soon as degradation in FC of an element occurs. It was already observed in section 4.2 that the specimen failure occurs soon after the full degradation of some elements in FC, as FC damage leads to an important stiffness reduction. However, when compared to the damage parameters evolution in level 2, the current damage state is not sufficient to truly correspond to total failure. While FC damage barely starts in a single element, the two other MC and MT damage parameters only reach a maximum value of 0.55 in very few elements around the hole. The reason why the level 4 simulations do not converge further than the initiation of fiber compression damage is therefore suspected to be caused by the important stiffness reduction underwent by the corresponding ply. This issue was not encountered during level 2 due to the layup defined in a single layer of elements using the Abaqus composite layup tool. In that model, each element stiffness is an average of all the layers' stiffnesses. Therefore, when a layer is damaged in a specific mode, the element's stiffness is only reduced by a limited amount, which avoids numerical instability. In the level 4 model, each layer is modelled separately, leading to an important and sudden stiffness reduction in an element when its corresponding ply is damaged in FC mode.

6.2.3. ATTEMPTS IN SOLVING THE CONVERGENCE ISSUE

In an attempt to improve the convergence of this simulation, the sensibility to a number of parameters is studied.

- First, stabilizing tools are used. It consists in introducing inertia or damping effects in different ways, so the equilibrium can be reached more easily. Increasing the number of cutbacks to 15 in the analysis, and starting with a small initial step of 0.001, default automatic stabilization in the step definition is used. Viscous stabilization is as well used in the Hashin damage module, but it does not yield an improvement in convergence.
- A dynamic, implicit, quasi-static step available in Abaqus/Standard is then introduced [10]. It uses a direct, implicit time integration to calculate the transient dynamic response of a system. For this analysis, materials have to be assigned a density, which is taken as the matrix material density. The mass, damping, and stiffness matrices are assembled and the equation of dynamic equilibrium is solved at each point in time. With this method, artificial damping is introduced using the default value recommended to permit the automatic time stepping procedure to work smoothly. The results obtained with the dynamic step are identical to the previous analyses.
- Since the analysis stops when energy dissipates through damage, the influence of the fracture toughness parameters GC1, GC2, GT1, GT2 defined in subsection 2.2.1 for the Hashin damage module is investigated. No influence is observed for either an increase or decrease of these parameters.
- Refining the mesh around the hole appears to worsen the convergence. It is as well verified that hourglassing does not have an impact on the analysis' results and convergence.

6.3. CONCLUSION

This chapter described an attempt to assess the performance of the inter-ply fracture model for a complex test. For this process, the lack of test data imposed to use another time the OHC test. The model developed for level 4 of the BBV approach was therefore based on the level 2 model (presented in section 4.2), with all the plies modelled separately and in contact through a cohesive surface. The mesh dependency study was

performed as well. The next step of verification consisted in comparing the results obtained with the current model, including only intra-ply damage, to the results of level 2. Convergence could not be achieved with Abaqus/Standard, despite numerous attempts. This stability issue was attributed to the high non-linearity occurring when the fibers of a ply start damaging.

Resorting to Abaqus/Explicit would be the last option. The time required to ensure a good definition of the OHC model and analysis using Abaqus/Explicit, followed by the validation process, is too important to be included in the current study. Additionally, using the OHC test for level 2 and level 4 results due to a lack of experimental data is not an ideal configuration and makes the validation procedure unnecessarily heavy. As it has been developed in the test data recommendations of each chapter, the BBV approach should make use of independent test results throughout the levels. The validation level 4 is therefore interrupted without a performance evaluation. The next section gives a number of recommendations based on the conclusions drawn about this validation level.

6.4. RECOMMENDATIONS FOR LEVEL FOUR

Following the conclusion of this chapter, two main recommendations are formulated with respect to the test data which would enable to perform the validation of the surface-based cohesive behavior.

6.4.1. RECOMMENDED SET OF TEST

It was repeatedly mentioned that having a combination of delamination and intra-ply damage does not constitute an appropriate way to validate the fracture model. The OHC test should therefore be used in an upper level of the BBV approach. Instead, the level 4 should simply be constituted of experiments which trigger pure delamination, involving modes 1, and mode 2 or 3. The former aspect is important to validate all the parameters involved in the cohesive surface model. For example, one can use the simple three-point bending and peel tests recommended for the fracture model calibration. As far as is it know in this study, changing the number of layers, the ply orientations and the specimen size should be sufficient to obtain a variety of responses which differ from the two calibration tests.

6.4.2. OVERCOMING CONVERGENCE DIFFICULTIES

The convergence issue encountered in this chapter came from the activation of intra-ply damage in a model whose plies are modelled separately. The severe discontinuities and softening which arise when single plies start getting damaged are too important to obtain convergence with Abaqus/Standard. This issue can be avoided for the level 4 fracture model validation when following the previous paragraph's recommendations, since intra-ply damage should ideally not be modeled at this stage. The problem can however still be encountered in sub-parts or part levels of a complex BBV approach, as soon as both damage and fracture together. For these cases, two solutions are possible:

- The plies can all be modelled separately and Abaqus/Explicit must be used to obtain the sample response.
- If the planes of delamination are identified, one can insert the cohesive surfaces at these locations only. Thereby, the layup is defined by groups of plies separated by a limited number of interfaces. Regrouping plies together with the composite modeler of Abaqus has a stabilizing effect and convergence can be obtained more easily, as it was the case in chapter 3 and 4 for example. This stems from the stiffness matrix averaging made on all the plies when very few of these plies get damaged.

Abaqus/Explicit would solve the issue through its direct iterative calculations. Abaqus/Standard, which has been used up to this point, gives a very good accuracy for nonlinear solutions and requires large time steps. However numerical stability is not ensured and in some cases, such as the current failure analysis, convergence cannot be obtained. The convergence difficulties are explained by the nature of the implicit integration scheme, which iterates until force equilibrium is reached. In the case of severe nonlinearity, difficulties can arise in obtaining convergence. Therefore, the explicit solver can be used, even if it recommended for linear problems. In the case of nonlinear analyses, the time increment required to have an accurate result may be extremely small, which makes the explicit analysis very time-consuming. Finding a good time step is an important question as well, since an inappropriate increment size leads to a drift in the solution. This stems from the fact that explicit solvers work on deriving the kinematic state from the previous increment, without

iterations.

The next chapter corresponds to the level 5 of the BBV approach, which models the delamination occuring in a whole stiffened panel during a compression test.

7

LEVEL FIVE: FAILURE SIMULATION OF A STIFFENED PANEL

This chapter describes the numerical results obtained with a complex failure simulation. It corresponds to the final level of the BBV approach presented in section 2.3. The test used for that level is a stiffened panel compression test. The panel corresponds to a scaled portion of Ariane 6's composite ViTF which includes a service hole, and is attached a portion of top-ring. The original ViTF structure is shown in Figure 1.1. The stiffened panel design, which was created in the frame of a previous research program by ADSNL and NLR, was meant to investigate the performance of AFP for curved stiffened geometries. The panel was tested in compression at NLR and the test results were made available for the current study. Since failure occurs by stringers' delamination, the performance of the fracture model calibrated in chapter 5 can be assessed by comparing the test data and simulation results.

Section 7.1 provides the specifications of the conical panel together with the experimental test data. The numerical model which is created based on the test set-up is explained in section 7.2. This chapter includes as well a validation of the numerical model's behavior excluding fracture. Finally, the validation of the failure results is performed in section 7.3, followed by the conclusion in section 7.4. In addition, recommendations concerning the test data are provided in section 7.5.

7.1. DATA FOR TEST SIX: STIFFENED PANEL TEST

This section describes the stiffened panel compression test and its results. The different parts composing the panel and the test set-up are reported in subsection 7.1.1. The results are listed and commented in subsection 7.1.2.

7.1.1. TEST DESCRIPTION

All the parts composing the panel were manufactured by AFP, which consists in laminating coated fibre material automatically onto or into a mandrel. This technology is a cost efficient way to produce large components and it enables the optimization of fibre architectures for the critical load cases of the component. The compression test was originally performed to validate the panel design and manufacturing methods. In order to lower the recurring cost, the panel which was tested in compression by NLR is stiffened through integral blade stiffeners instead of the original T-stringer concept proposed earlier during the research program. Moreover, in order to achieve the target strength performance defined during that program, the stringers were applied over the whole length of the panel. Therefore, the panel is composed of four stringer sub-laminates and a skin sub-laminate. The cost of this part was further reduced by the out-of-autoclave curing process used during manufacturing.

The geometry of the five sub-laminates is represented in Figure 7.1. Fillers made of 0^o material are used at the stringers' base. A filler can be observed on the panel's close view in Figure 7.7. The stringer sub-laminates all have the same layup. The different sub-laminates' layups are represented in Figure 7.2, where the angle α stands for the local ply orientation, which changes along the panel location accordingly to the AFP design.

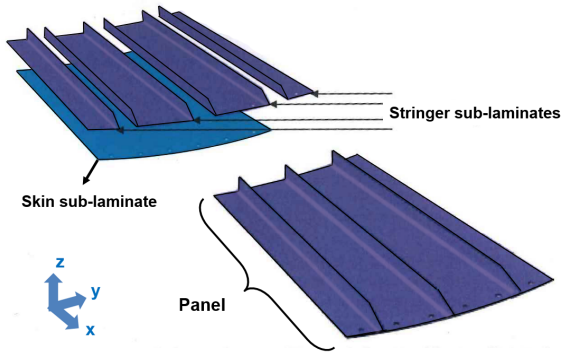

Figure 7.1: Exposed view of the sub-laminates in the stiffened conical panel and assembled panel.

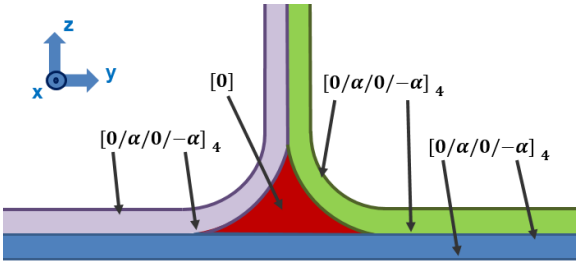

Figure 7.2: Layups definition for the two types of sub-laminates and the filler: the skin sub-laminate (in blue), the stringers sub-laminates (in green and purple) and the fillers (in red). The arrows give the layups orientations by indicating which plies are the outer ply for each sub-laminate.

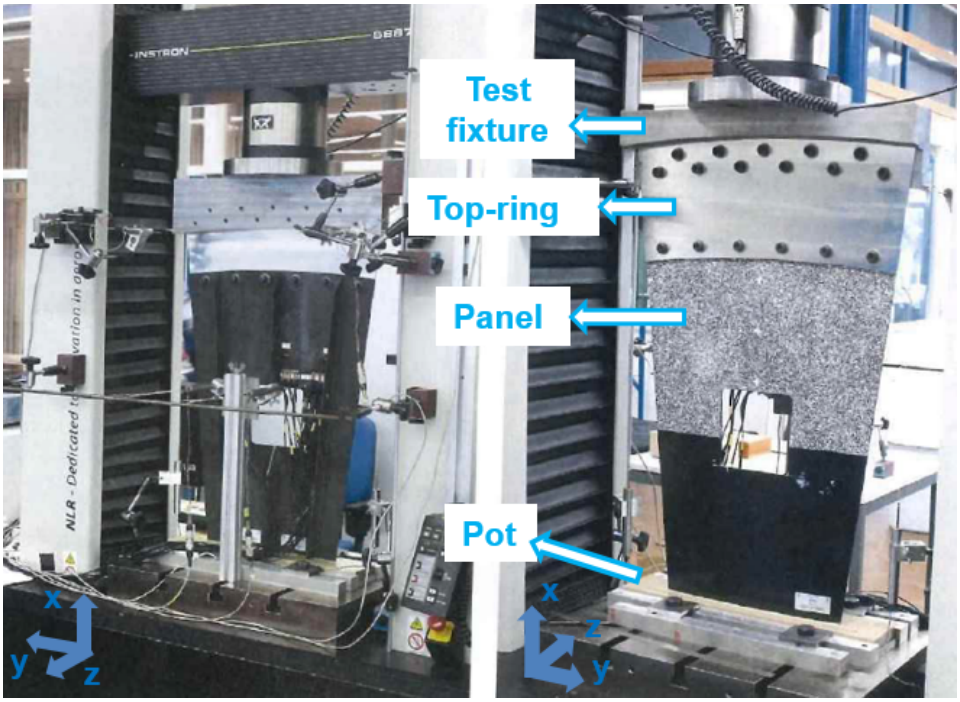

Figure 7.3: Experimental set-up of the stiffened panel compression test. The panel, top-ring, pot and test fixture are visible, as well as the test bench, LVDTs and pattern for digital image correlation.

This angle is 52º at the largest panel radius, which is the top of the panel in Figure 7.3, and 45º at the smallest panel radius, which is at the bottom end in the Figure. Once the sub-laminates have been assembled, the total skin layup is symmetric. On the stringer webs, the layup is balanced but asymmetric because of the angle plies.

A picture of the compression test set-up is shown in Figure 7.3. As visible on the Figure, the panel includes a service hole. At the bottom of the panel, which corresponds to the smaller radius region, the panel is cut straight and potted in polyurethane resin (permacol 5133) of dimensions 54/11/2.5 cm. The pot is clamped at the lower bed of the test bench of the 300 kN Instron 5887 machine used for the test. The top of the panel is attached to an aluminium panel using six 12 mm H7 bolts. This aluminium skin represents the top-ring connected to the Engine Thrust Frame (ETF), and is itself attached to a rigid steel test fixture with eleven M10 bolts. The same 45 Nm torque is applied to all the bolts. The test consists in applying a compressive displacement at the test's fixture while recording a number of parameters up until final failure. Final failure is reached when the reaction load recorded at the test fixture has dropped by 5% of the maximum load.

7.1.2. TEST RESULTS

The results of the tests carried at NLR consist of the measurements listed below, using the sensors shown in Figure 7.4:

- In-plane and out-of-plane panel displacements are measured at the upper test fixture, using LVDTs. Out-of-plane displacement is measured as well on the skin around the service hole. The corresponding displacement/load curves during the failure test are shown in Figures 7.5 and 7.6.
- Visual inspection of the panel is performed after testing. Two cracks are observed at the outer stringer run-outs. A close view of the left-hand stringer (with respect to Figure 7.4) run-out is shown in Figure 7.7.
- Out-of plane displacement fields were recorded, using a 3D Digital Image Correlation System called Aramis. The displacement fields up until the first failure are shown in appendix G.
- Strains are measured using linear strain gauges and rosette strain gauges. The microstrain/load curves obtained during the failure test are shown in appendix G.

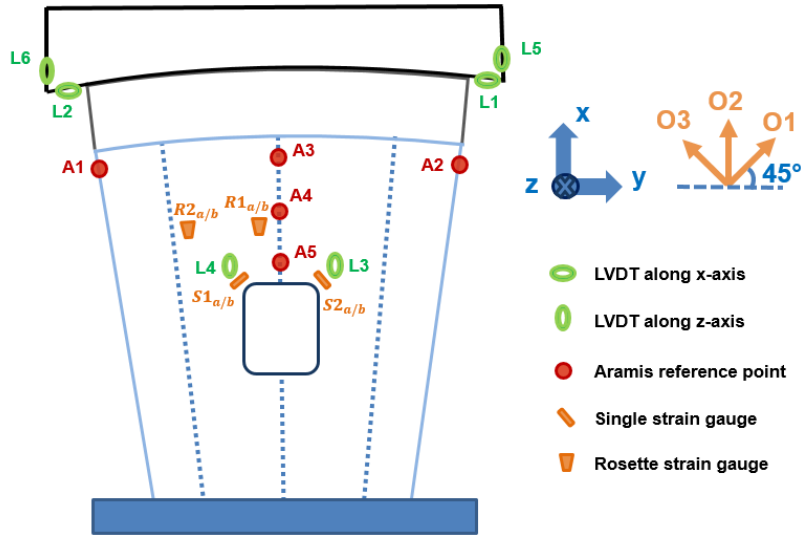

Figure 7.4: Position of all the sensors for the panel failure test viewed from the side opposite to the stringers.

A few remarks are made about the test results. First, a maximum positive displacement of 0.85 mm (L5) and 0.9 mm (L6) is noticed in Figure 7.6. It comes from the bending moment present between the test bench and load cell. The difference in displacement indicates an asymmetry in the out-of-plane displacement. It is reported by NLR that a first crack is heard at 61 kN and that the maximum load reached during testing is 64.4 kN. At that point the outer stringer, which is on the left-hand side of the Aramis field view, failed at the stringer run-out. The second outer stringer delaminates at 62.8 kN. The fracture behavior is therefore asymmetrical, most likely because of the angle plies present in the layup, combined with the panel's curvature. The Aramis fields show a large amount of bending in the panel. Moreover, the Aramis fields show an asymmetry in the bending panel, which is coherent with the fact that fracture initiates first on one side. Finally, the visual inspection of the panel after testing reveals that delamination occurred at the interface between the stringer's laminate and the skin's laminate for the two outer stringers. No damage is observed at the service hole. The interpretation of this failure mode is given by NLR, which suspects that the high stiffeners run-out angle (35°) introduced a stress concentration at the stiffeners' end combined with the high peel stress present due to the panel bending.

In summary, this set of available data indicates that the structure significantly bends towards the stringers side because of the load introduction method. It finally fails by delamination at the outer stringer run-outs in an asymmetrical manner. In addition, it is important to notice that the test fixture itself had an asymmetrical out-of-plane motion during the test. The numerical model which is developed to simulated this panel compression test is described in the next section.

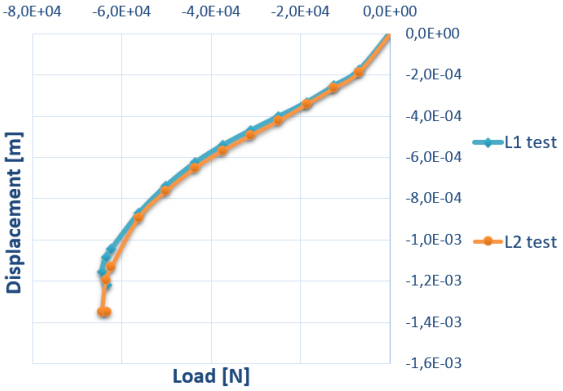

Figure 7.5: Load-displacement curves of the panel compression test obtained as output of LVDTs L1 and L2, as defined in Figure 7.4.

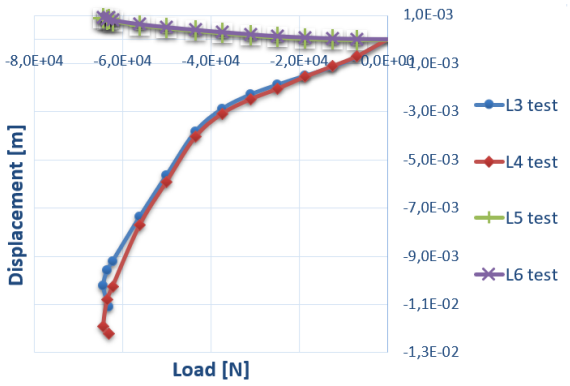

Figure 7.6: Load-displacement curves of the panel compression test obtained as output of LVDTs L3 to L6, as defined in Figure 7.4.

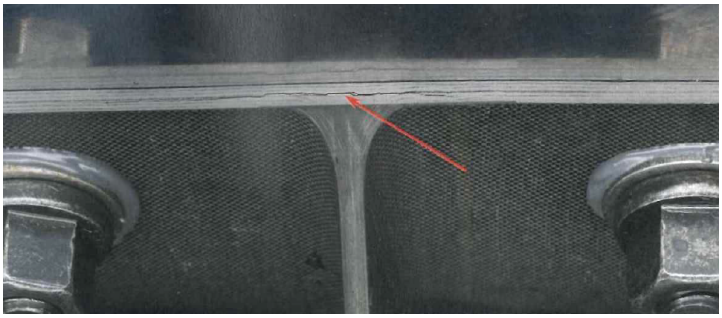

Figure 7.7: Panel failure at the stringer run-outs of the two outer stringers.

7.2. TEST SIX NUMERICAL MODEL AND VALIDATION WITHOUT INCLUDING FRACTURE

This section describes the construction, verification and validation of the numerical model for the panel compression test. The delamination is not implemented yet in order to clearly identify the model's performance before damage. The numerical model is composed of the panel and its service hole, the pot, the aluminium ring and the top test fixture, which are described in subsection 7.2.1. The bolts pre-loading requires a specific procedure justified in subsection 7.2.2. The choice of elements for the different parts and the mesh convergence study are performed in subsection 7.2.3 and 7.2.4. The influence of the pot is assessed in subsection 7.2.5, in order to estimate the error made with equivalent boundary conditions. Finally, results of this model are presented in subsection 7.2.6 only for applied displacement below the displacement at which the first crack is expected to occur. A short conclusion is drawn in subsection 7.2.7.

7.2.1. MODEL GEOMETRY, ASSEMBLY AND BOUNDARY CONDITIONS

First, the four stringer laminates, the fillers and the skin laminate are modelled with solid sections. The layups are implemented using the composite modeller available in Abaqus. In order to easily account for the variation in angle α along the x-axis due to the AFP manufacturing, the panel section is cut into six regions which each have a different value of α. The value adopted for each region corresponds to the average between the angle at the lower and upper parts of the region. From bottom (the potted end) to top (the end going to the top-ring), the six different α angles are taken as: 47.6º, 49.17º, 50.32º, 51.13º, 51.64º, 51.86º. The four filler parts are modelled separately and are assigned the material property of the unidirectional lamina, with the fibers parallel to the filler lengths. The aluminium top-ring is modeled with a solid section as well. The Young's modulus used during previous analysis at ADSNL is used in the current model: $E_{topring} = 72$ GPa. All the model's parts and their partitions are shown in Figure 7.8.

It is decided to model as many parts of the set-up as possible, which means that both the clamped pot and the upper test fixture are modelled. This choice is made since NLR test results reveal a large amount of

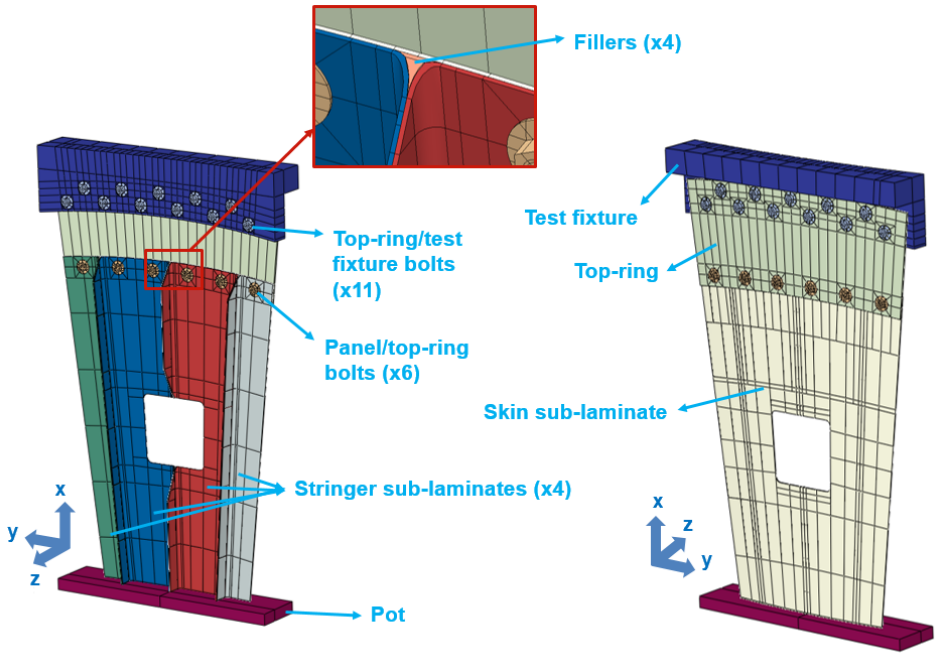

Figure 7.8: Final panel model's 29 parts and their partitions.

bending in the panel, on which the test fixtures' out-of-plane displacements could have a significant influence. In addition, modeling the whole upper test fixture permits to measure the vertical displacements at the same location as it is performed in reality.

The pot is modelled by a rectangular solid section. The material is a type of polyurethane whose Young's modulus is not precisely known, therefore a typical value of 69 GPa is chosen. The panel is embedded in the pot through the embedded region constraint, which permits to connect the degrees of freedom of the hosted structure's nodes with the degrees of freedom of the host structure's nodes. The region of host nodes concerned with the constraint is defined by a "radius" around the hosted region [10]. This constraint is shown together with the other constraints of this model in Table 7.2.

The steel test fixture is modeled with a solid section using steel material of Young's modulus $E_{steel} = 200$ GPa, as used during the previous analysis at ADSNL. During the test, a compressive displacement is applied at the top of this part. The boundary conditions applied to the pot and test fixture are represented in Figure 7.10 and are listed in Table 7.1.

Finally, each part possesses holes for the bolted connections with the other parts. All the holes are 12 mm large, apart from the test fixture holes which are 10 mm. The bolts used for the connections are modeled using solid sections and are assigned the same steel material as the upper test fixture. Both types of bolts used in the model are shown in Figure 7.9.

Once the parts are assembled, several ties and contacts have to be applied. These constraints are summarized in Table 7.2. The master/slave assignment for the ties between the skin laminate, stringer laminates and fillers are shown in Figure 7.11. It avoids to have two conflicting master nodes for a single slave node. The panel and top-ring, as well as the top-ring and test fixture are in contact.

7.2.2. STRATEGY FOR PRE-LOADING AND CONTACTS OF BOLTS

The first simulationsaim to determine the best strategy to enforce the bolt's pre-load. First, the torque value of 45 Nm which is applied on each bolt has to be converted into a pre-load value. A simple way to estimate the torque is [28]:

$$T = K \cdot F \cdot d \tag{7.1}$$

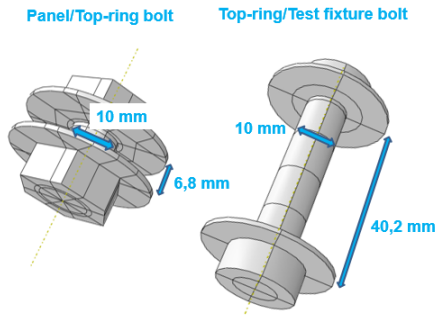

Figure 7.9: Geometry of the bolts connecting the panel to the top-ring and the top-ring to the test fixture.

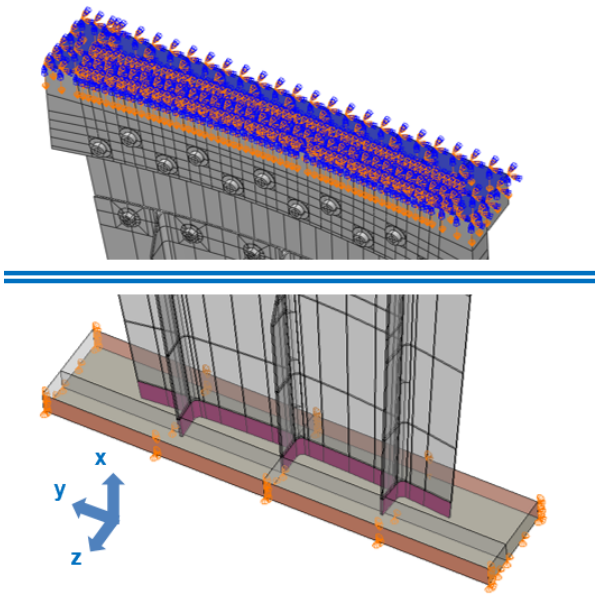

Figure 7.10: Boundary conditions applied to the test fixture and pot during the panel compression simulation's load step.

Region	Motion	Steps
Pot, lateral surfaces	$U_y = 0$, $U_z = 0$	1, 2, 3
Pot, bottom surface	$U_x = 0$, $U_z = 0$	1, 2, 3
Test fixture, top surface	$U_y = 0$, $U_z = 0$	1, 2, 3
Test fixture, top surface	U_y applied, smoothly	3
Bolts, mid-surfaces	$U_x = U_y = U_z = 0$	1, 2
Bolts, mid-surfaces	Pretension 22500 N	1
Bolts	Fixed length	2, 3

Table 7.1: Summary of the boundary conditions and displacement applied to the panel's model and the steps at which they are applicable. The content of each step is justified in subsection 7.2.2. *U* designates translational degrees of freedom.

Region 1 (master)	**Region 2 (slave)**	**Type**	**Specifications**
Skin sub-laminate	Stringers sub-laminates	Tie	Finite sliding
Fillers	Skin sub-laminate	Tie	
Stringer sub-laminates	Fillers	Tie	
Stringer sub-laminates	Stringers sub-laminates	Tie	
Test fixture	Bolts' washers	Tie	Surface-to-surface contact
Top-ring			
Skin sub-laminate			
Skin sub-laminate	Top-ring	Contact interaction	Finite sliding Surface-to-surface contact Normal: "Hard" contact Tangential: friction coefficient 0.2
Test fixture	Top-ring	Contact interaction	
Panel	Pot	Embedded region	-

Table 7.2: Contacts and interactions used in the stiffened panel's model.

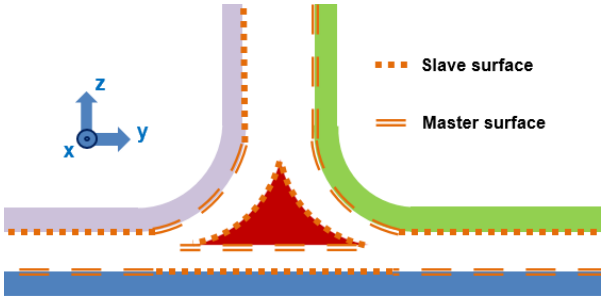

Figure 7.11: Assignment of the master/slave roles on each surface of the stiffened panel.

With T the torque, K the nut factor (which is a constant depending on the bolt geometry and material), F the pre-load force and d the bolt diameter. Using the bolts' diameter of 10mm and a coefficient K of 0.2 as it is common for dry mild-steel bolts, the pre-load is estimated to be 22500 N.

Enforcing the pre-load is made simple in Abaqus, using a bolt load with prescribed pretension. The bolt mid-section must be entered in the software following which Abaqus adjusts the length of the elements on one side of the surface to achieve the prescribed amount of pre-tension. Applying this pre-load to the bolts at the beginning of a loading step leads to a singularity error due to rigid body motions. A solution is proposed by Krolo, Grandić and Bulić [29]. The authors suggest to follow a strategy which, adapted to the current case, is divided into three analysis steps (this strategy is summarized in Table 7.1):

- Step 1: apply the bolt load at the bolts' mid-section, as well as applying an artificial pinned boundary condition on the same section in order to prevent rigid body motion. In addition, for all the analyses, the contacts panel/top-ring and top-ring/test fixture are applied and the translation of the test fixture's upper surface is restrained in y and z directions.
- Step 2: remove the artificial boundary condition and transform the bolt's pre-load command into a fixed bolt length command. The fixed length helps to avoid problems of extensive elongation of the bolts under external loading.
- Step 3: apply the external loading.

A choice has to be made regarding the contact type between the bolts' washers and the plates. At first, an attempt is made with the same contact definition as the one used between the panel and top-ring. This leads to a significant increase in computational time and during which the bolts slip significantly with respect to the plate they are in contact with. This is not a desired result, since on the actual panel after testing, the washers are glued to the panel and therefore they cannot slip. It could still be possible to have a relative slip of the bolts' nuts with respect to the washers. However, the test panel does not show any trace of damage or deformation around any hole, which indicates that the bolt shafts most likely did not come into contact with the holes. In addition, a relative slip of the nuts should be represented by a jump on the final load-displacement curve. This jump should be present after a few tenths of millimeters of applied displacement, since relative slip occurs after reaching a limit force depending on the coefficient of friction. As no such jump is observed, it is assumed that the applied torque was sufficient to avoid bolt slippage during the test.

For these reasons and in order to reduce the calculation time, the washers are tied to the adjacent surfaces, as is summarized in Table 7.2. In this configuration, steps 1 and 2 require only one iteration each.

7.2.3. CHOICE OF ELEMENT

Once the geometry is defined, a type of element has to be chosen for each part constituting the model. The parts which are bulky and are not expected to bend a lot (namely the steel test fixture, the steel bolts and the pot) are chosen to be modelled with linear solid elements C3D8R. The parts constituting the panel and the top-ring, on the other hand, bend significantly during the simulations. Because of the Abaqus' definition of composite layup for solid sections, only one layer of elements is allowed throughout the thickness. One has to make sure that the chosen elements perform well in bending, as the panel was shown to deform mainly

under bending during the experimental test.

A short comparative study is performed on a thin square plate under pure bending: clamped at one side, a displacement is applied at the other. The material is the same layup as the panel's skin. For this geometry, three types of elements are compared, namely linear solid elements (C3D8R), quadratic solid elements (C3D20R) and their fully integrated counterparts (C3D20), as well as continuum shell elements (SC8R), for a 10x10 elements mesh. This mesh only has one layer of elements throughout the thickness. The resulting load-displacement curves at the plate loaded end are shown in Figure 7.12.
The shell elements are used as a reference, since this type of element is known to perform well for simple bending situations. As expected, the linear solid elements yield a very flexible response. Reduced-integration, first order solid elements cannot accurately capture curvature due to the position of their integration point: it leads to hourglassing. C3D8R are therefore not adapted for the panel model. Likewise, C3D8 yields a high stiffness due to shear locking effect, which is caused by the numerical formulation of the elements giving rise to artificial shear strains. On the other hand, the second order solid elements show an equivalent performance to the shell elements.

In order to choose between the three remaining types of elements SC8R, C3D20R and C3D20 for the panel's elements and the top-ring, three simulations using each element type are conducted. The mesh is chosen to be uniformly fine (mesh seed size: 4 mm) in order to avoid hourglassing. It is verified that this mesh corresponds to a converged behavior for the three types of elements. The reaction force versus applied displacement curves are plotted in Figure 7.13. In the case of the shell elements simulation, the top-ring is modelled with C3D20R elements while the skin is modelled with shells. This choice stems from the difficulty to enforce the contact between a shell skin and a shell top-ring. The curve reveals that the shell model behaves stiffer than the two solid models. In the present bending problem, the desired solution is the most flexible result possible. Shell elements are therefore excluded. Additionally, since the fully integrated quadratic elements give the same results as the reduced integrated ones and require much more computational power, full integration is excluded.

As a conclusion, the quadratic solid elements C3D20R are chosen for their performance in bending and their relative computational efficiency. C3D20R is used for the panel elements and the top-ring. The pot, bolts and test fixture are modeled with C3D8R elements and it is verified that the results obtained with C3D8R for these parts are equivalent to using C3D20R.

7.2.4. MESH CONVERGENCE STUDY

One of the last steps before validating the behavior of the elastic panel is to decide on a mesh size which would be small enough to obtain a converged behavior, while being computationally efficient. The simulations are mainly mesh sensitive for bending parts: for all the following simulations, fixed mesh seeds of 20 mm for the pot and 8 to 15 mm for the text fixture are used. Likewise, the bolts have a mesh seed of 1.5 mm. It is verified after the mesh convergence study that the results are not sensitive to these parameters.

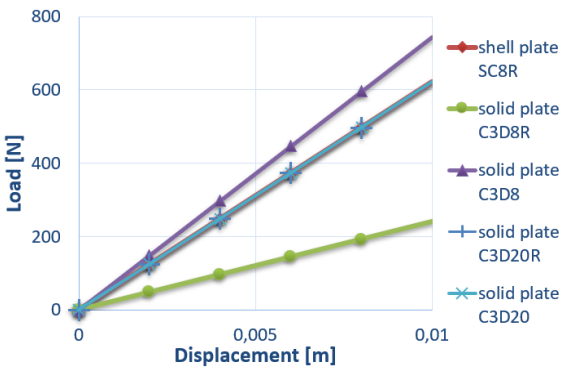

Figure 7.12: Bending plate's load-displacement curves for five different types of elements.

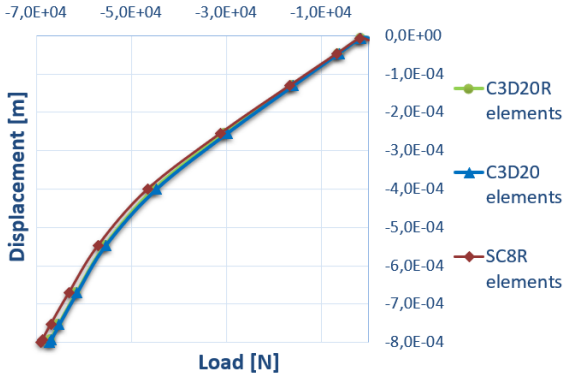

Figure 7.13: [Load-displacement curves of the panel model for different element types SC8R, C3D20R and C3D20, applied to the panel and top-ring.

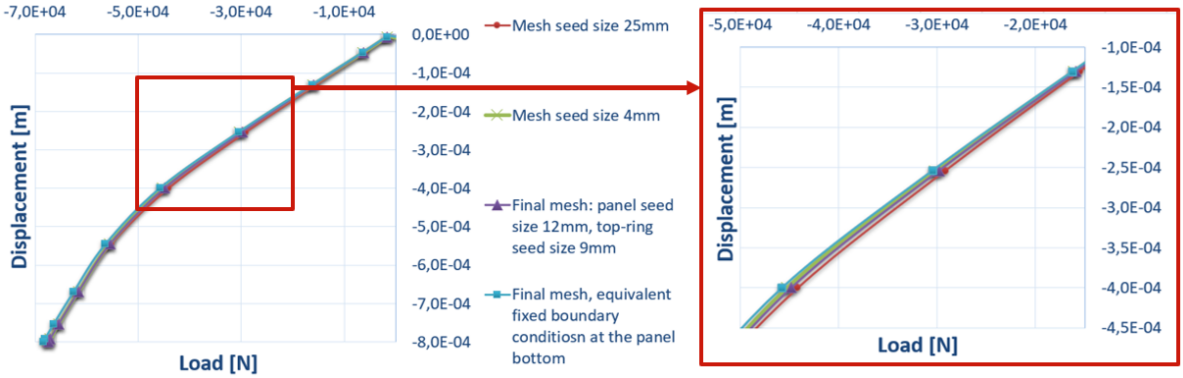

Figure 7.14: Load-displacement curves for different mesh seed sizes applied to the panel and top-ring and load-displacement curve for the equivalent bottom boundary condition

Several uniform mesh sizes are applied to the panel's parts and the top-ring. Some load-displacement results are shown in Figure 7.14. Each curve clearly shows two different sections, which can each be approximated by a linear curve. For the mesh convergence study, the only noticeable difference between the curves lies in the slope of the first section. From a mesh size considered as fine (4 mm) to a coarse mesh (25 mm), there exists a difference of only 3.5% in slope. The model is therefore almost insensitive to mesh size for the range of meshes considered. It is decided to choose a mesh as coarse as possible but which permits to have a uniform element distribution given the necessary partitions which exist on the parts. The final mesh size is therefore 12 mm for the panel parts. A mesh size of 9 mm is used for the top-ring. The errors with respect to the 4 mm mesh load-displacement curve are 1.5% for the first slope and 0.9% for the second slope. Both errors are reasonable. The typical displacement field obtained with the final model is shown in Figure 7.15.

7.2.5. INFLUENCE OF THE BOUNDARY CONDITIONS

Once the model is verified, the influence of the pot boundary conditions are studied in order to know the relevance of modelling the pot. Modeling the upper test fixture, on the other end, is judged necessary in order to compare the LVDTs measurements made by NLR.

Using the selected final meshes and replacing the pot embedded region by fixed boundary conditions, the resulting load-displacement curve is shown in Figure 7.14. Compared to the results obtained for the model using the final mesh and the pot embedded region, the errors in slope for both the first and second linear regions are 2% and 1.2% respectively. The errors being below 2% are considered very low considering the absence of uncertainty evaluation. Therefore, using the equivalent boundary conditions is a reasonable choice. As a conclusion, the equivalent fixed boundary conditions can be used during the verification of the heavy fracture analyses, in order to alleviate the numerical model.

7.2.6. ELASTIC RESPONSE

The results obtained with the previously verified model are compared to the experimental curves given by L1 and L2 (see Figure 7.4 for the sensors position). The data has to be compared for a load below 60 kN, which is the load after which fracture occurs during testing. An artificial initial softening is present on the original NLR data curves, as it can be seen in Figure 7.16. This effect is due to initial relative motions between the different parts of the test set-up when the test starts. Therefore, the L1 and L2 curves should be extrapolated before 0.2 mm of applied displacement. In order to visually compare the numerical results with the experimental ones, the extrapolated L1 curve is shown on the picture.

First, both the experimental and the numerical results show two distinct quasi-linear sections, which means that the analysis follows the structural behavior observed in reality. The change in slope occurs when the two outer stringers' webs start to buckle and have a displacement component in the y direction. The similarity is confirmed by the shape of the displacement field observed in Figure 7.15 and in the Aramis displacement fields before fracture in Figures G.2a and G.2b. The fields show an asymmetry which is likely due

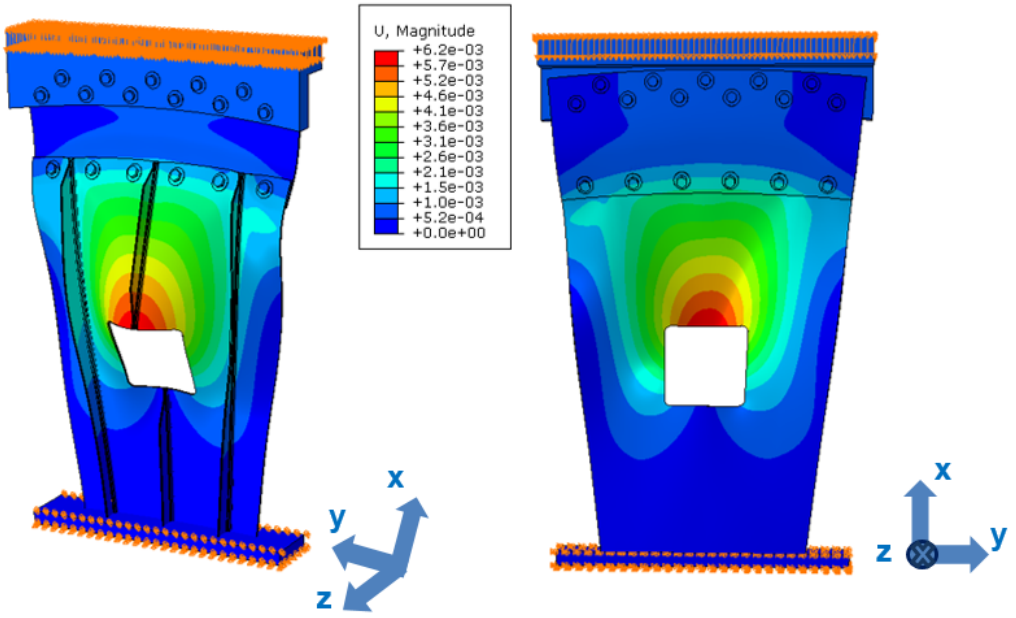

Figure 7.15: Displacement field and boundary conditions of the final panel model during step 3, for an applied compressive displacement of 5.5 mm and a reaction force of 55.3 kN.

to the panel's curvature combined to the layup stacking sequence. This asymmetry is observed as well on the analysis result and its presence is essential to later simulate initiation of the the asymmetrical delamination.

On the other hand, there exists a clear difference in panel flexibility between the test and the analysis. Comparing the Aramis measurements with the simulation, for a reaction load of 60.2 kN, a difference of 25% exists between the maximum out-of-plane displacement of the numerical model and the test results. Even if this error is expected to be lower when fracture will be added to the model, the model still behaves significantly stiffer than the real panel. Moreover, in Figure 7.16, the error in slopes between the numerical result and the L1 and L2 outputs are 20% for the first curve region and 4% for the second region. The L3 and L4 outputs are compared in Figure 7.17. The errors in slope are on average 45% for the first curve region and 4% for the second region. Several hypotheses are formulated to explain the observed discrepancies in flexibility:

- The second-order C3D20R elements used for the panel parts cannot be used with more than a single layer in thickness, as explained in paragraph 7.2.3. There are also no third order elements available which could help increase the number of integration points. Therefore, the flexibility through the thickness is restricted and is expected to have an influence on the final result.

- The model only approximates the composite layup. The fiber angle α is implemented in 6 homogeneous horizontal regions across the panel, instead of modeling the angle variation continuously. This is expected to change the stress repartition in the panel, especially on the upper part. This together with the restriction in integration points through the thickness are probably the main sources of error for the L3 and L4 results. These two outputs are monitored on the panel itself and cannot include the next set of issues.

- The eventual slippage which can occur between all parts during the test is not modeled, since the bolts are tied to the different surfaces. On top of that, the test bench rotates during the test, as is recorded by the two out-of-plane LVDTs L5 and L6 in Figure 7.6. On the contrary, the model does not show such a behavior since the out-of-plane displacement of the modeled test fixture at the L5 and L6 locations does not go above 10^{-3} mm.

- The panel manufacturing imperfections cannot be modeled and there are many defects expected with the out-of-autoclave process. This influences the final panel bending behavior to an unknown extent.

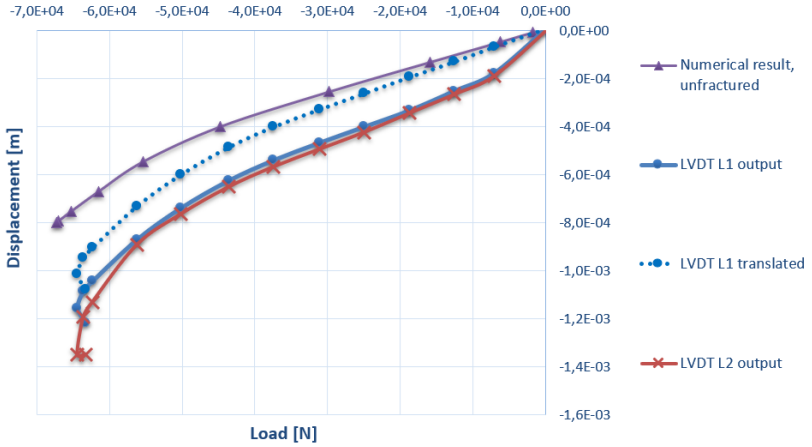

Figure 7.16: Load-displacement curves of the elastic panel compression simulation together with the experimental outputs of L1 and L2. L1 and L2 simulation outputs are identical.

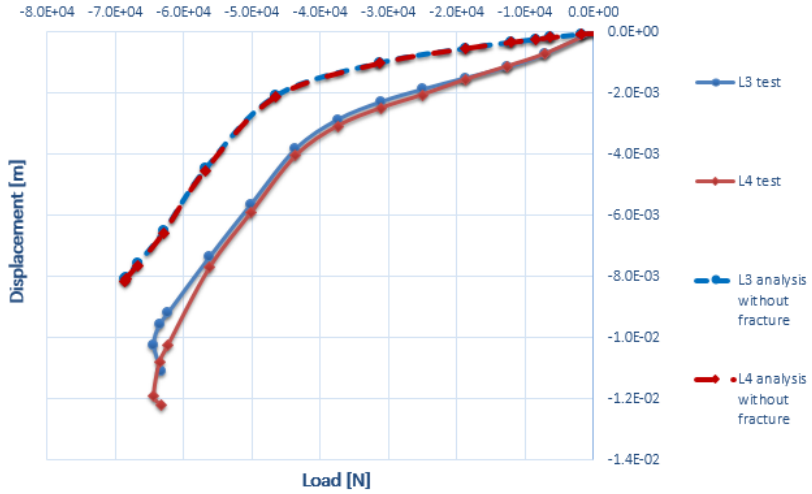

Figure 7.17: Load-displacement curves of the elastic panel compression simulation together with the experimental output of L3 and L4.

7.2.7. CONCLUSION ON THE SUITABILITY OF THE ELASTIC MODEL

Despite the stiffness differences, the analysis results are judged satisfactory given the bending modes observed on the panel, including the asymmetry and the displacements orders of magnitude. Moreover, the shape of the load-displacement curve is satisfactory and the necessary calculation time is reasonable. A possibility to improve the bending response would be to avoid using the composite modeller of Abaqus. This would enable to use several layers of finite elements through the thickness and obtain a more flexible behavior. It would however require to define the composite layup as an equivalent laminate, using the classical lamination theory. It additionally requires the validation of the code implemented. Using an equivalent laminate by defining the engineering constants results as well in a loss of information: the composite stacking sequence is not taken into account and both skin and stringer sub-laminates would have the exact same material definition. The panel would therefore bend in a symmetrical manner.

For this study, the objective is mainly to evaluate if the cohesive surfaces implemented in Abaqus can provide delamination results similar to the experimental ones, for a complex loading case. There are not precise validation criteria defined for this level of the BBV approach. Therefore, for this comparison, it is chosen to keep this numerical model even if the it lacks flexibility. The model and the test still have the same general bending behavior and the out-of-plane asymmetry is modeled to a certain extent.

7.3. VALIDATION OF THE SIMULATED FRACTURE BEHAVIOR

This section has for purpose to describe the validation of the final panel model which includes fracture. In subsection 7.3.1 are described the modification introduced in the model to simulate fracture. The comparison of the analysis with the test results is performed in subsection 7.3.2.

7.3.1. NUMERICAL MODEL FOR FRACTURE ANALYSIS

The base model before fracture implementation is described in section 7.2. The main modification required to model fracture is to introduce cohesive surfaces at the skin sub-laminate/stringers sub-laminates and skin sub-laminate/fillers interfaces. These replace the tied constraints listed in Table 7.2. As a reminder, the description of the inter-ply damage model is in subsection 4.2.2. The inputs used for the current simulations correspond to the optimized elastic inputs of expression (3.1) and the optimized strength inputs of expression (5.2). As justified in subsection 7.2.5, equivalent fixed boundary conditions are used at the panel bottom. The mesh is adapted to the fracture analysis by refining the zones where fracture is observed during the analysis. This final mesh can be seen in Figure 7.18. The maximum mesh size is the one determined in subsection 7.2.4.

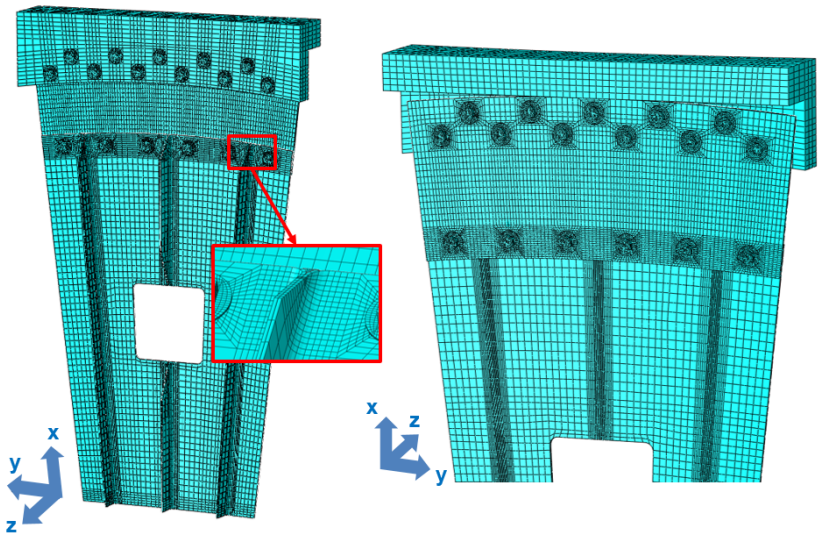

Figure 7.18: Final mesh used for the stiffened panel fracture analyses.

7.3.2. FRACTURE RESPONSE

This subsection presents the final simulation results obtained with the stiffened panel model. The test data presented in subsection 7.1.2 is compared to the final fracture results in order to assess the validity of the panel fracture simulation. The main final errors evaluated between the model and the experiment are summarized in Table 7.3.

FRACTURE INITIATION AND GROWTH RESULTS

First, the damage initiation and evolution outputs CSMAXSCRT and CSDMG (see Table B.1) are exploited in order to visualize the damage zone at the end of the analysis. The CSDMG damage field is presented in Figure H.1. The following conclusions can be drawn on the predicted fracture initiation:

- The high values of CSDMG indicate a full stiffness degradation. Therefore, damage initiates mainly at the outer stringers run-out. This is coherent with the visual observation made on the test panel, which shows two crack at these locations.
- Additionally, damage is present along all the fillers on the panel upper part. Given the limited available test data, the damage state inside the panel cannot be visualized.

The CSMAXSCRT initiation criterion field is shown in Figure H.2. It provides indication of the elements which are susceptible to get damaged soon in the analysis. Therefore, even without having any propagation result, the following propagation results can be foreseen:

Output type	Performance evaluated on	Performance of the fracture analysis
L1/L2 load-displacement	Initial stiffness (% difference)	20% error
	End of the analysis	Corresponds to the beginning of experimental crack propagation
L3/L4 load-displacement	Initial stiffness (% difference)	45% error
Stringers run-out visible cracks	Location of crack (visual evaluation)	+ Damage initiates at left stringer + Damage likely propagates at outer stringers - Significant damage at middle stringer
A5 out-of-plane displacement	Displacement at 44 kN (% difference)	40% error
	Displacement at 60 kN (% difference)	36% error
Strain responses	General features	+ Same strain evolution trends - Persisting slopes discrepancy

Table 7.3: Summary of the performance of the final panel's fracture simulation compared to test data. The sensors references are shown in Figure 7.4.

- The high values of CSMAXSCRT indicate the imminent damage initiation. Therefore, the right and left stringers will start damaging in their center. This will probably promoting delamination at these locations later during the test. This information cannot be verified with the current data.
- The low values of CSMAXSCRT indicate a possible damage initiation later during the analysis. Therefore, damage may start between the skin and the stringer sub-laminates. It would initiate crack propagation at the outer stringers run-outs. This corresponds exactly to the visual inspection described in Figure 7.7.

LVDT RESULTS

The final L2/L3 load-displacement curve is given in Figure 7.19 and is compared to the test data and to the analysis which didn't include fracture. The L3 and L4 curves are given in Figure 7.20. The out-of-plane displacements at L5 and L6 locations are still negligible. Different remarks are listed below. Overall, the simulated load-displacement behavior agrees with the experiment.

- The errors in initial stiffness for both figures remain the same in as subsection 7.2.6, therefore the remarks made about the model low flexibility are still valid.
- The second half of the fracture response however shows a reduced stiffness which is very similar to the experimental result. The effect of damage is visible on the curve from 40 kN to 56 kN, which is the end of the analysis.
- The analysis stops shortly before 60 kN, which is the load at which NLR reported to hear a sudden crack. As it was explained in subsection 7.3.2, the analysis stops converging right before crack propagation. Therefore, the final load-displacement curve obtained for the fracture analysis is coherent with the experimental results.
- The damage starts in the left-hand stringer (with respect to the right view in Figure 7.18), which is the first stringer NLR reported to fail.
- The asymmetry in the experimental L1/L2 and L3/L4 curves appears after 60 kN, which is the first delamination propagation. Since the analysis stops before 60 kN, the fact that no asymmetry is observed in the analysis curves is satisfactory.

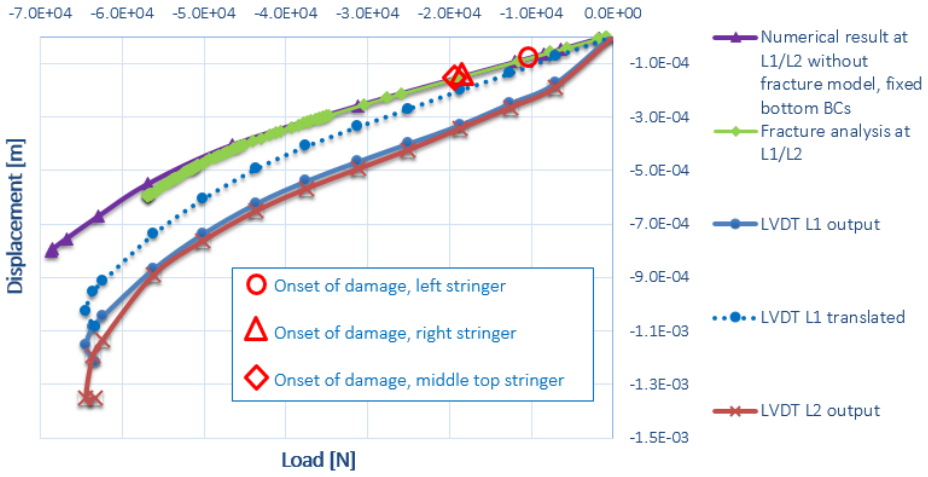

Figure 7.19: Load-displacement curves of the panel elastic and fracture compression analysis together with the experimental outputs of L1 and L2. L1 and L2 simulation outputs are identical.

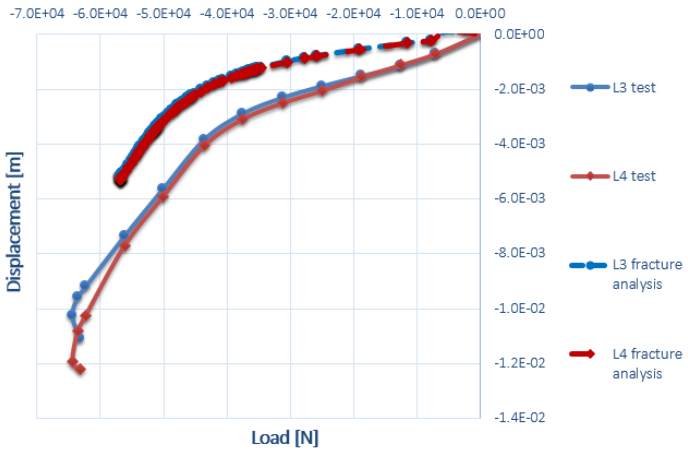

Figure 7.20: Load-displacement curves of the panel elastic and fracture compression analyses together with the experimental outputs L3 and L4.

OUT-OF-PLANE DISPLACEMENT FIELD RESULTS

Two out-of-plane displacement fields are shown in Figure H.3; one at 44 kN and one at the end of the fracture analysis. These fields are compared to the Aramis results of Figure G.2. The test data and analysis results comparison leads to the following observations. First, the global gradients in displacement along the surface are very similar for both 44 and 60 kN. However, the fields asymmetry which is very clear on the test data is less present for the analysis results. Moreover, the amplitude of the out-of-plane displacements is approximately 40% lower for the analysis compared to test. This highlights once more a difference in flexibility.

STRAIN GAUGES RESULTS

The strains evolution are recorded in different points during the analysis and are shown in Figure H.4. These results are plotted together with the strain test results for comparison. The observation is made that almost every analysis strain curve follows the same trend as the corresponding test result. However, the slopes are invariably lower in the case of analysis. This confirms one more time the low flexibility of the model. In addition, the strain signs are different between experiment and analysis for the R2a strain rosette, along the O2 axis (see Figure 7.4). This gauge is placed along the left outer stringer at the location where the most differences in out-of-plane displacements are observed between analysis and experiments.

7.4. CONCLUSION

This chapter focused on the modelization of the failure behavior of a conical stiffened panel. The model used for this process did not include fracture at first, in order to identify the elastic response of the numerical set-up. It was chosen to model all the parts present in the experimental set-up in an attempt to limit the sources of discrepancy and capture accurately the loads. The AFP layup was approximated through different zones of constant ply angle. The panel and top-ring were modeled with C3D20R elements in order to capture bending while ensuring a straightforward implementation of contact interactions. The elastic response of the numerical model shown to be significantly stiffer than the experiment's one. It is suspected that the real panel manufacturing imperfections and the rotation of the test bench are sources of discrepancy. Additionally, the limit in the order of numerical elements and the approximated layup may prevent the model from having the desired flexibility. However, the predicted panel's bending mode was the same as the experimental deformation and the asymmetry in out-of-plane displacement were as well captured by the model. Therefore, even if the developed numerical model is not suited for a quantitative estimation of error, the fracture behavior was still implemented to assess the soundness of the failure model.

The cohesive surfaces were added to the model to predict fracture. The fracture predictions were proven to be very close to the experimental results. Cracks initiated at the stringers' run-outs and are expected to propagate around the outer stringers. This corresponds to what was observed visually on the final test panel. Moreover, damage initiated initially at the left stringer during the analysis, which is coherent with the first crack propagating at the left stringer during testing. Moreover, the analysis stopped converging most likely just before the first crack propagation. The load level at the end of the analysis was the same as reported during the first delamination propagation during testing. The fact that the analysis did not predict damage around the cutout corresponds as well to the experimental results. In other words, independently of the low panel flexibility, the fracture simulations yielded promising results. The limit in convergence stems from the high non-linearity encountered during crack propagation. The surface-based fracture model's propagation predictions could therefore not be assessed.

Recommendations are formulated in the next section to be able to quantify validity of complex fracture simulation in future studies.

7.5. RECOMMENDATIONS FOR LEVEL FIVE

Following the conclusion of this chapter, two main recommendations are formulated for conducting the validation of complex failure analyses. The uncertainty quantification presented in subsection 3.5.1 is as well recommended.

7.5.1. TEST SET-UP

Positioning the LVDTs away from the panel to be tested again made the interpretation of the total displacement cumbersome. In particular, it is difficult to extrapolate the beginning of the response curve, since the global behavior of that structure is not linear. All the displacements should be measured on the panel itself. For example, measuring the vertical displacement in-between the upper middle bolts of the top-ring or the panel would have facilitated the comparison. The load measurement performed in the test bench, on the other hand, does not cause any issue. In the same way, all the strain gauges measurements could be directly compared to the analysis.

In addition, as it was explained in subsection 7.2.3, only one layer of elements can be used throughout the thickness when defining a laminate with the Abaqus composite modeller. The observation was made that the available element types could probably not perform flexibly enough during the compression simulations. In order to improve the correlation between simulation and test, using a test which does not generate a large amount of bending in the structure is preferable. For example, in the present case, since no delamination is observed around the cutout, using the same panel without cutout would probably give the same stringer delamination while creating less bending in the structure. Ensuring the proper fixation of the test fixture during testing would as well ensure that the panel flexibility observed during testing is not enhanced by loose fixtures.

Finally, having a idea of the extent of the final delaminations in the test and in the analysis would permit

to compare further the fracture behavior. In particular, the fracture toughness of the cohesive surfaces could be validated. In the current dataset, only the visual inspection gives an idea of the location and width of delamination. Non-destructive techniques can be used to detect the cracks inside the laminate. Namely C-scanning which uses ultrasounds, X-ray methods and Eddy current techniques are the most common [30]. C-scanning is advised as it is a reliable, automatable, fast and widely used process which gives the damage location and extension. Its principle is based on the propagation of acoustic waves throughout the material, which get transmitted and reflected differently when there is a defect. A precise description of this technique was done by Fahr and Kandeil [31].

7.5.2. NUMERICAL MODEL

The crack growth could be obtained in the numerical model by running an Abaqus/Explicit simulations. Fracture propagation is numerically influenced by the fracture toughness inputs. It would be valuable to evaluate this aspect of the fracture model which could not be validated in the present study. This analysis is meaningful mainly if the C-scan results are available, in order to compare extent of fracture inside the panel.

8

General Conclusions and Recommendations

8.1. Conclusions

Furthering the understanding behind Carbon Fiber Reinforced Plastic (CFRP) technology for space launcher applications is one of the objectives of the European Future Launchers Preparatory Programme 3 (FLPP3). Within the scope of this study, Airbus Defence and Space Netherlands B.V. (ADSNL) is designing a composite version of Ariane 6's Vinci engine Thrust Frame (ViTF) and seeks to ensure its structural integrity. This requires that the predictive capabilities of the developed simulations be heavily scrutinized and assessed. This Master thesis was carried out in order to investigate the Verification and Validation (V&V) of the numerical methodologies which are to be applied in the company for the numerical failure assessment of laminated composites. The conclusions derived from this investigation are valuable to companies willing to realize weight savings through the utilization of composite materials, as well as those who wish to incorporate accurate numerical models into their structural design process. The formulated objective of this study was:

The objective of this Master thesis is to assess the validity of the numerical Hashin intra-ply damage model and surface-based cohesive inter-ply fracture model. This is achieved by performing a calibration and validation procedure, which compares finite element-based failure simulations to experimental test data, as part of a Building Block Validation approach.

The study focused on one damage and one fracture models readily available in Abaqus. The explored method to verify and validate numerical models is a gradual approach divided into levels of model calibration and validation. Referred to as: "certification by analysis supported by test evidence" or Building Block Validation (BBV) approach, it optimizes the need for experimental testing and modeling. In chapter 2, a validation procedure based on that concept was built in five levels, which enabled the validation of the Hashin damage model and the surface-based cohesive fracture model. The test data being fully provided by Netherlands Aerospace Centre (NLR), the proposed approach was organized in terms of the available experimental results. The activities included in the scope of the study were the verification and implementation of the computational models, acquisition of the simulation results and the qualitative comparison to experimental results.

The results and outcomes of this work partially answered the research objectives initially defined. Specific conclusions were drawn concerning the validity and limitations of the results at the end of chapters 3 through 7, in order to maintain fluidity throughout the bottom-up validation procedure. A general summary is presented in the next paragraphs.

The BBV procedure started with the calibration of the Hashin damage model described in chapter 3. This model was used to predict CFRP intra-ply damage. The three tests used to perform the calibration were a mixed layup 0^o and 90^o compression test (test 1 and 2) as well as an in-plane-shear test (test 3). The optimization started with the elastic input parameters, which influence the linear response of the models. The

strength input parameters were subsequently optimized which influence the nonlinear response and total strength. In both cases, a sensitivity study of the different inputs was performed in order to determine the most straightforward optimization approach. The sets of final inputs were provided in expressions (3.1) and (3.2). The final stiffness errors were negligible, while acceptable final strength errors were obtained for test 3. An important stiffness difference was however pointed out in the test 2 result, which probably stemed from the built-in formulation of the Matrix Compression (MC) damage parameter. The fracture toughness parameters could not be calibrated with the current procedure because they do not influence the numerical responses, which are brittle.

The performances of the elastic behavior and the damage model were assessed in chapter 4. This level compared the final response of an Open-Hole Compression (OHC) test with the corresponding simulation results. It was noticed that the OHC model was extremely mesh sensitive. After conducting a mesh-convergence study on the strain concentration factor K, a mesh which is biased and refined around the hole was adopted. The inputs determined in chapter 3 were used for the validation simulation and both the errors in stiffness and strength were low. However, the current OHC specimen displayed inter-ply fracture which was not taken into consideration. It was necessary to include the modelization of delamination in level 4 in order to draw final conclusions concerning the validity of the Hashin model.

The next stage of the BBV approach concerned the calibration of the inter-ply fracture model using a three-point bending test described in chapter 5. The numerical model was built with each layer in contact through a surface-based cohesive behavior, and the boundary conditions constituted of solid cylinders in contact with the specimen. After ensuring mesh convergence, the cohesive input parameters were calibrated. The position of the displacement sensor during the test were not suitable to perform a comparison with simulation, therefore the calibration procedure focused solely on the maximum strength. This enabled the calibration of the single strength parameter X_c, given in expression (5.2) and yielding a negligible error. Consequently, three of the fracture model's input parameters could not be optimized.

Due to lack of test data, the validation of the inter-ply fracture model in chapter 6 had to be performed with the same OHC test as in level 2. This configuration was not ideal since both the Hashin damage model and the cohesive surfaces had to be used. All the plies of the level 4 numerical model were modeled separately in order to use cohesive surfaces between each one. A convergence issue was encountered when verifying that the level 4 model with tied plied and intra-ply damage gives the same results as that of level 2. The stability issue arose due to the sudden stiffness drop met during fiber damage in the single plies. This problem could not be overcome in Abaqus/Standard and it was decided to halt the validation procedure, due to the time restrictions and the fundamental unsuitability of the OHC test. The performance of the calibrated fracture model was therefore not assessed.

Nevertheless, the performance of the inter-ply fracture models could be studied in chapter 7 for the next level of the BBV pyramid. This last step focused on inter-ply fracture simulations for a curved stiffened panel. This assembly represents a scaled section of a fiber-placed ViTF design, attached to an aluminum top-ring. All the parts present in the test set-up were modeled individually and the mesh convergence as well as the choice of elements was carefully studied. The resulting model behaved stiffer than the test panel. A qualitative comparison to the experimental results could nevertheless be conducted. The simulation converged up until fracture propagation. It provided satisfactory predictions of the damage initiation and the load at which the first delamination propagates during testing. The probable fracture propagation regions, represented by zones where the initiation criterion reaches significant values, corresponded to regions around the stringers run-out where cracks were experimentally observed. Despite a low panel flexibility, the simulation yielded promising results in terms of fracture predictions.

8.2. FUTURE WORK

The thesis objective was to fully validate the two failure numerical models. This was not entirely achieved due to the limitations of the available test data, however the models' calibration was performed. The key aspects of the BBV activities were identified and highlighted, which constitutes the groundwork to develop an efficient validation procedure. The areas which require further research in order to make accurate and time-efficient validation procedures for failure of CFRP structures are summarized herein. Given the specificity

of some of the recommendations, specific suggestions were already formulated in chapters 3 through 7. A summary of the key suggestions the author is described below.

First, the sets of tests which could permit to follow the entire intended validation approach are the following:

- Calibration of both the full material elastic behavior and the Hashin damage model can be performed in a straightforward manner with the response curves of: a 0° tension test, a 0° compression test, a 90° tension tests and a 90° compression test, all layups being preferably unidirectional. An In-Plane Shear (IPS) test similar to the one already available can be used in addition. Concerning the fracture toughness inputs, direct measurement tests are uncommon. A way to estimate these parameters may be to measure the stiffness reduction during a cycling tests and use the Abaqus damage propagation theory to deduce the corresponding inputs.

- Validation of the material elastic behavior and Hashin damage model may be more efficiently performed using compression testing of coupons having mixed layups. Tension tests can be included if the tensile input parameters have to be validated. Any variety of stacking sequences and number of plies could be used for this level. It is of primary importance that the specimens show very little or no delamination before final failure.

- Calibration of the cohesive surface-based fracture model is expected to be possible with two tests involving only mode 1 delamination, and two tests involving mode 2 delamination. The latter could simply be two tests similar to test 4 used in this study, differing in stacking sequence. For the mode 1 delamination tests, it is recommended to try using double cantilever beam tests.

- Validation of the same fracture model should be achieved with the same type of test, as long as both mode 1 and mode 2 delamination are present. The difference from the calibration tests lies in the complexity of the sample: bigger stacking sequences together with different layer orientations are expected to be sufficient.

- Validation of the complex stiffened panel test would be improved if the test fixtures were prevented from bending. Additionally, for a first sub-part validation step, it is advised to use a test panel which would bend less and be easier to model, for example without a cut-out.

The test set-up and the sensor positions were shown to be of primary importance in order to perform the comparison to simulation, especially in chapters 5 and 7. The comparison is made difficult if the displacement and strain sensors are placed on the tests bench or on the tabs, since spurious deformations are taken into account. It is preferable to measure these quantities on the specimen itself, or as close as possible, to estimate the measurement uncertainties.

A video recording of the tests would largely improve the interpretation of the test data as well. In particular, visually detecting the initiation of delamination during coupon testing indicates the extent to which the test results can be used for an intra-ply model calibration. In the case of the panel test of chapter 7, an additional C-scan of the composite parts would enable the comparison of crack extent, which is indispensable in the current validation procedure.

Concerning the tests modelization, it is suggested to carefully study the expected failure modes before choosing the integration scheme of a coupon model. This would ensure significant time saving. Convergence difficulties arise when the stiffness reduction following the damage initiation is too important. For example, as encountered in chapter 6, if the plies damage individually and no stabilizing averaging effect is present, convergence may not be obtained with Abaqus/Standard, which incites the use of Abaqus/Explicit. In addition, the simulation of complex components such as the panel of chapter 7 would require the use of Abaqus/Explicit in order to obtain crack propagation results. In the case of the stiffened panel, the severity of damage created convergence difficulties.

One major key aspect of validation which was defined as being beyond the scope of this study concerns the evaluation of uncertainties. As detailed in subsection 3.5.1, final error evaluation is not meaningful without this evaluation. The Guide for Verification and Validation in Computational Solid Mechanics [2] advises

to estimate uncertainty in both the models and test results. Methods for evaluating the model's aleatory uncertainty could for example include Monte-Carlo simulations [20] or simulation reliability estimation [21]. A simple mean value and standard distribution should at least be provided for the experimental results by performing redundant measurements.

Apart from improvements concerning the validation of the current failure models, a suggestion for future research is proposed. The large variety of damage initiation criteria available either directly in Abaqus or as UMATs make it difficult to estimate the best choice for a given scope of validation application. Therefore, assessing the performances of several intra-ply damage criteria on usual laminate coupons and parts could lead to the construction of a comparative catalog. From the latter, engineers could choose the most suitable criterion for their objective, given their resources. This would also help them define the appropriate coupon testing campaign corresponding to the chosen failure criterion.

Appendices

A

Material Input Data

Description	Notation	Initial value	Source
Damage model initial inputs			
Longitudinal tensile modulus	E_{11}^0	157200 MPa	Manufacturer's datasheet
Transverse tensile modulus	E_{22}^0	9377 MPa	
Shear moduli	$G_{12}^0 = G_{13}^0 = G_{23}^0$	5516 MPa	
Poisson ratio	ν_{12}	0.3	
Longitudinal tensile strength	X_t^0	2505 MPa	
Longitudinal compression strength	X_c^0	2078 MPa	
Tranverse tensile strength	Y_t^0	76 MPa	
Longitudinal shear strength	S_L^0	56 MPa	
Transverse compressive strength	Y_c^0	76 MPa	No data, so $Y_c^0 = Y_t^0$
Transverse shear strength	S_T^0	38 MPa	The Hashin model imposes $S_T = Y_c/2$
Longitudinal tensile fracture toughness	$GT1^0$	91.60 N/mm	Shi, Swaut and Soutis [32]
Longitudinal compressive fracture toughness	$GC1^0$	79.90 N/mm	
Transverse tensile fracture toughness	$GT2^0$	0.22 N/mm	
Transverse compressive fracture toughness	$GC2^0$	1.10 N/mm	
Additional fracture model initial inputs			
Tensile contact strength	X_{2t}^0	76 MPa	$X_{2t}^0 = Y_t$ after calibration of level 1
Shear contact strength	X_6^0	80 MPa	$X_6^0 = S_L$ after calibration of level 1
Transverse tensile fracture toughness	$GT2^0$	0.22 N/mm	Shi, Swaut and Soutis [32]
Shear fracture toughness	$G6^0$	0.79 N/mm	Lopes [6]

Table A.1: Initial input parameters and their origin.

B

Damage and Contact Output Parameters

Output name	Description	Comments
HSNFTCRT	Maximum value of the Hashin fiber tensile initiation criterion	Value 0: the criterion has not been satisfied Value 1: the criterion has been satisfied
HSNFCCRT	Maximum value of the Hashin fiber compressive initiation criterion	
HSNMTCRT	Maximum value of the Hashin matrix tensile initiation criterion	
HSNMCCRT	Maximum value of the Hashin matrix compressive initiation criterion	
DAMAGEFT	Fiber tensile damage variable	Value 0: element undamaged Value 1: element totally damaged (for the damage mode)
DAMAGEFC	Fiber compressive damage variable	
DAMAGEMT	Matrix tensile damage variable	
DAMAGEMC	Matrix compressive damage variable	
STATUS	Status of the element	Value 0: element inactive Value 1: element still active
CSMAXSCRT	Cohesive surfaces maximum contact stress damage initiation criterion	Value 0: the criterion has not been satisfied Value 1: the criterion has been satisfied
CSDMG	Cohesive surfaces overall value of the scalar damage variable	Value 0: cohesive behavior undamaged at the node Value 1: cohesive behavior fully damaged at the node
ALLIE	Internal energy of the model	-
ALLCD	Energy dissipated by viscoelasticity in the model	Make sure that ALLCD <5 % ALLIE
ALLAE	Artificial strain energy in the model	Make sure that ALLAE <5 % ALLIE
ALLSD	Energy dissipated by viscous damping in the model	Make sure that ALLSD <5 % ALLIE

Table B.1: Damage and contact output parameters names and descriptions.

C

Level 1: Input Strengths Sensitivity Analysis

This appendix provides with the sensitivity analysis of the tests 1, 2 and 3 models to the input strengths of the Hashin model. Such a study enables to identify the dependence of each model to the strength inputs and decide in consequence of the best calibration strategy. The damage initiation criterion are monitored for the four different damage modes with the outputs HSNFTCRT, HSNFCCRT, HSNMTCRT and HSNMCCRT (see Table B.1). As soon as one of them reaches one, damage starts in the corresponding mode.

In the case of the test 1 model, MC and Fiber Compression (FC) are the two occurring damage modes. A representation of the damage initiation outputs evolution during the simulation for the initial model is shown in Figure C.1. Final failure is reached as soon as FC damage initiates. This corresponds to the numerical response in Figure 3.13. The four strength parameters are considered to have an influence on the simulation if modifying their value leads to a variation of HSNFCCRT or HSNMCCRT. After doing a sensitivity analysis study, Table C.1 sums up the influence of each strength parameter on damage initiation.

In the case of the test 2 model, MC and FC are as well the two occurring damage modes. Final failure is reached as soon as FC damage initiates. The outputs are plotted in Figure C.2 before optimization of the damage model inputs. This corresponds to the numerical response in Figure 3.14. Table C.2 sums up the influence of each strength parameter on damage initiation. It is remarkable that the MC damage initiation occurs for comparable displacement values in the two types of plies, while the FC damage initiation occurs afterwards.

For the test 3 model, the evolution of the criterion parameter is shown in Figure C.3. This corresponds to the numerical response in Figure 3.15. The only strength parameter having an influence on the damage initiation is S_L.

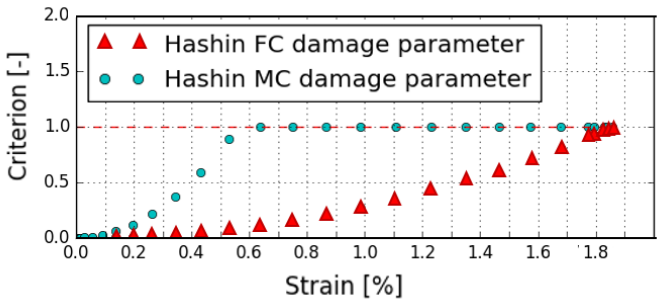

Figure C.1: Damage initiation outputs of test 1, before optimization of the damage input parameters.

Parameter \ Critical failure mode	MC in ±45° plies	FC in 0° plies
Y_c, S_T	0	0
S_L	+	0
Y_t	0	0
X_c	0	+
X_t	0	0

Table C.1: Sensitivity of the test 1 model to the input strengths, as a result of a 20% increase in the strengths parameters. 0: no visible influence, +: relative change in strain at damage initiation above 10%.

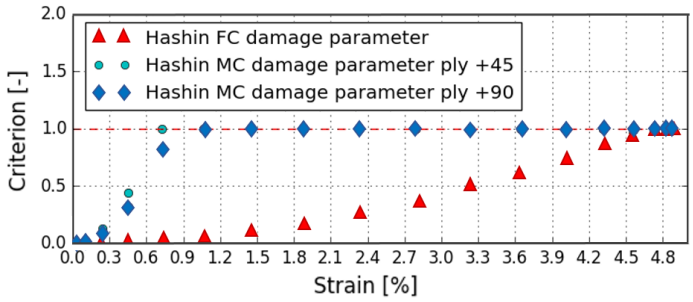

Figure C.2: Damage initiation outputs of test 2, before optimization of the damage input parameters.

Parameter \ Critical failure mode	MC in ±45° plies	MC in 0° plies	FC in ±45° plies
Y_c, S_T	-	+	0
S_L	+	0	0
Y_t	0	0	0
X_c	0	0	+
X_t	0	0	0

Table C.2: Sensitivity of the test 2 model to the input strengths, as a result of a 20% increase in the strengths parameters. 0: no visible influence, -: relative change in strain at damage initiation below 10%, +: relative change in strain at damage initiation above 10%.

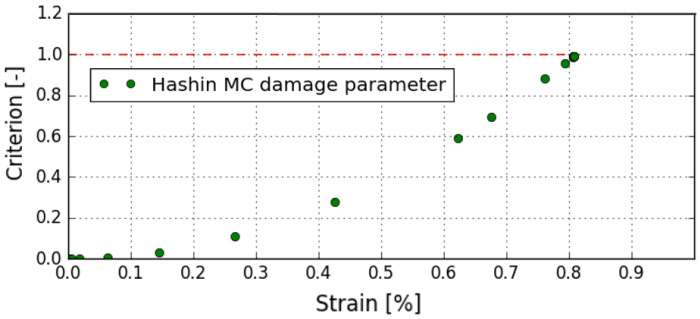

Figure C.3: Damage initiation outputs of test 3, before optimization of the damage input parameters.

D

Level 1: Alternative Calibration Approach

This appendix proposes an alternative approach which was attempted for the strength inputs calibration procedure presented in subsection 3.3.2. The set 1 of linear elastic is used throughout this approach. The final results obtained for the alternative procedure yield less satisfactory final strength errors and drifting of the optimized inputs from the manufacturer's data. The calibration approach is presented in section D.1 and the results obtained for the validation procedure of chapter 4 is presented in section D.2.

D.1. Alternative Calibration Approach

This approach consists in performing the curve fit in a different order than what was done in subsection 3.3.2. The test 2 curve fit is performed before test 1 and test 3 optimization. Figure 3.14 is therefore calibrated first. Following the remarks of the sensitivity study and Table 3.3, X_c is lowered in order to obtain the right failure strain. It corresponds to $X_{c,calib} = X_c^0 - 65\% X_c^0 = 727$ MPa. The slope of curve during the damage process is very low, as seen in Figure 3.14. Therefore, after calibrating X_t, the predicted strength is still significantly below the experimental value. The only way to improve this aspect is to increase the value of S_L and S_T and therefore delay the onset of damage. It is initially chosen not to go beyond an increase of 100% in these values, in order to not deviate too much from the manufacturer's data. With an increase of 90% in S_L and S_T, the following calibrated response for test 2 is shown in Figure D.1.

As summarized in Table 3.3, fixing the values of S_L, S_T and X_c already determines all parameters influencing the test 1 and test 3 simulations. The set of optimized values called alternative set is given below.

$$X_{c,calib} = 0.35 X_c^0 = 727 \text{ MPa} \tag{D.1a}$$

$$S_{L,calib} = 1.90 S_L^0 = 106 \text{ MPa} \tag{D.1b}$$

$$S_{T,calib} = 1.90 S_T^0 = 72 \text{ MPa} \tag{D.1c}$$

$$Y_{c,calib} = 2 * S_{T,calib} = 144 \text{ MPa} \tag{D.1d}$$

The results for test 2 and 3 simulations with the determined parameters are shown in Figure D.2 and Figure D.3. The final strengths errors are 28% for test 1, 9% for test 2 and 110% for test 3.

The strength results for the IPS test and test 1 simulations is less satisfactory than with set 2 (see expression (3.2)). This is explained by the fact that X_c is lowered significantly and S_L is increased almost by a factor two; the onset of damage in FC mode occurs before the onset of damage in the matrix. Hereby final failure does not happen immediately after fiber damage and some extra load is carried up until the matrix starts damaging. The loss in stiffness after the start of fiber damage is very important and does not seem to correspond to what happens during the experimental test.

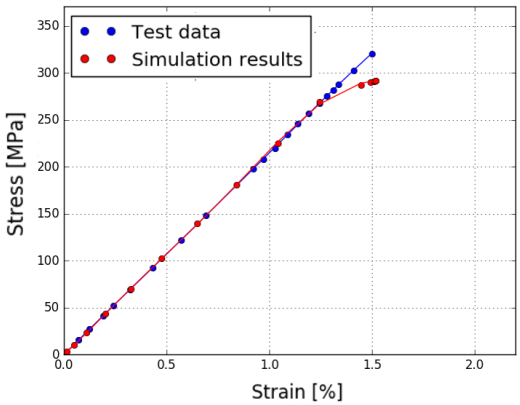

Figure D.1: Response of the test 2 model with the calibrated elastic parameters and, in the second calibration approach, $X_{c,calib}$ = 727 MPa, $S_{L,calib}$ = 106 MPa, $S_{T,calib}$ = 72 MPa.

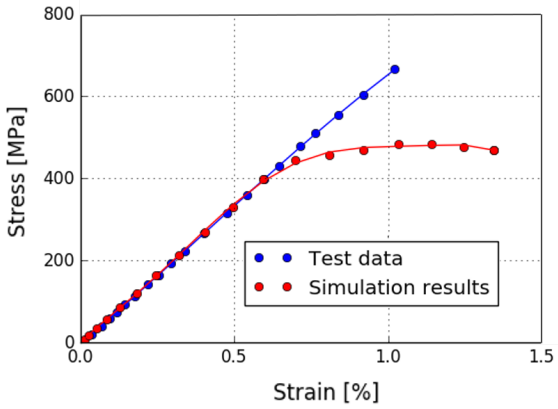

Figure D.2: Response of the test 1 model with the calibrated elastic parameters and, in the second calibration approach, $X_{c,calib}$ = 727 MPa, $S_{L,calib}$ = 106 MPa, $S_{T,calib}$ = 72 MPa.

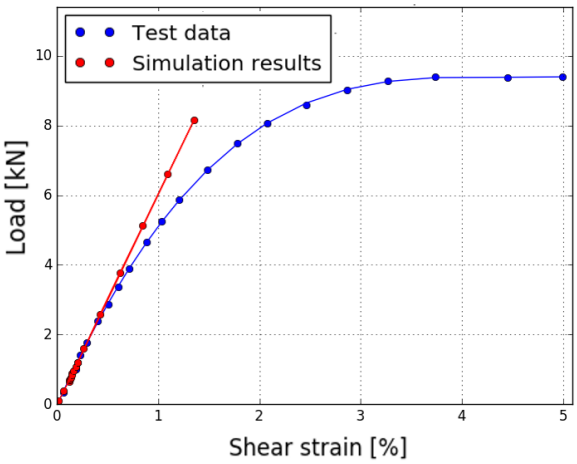

Figure D.3: Response of the test 3 model with the calibrated elastic parameters and, in the second calibration approach, $X_{c,calib}$ = 727 MPa, $S_{L,calib}$ = 106 MPa, $S_{T,calib}$ = 72 MPa.

D.2. VALIDATION OF THE ALTERNATIVE INPUT SET

Using the validation procedure of chapter 4, the result of the OHC simulation for the alternative set is plotted in Figure D.4. The error is 7% in stiffness and 25% in strength. The error in strength is not acceptable, especially because it already predicts a very low strength. This prediction can only become even lower when adding delamination to the model. Therefore, the preference of set 2 over the current alternative set of inputs is confirmed.

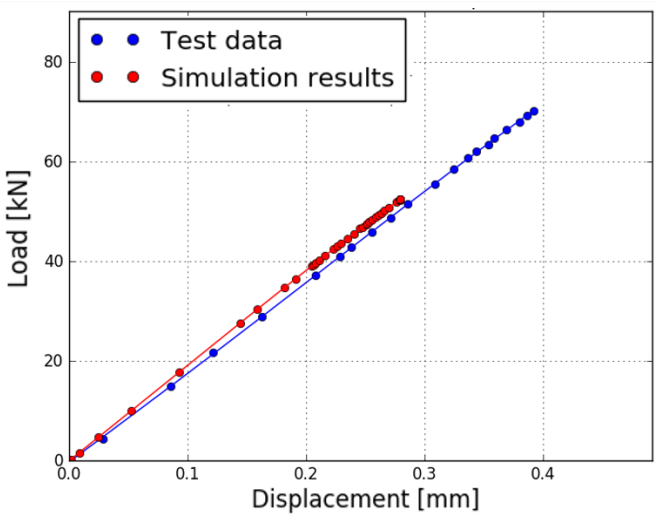

Figure D.4: Results of the OHC simulation in level 2, using the alternative set of parameters.

E

OHC Model: Damage Input Parameters Sensitivity Analysis

This appendix provides a set of comments concerning the sensitivity of the OHC test for the level 2 of the BBV approach. It was explained in 'Parameters Calibration' of subsection 3.3.2 that the value of S_L and S_T were not clearly calibrated. There remains a degree of freedom for these two parameters which could be exploited for calibration refinement if the results obtained with the damage model are insufficient in the next levels of validation.

An inspection of the damage parameters for the OHC simulation of Figure 4.8 reveals that only the FC damage mode is activated. The initiation criteria for Matrix Tension (MT) and MC in the 0° and 45° layers reach the value 0.9. As it was proven in subsection 3.3.2, FC damage initiation depends on X_c, while the matrix damage modes depend on S_L.

MT and MC damage can therefore accelerate the failure if a modification in S_L makes the initiation parameters reach the value 1 before final failure. Using the set 1 parameters with an increase in S_L of 50% instead of 20%, Figure E.1 is obtained. An increase in S_L therefore anticipates the final failure. The final strength in Figure E.1 equals the one of the experimental result.

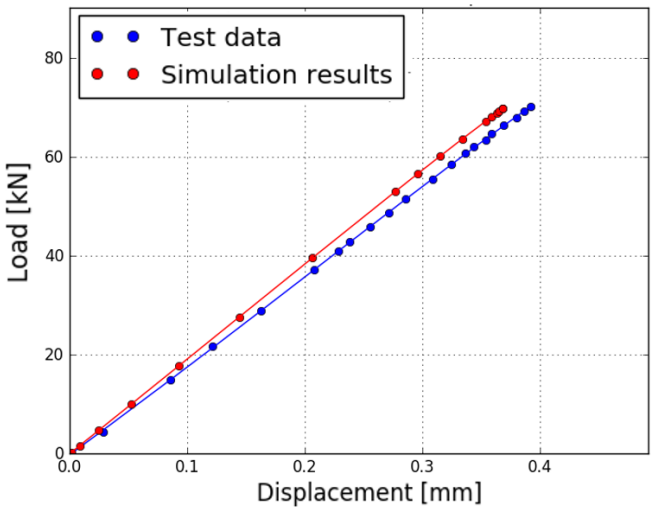

Figure E.1: Results of the OHC simulation in level 2, using set 1 of parameters and $S_L = S_L^0 + 50\% S_L^0 = 28$ MPa.

As it was already mentioned, it is desired to keep a predicted strength above the experimental value for the OHC model including only intra-ply damage. It means that $S_L = S_L^0 + 50\% S_L^0$ is the upper limit for S_L. This information can be used later in level 4 validation in the case where adding delamination in the model would result in too low failure loads: the value of S_L can be lowered in order to increase the total strength.

On the other hand, the choice of S_T does not influence the OHC simulation result. It was defined during calibration that this quantity, which influences the results of test 2 simulations, still had to be optimized. Increasing the value of S_T has a beneficial impact on the test 2 simulation results. In this case, the choice of S_T value is made considering what would be a physically acceptable value. This quantity is not decoupled from the longitudinal strength S_L, even if there does not exist a simple analytical relationship between both. Since the calibration process in itself contains several sources of inaccuracy, the estimation of S_T is kept simple by maintaining the ratio that existed between S_L and S_T in the initial values of Table A.1. Therefore, since S_L is increased of 20%, S_T is chosen to be increased by 20% of its initial value as well.

Extra simulations with the OHC model prove that increasing X_c sensitively increases the maximum load as well. This remark was made likewise for test 1 and test 2 simulations.

F

INTER-LAMINAR SHEAR MODEL: BOUNDARY CONDITIONS

In this appendix, three possible sets of boundary conditions are defined for the Inter-Laminar Shear (ILS) test. The experimental test set-up which is modeled is represented in Figure 5.1. All the boundary conditions are summarized in Table F.1.

Set of Boundary Conditions	Region	Motion
Equivalent boundary conditions Figure F.1	Edge A	U_z applied (<0)
	Edges B and C	$U_x = U_z = 0$
	Point D	$U_y = 0$
Analytical rigid cylinders Figure F.2	Top cylinder	U_z applied (<0)
	Bottom cylinders	Fixed
	Points A and B	$U_y = 0$
	Edge C	$U_x = 0$
Solid elements cylinders Figure F.3	Top cylinder	Uz applied (<0)
	Points A and B	$U_y = 0$
	Edge C	$U_x = 0$
	Surfaces D	Fixed

Table F.1: Summary of the three sets of boundary conditions and displacements applicable to the ILS model.

A first set models each roller contact by an equivalent line constraint.
In that case, the final load-displacement curves are obtained by looking at the total vertical reaction force on edge A and the vertical displacement of one of edge A nodes.

The numerical model with its equivalent boundary conditions are shown in Figure F.1.

Another set of more realistic boundary conditions is created, using analytical rigid surfaces. The analytical rigid surface is an attractive choice for several reasons. First, it does not require to be meshed, therefore saving computational effort. Further saving is realized thanks to the two-dimensional description of the surface and the reduction in tracking effort during contact enforcement. The type of interaction between the analytical rigid cylinders and the layup includes a normal and a tangential component, with a hard pressure-overclosure relationship and a default enforcement method. The tangential component is defined by friction. The friction coefficient being unknown, a default value of 0.15 is used. Additionally, it is decided to adopt a finite-sliding formulation, since it is doubtful that the composite laminate has small sliding with respect to the fixed rollers. The surface-to-surface interaction is selected.
In that case, the final load-displacement curves are obtained by looking at the total vertical reaction force and the vertical displacement of the top cylinder.

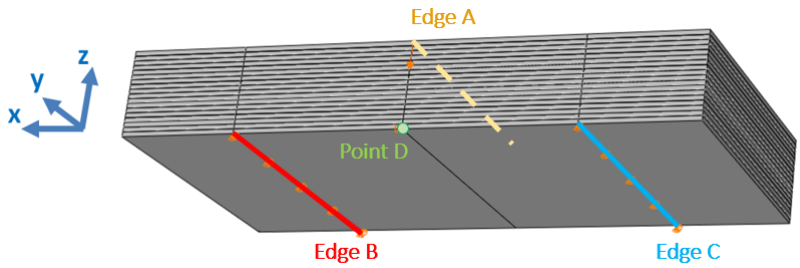

Figure F.1: Numerical model and boundary conditions of the ILS test using equivalent boundary conditions.

The model and its boundary conditions are represented in Figure F.2.

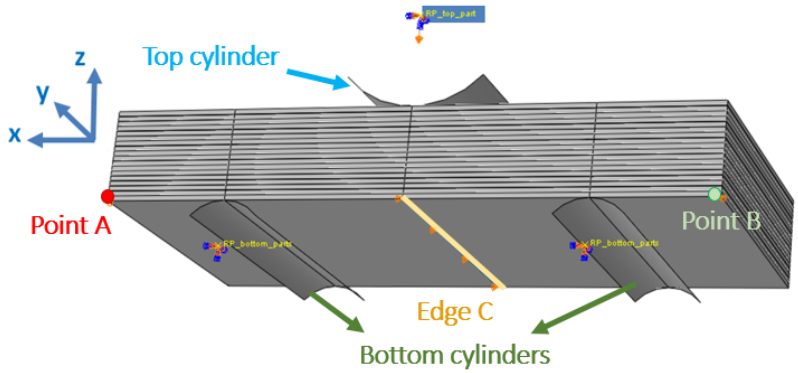

Figure F.2: Numerical model and boundary conditions of the ILS test using the rigid analytical surfaces.

In the last set of boundary conditions, the cylinders are modeled with solid elements. The material is a steel with a modulus of 210 GPa and a Poisson ratio of 0.3. A mesh refinement equivalent to the one which is to be applied to the laminate in contact is chosen. Otherwise, the interaction with the laminate, the friction coefficient, the finite-sliding formulation and surface-to-surface interaction with the laminate all are the same compared to the analytical rigid body boundary conditions presented above.
In that case, the final load-displacement curves are obtained by looking at the total vertical reaction force and the vertical displacement at the top cylinder reference point.

The model and its boundary conditions are represented in Figure F.3. The boundary conditions are similar to the ones used for the rigid analytical boundary conditions.

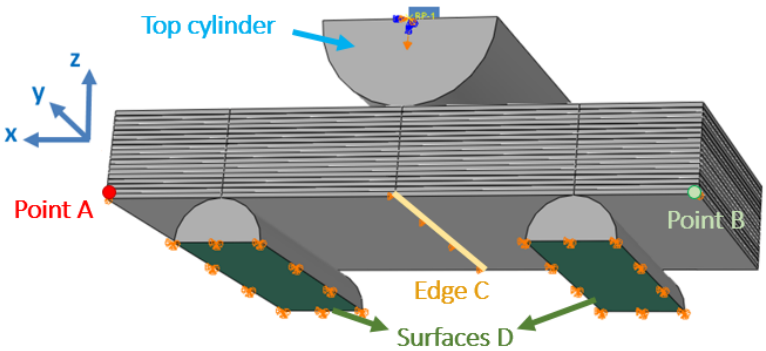

Figure F.3: Numerical model and boundary conditions of the ILS test using the solid elements cylinders.

G

Stiffened Panel: Additional Tests Results

In addition to the Linear Variable Differential Transformer (LVDT) response curves and the visual inspection described in subsection 7.1.2, Aramis and strain gauges results are presented in this appendix.

The single and rosette strain gauges are installed by pairs, with one gauge on the stiffeners side (coded by the letter a) and one on the opposite side (coded by the letter b). Their position is presented in Figure 7.4. The responses are plotted in Figure G.1. The rosettes are aligned with the stringers orientation and measure strains in three directions: the stringer direction (noted direction O2), and two directions oriented at 45° with respect to the stringer direction (noted direction O1 for 45° and direction O3 for -45° in Figure G.1).

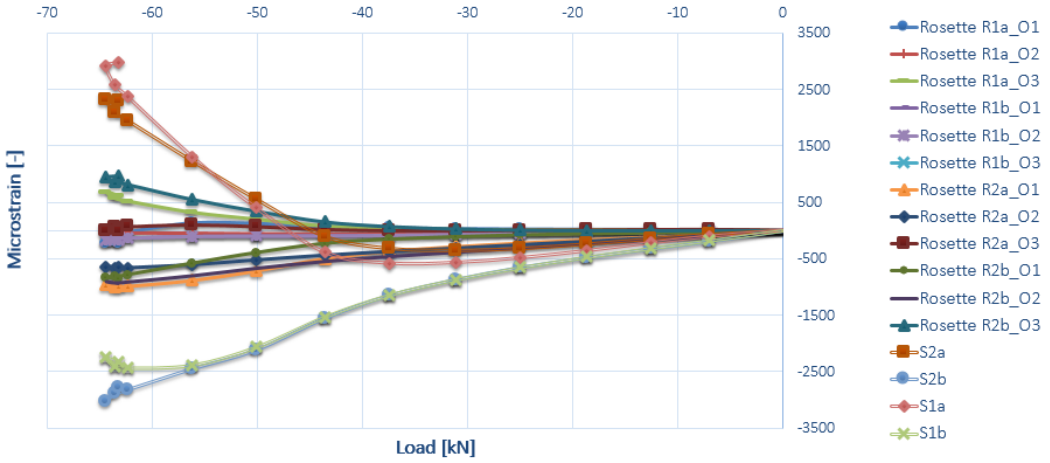

Figure G.1: Strain-load curves of the panel compression test, for single strain gauges and strain gauges rosettes (for strain gauge position see Figure 7.4).

The Aramis measurement is done to assess bending, which introduced in the panel via the aluminium tab. The result fields are shown in Figure G.2 for five different instants of the failure test: at reaction loads of 43.6, 60.2, 64, 62.8 and 59.4 kN successively. The displacement is recorded on the spotted surface shown in Figure 7.3.

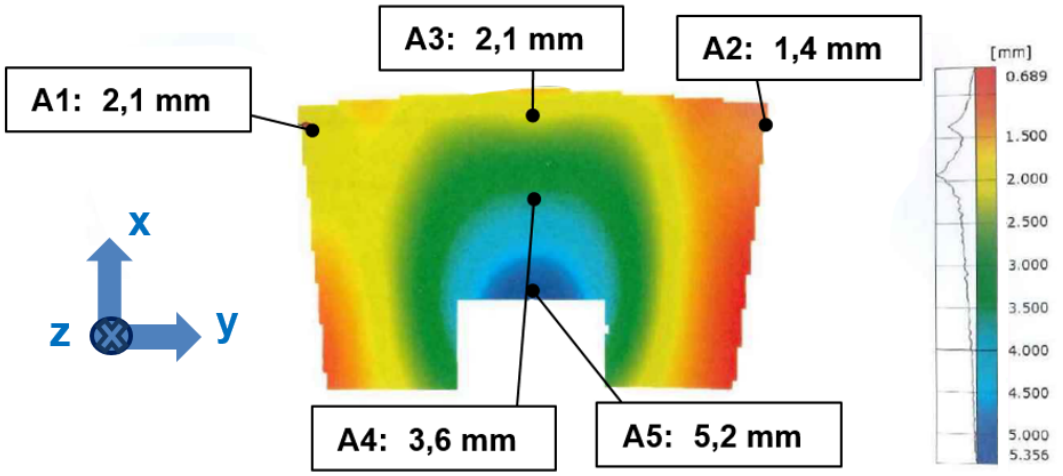

(a) Reaction force 43.6 kN

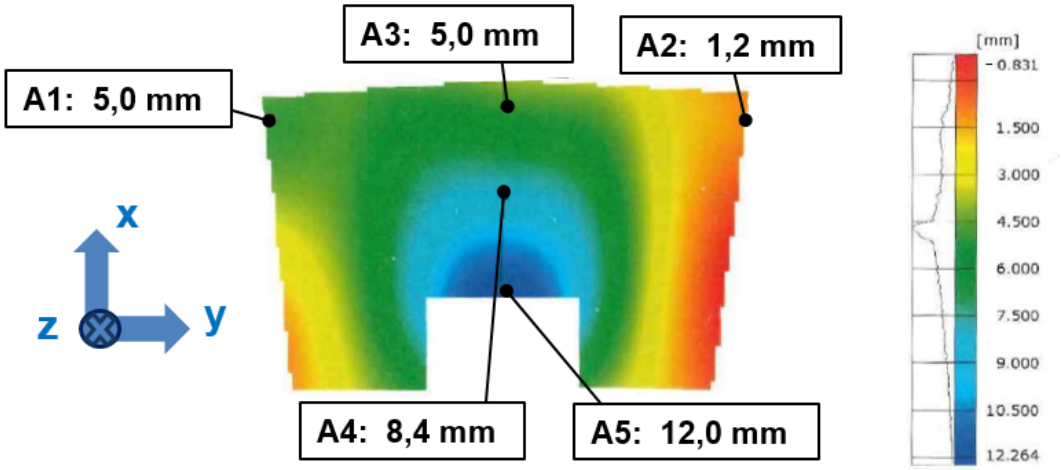

(b) Reaction force 60.2 kN

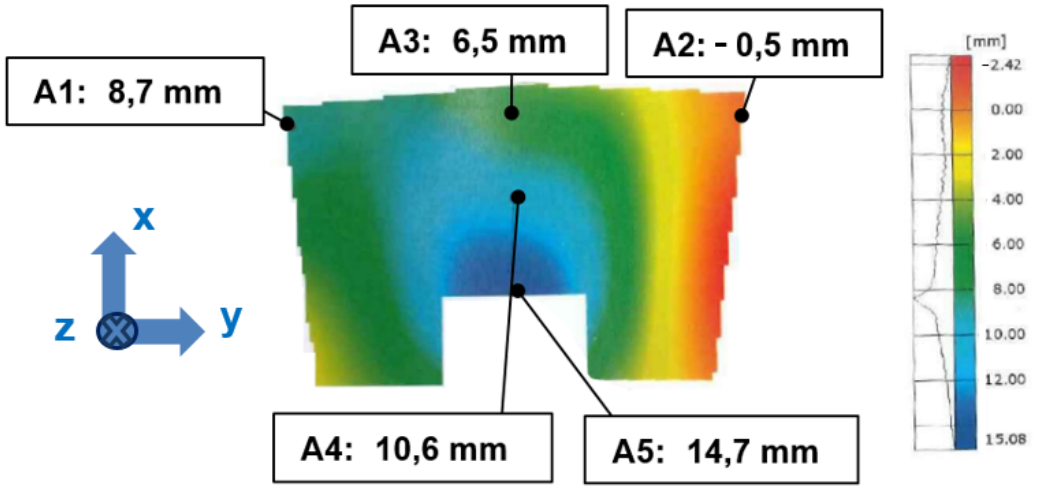

(c) Reaction force 64 kN: delamination of left stringer

Figure G.2: Aramis results for the panel compression test, for different reaction forces measured at the load cell. All the pictures are taken before global softening behavior.

H

Stiffened Panel: Fracture Analysis Results

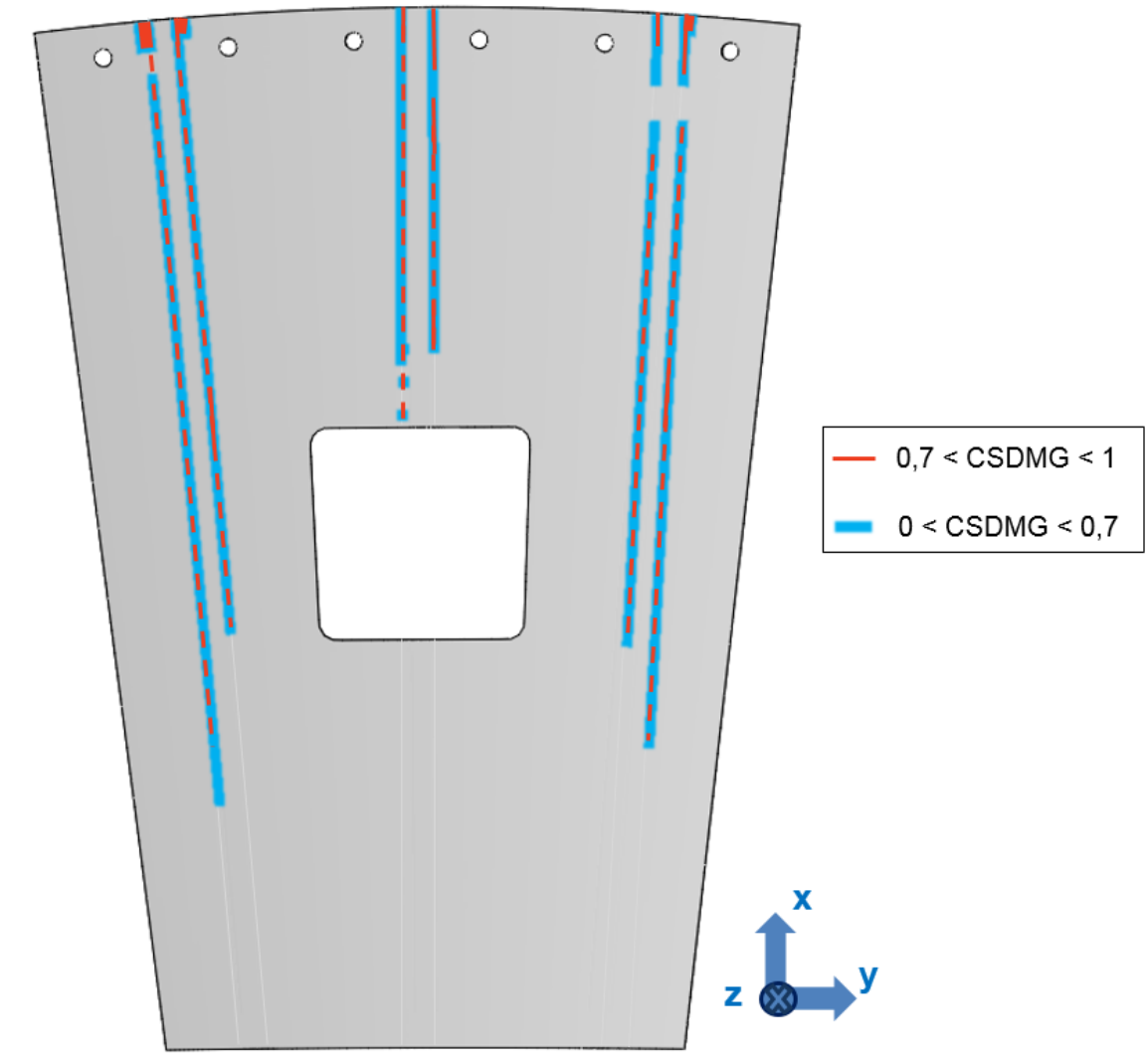

Figure H.1: Stiffened panel CSDMG field result at the end of the panel's fracture analysis. See table B.1 for the definition of CSDMG.

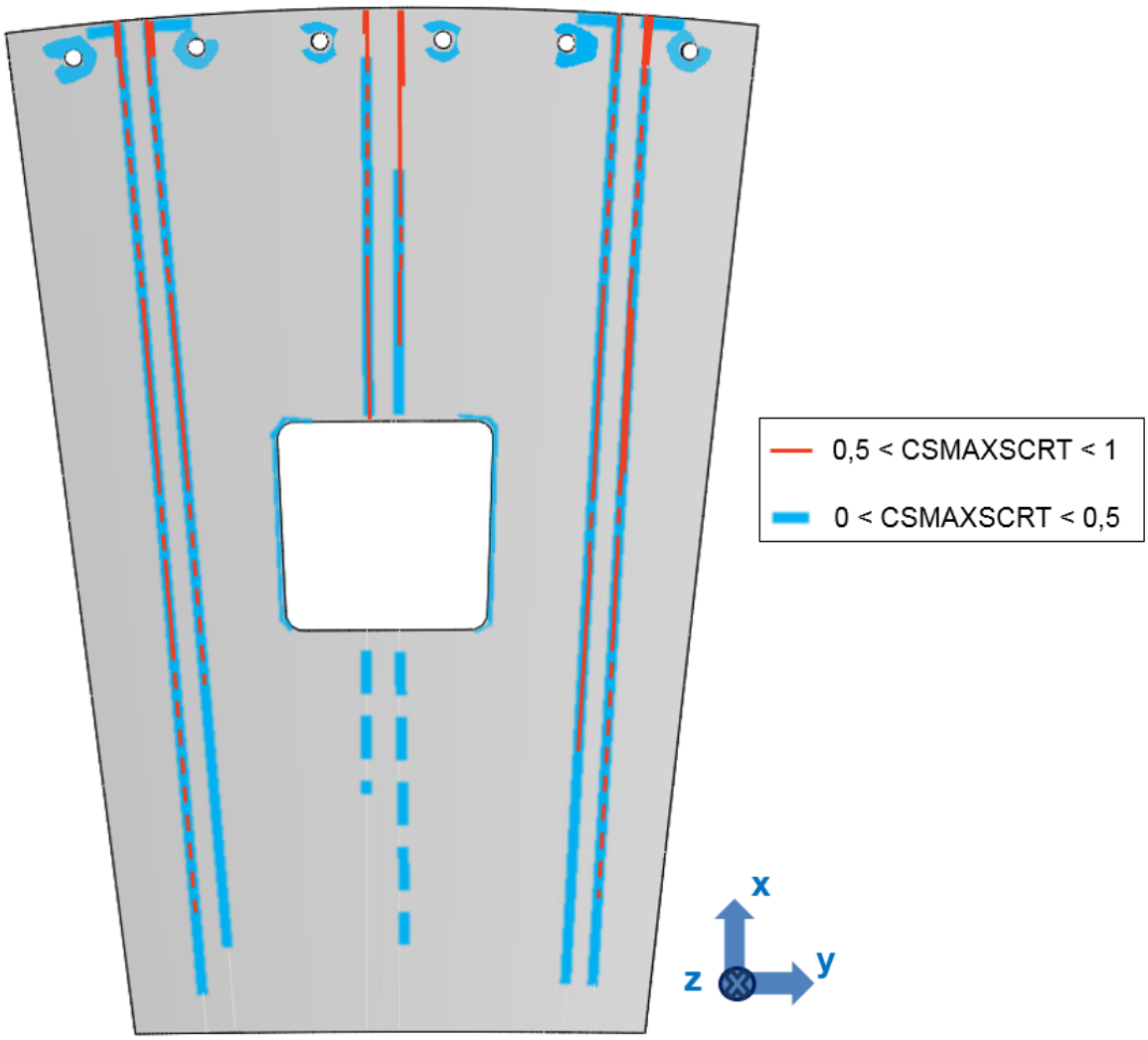

Figure H.2: CSMAXSCRT field result at the end of the panel's fracture analysis. See table B.1 for the definition of CSMAXSCRT.

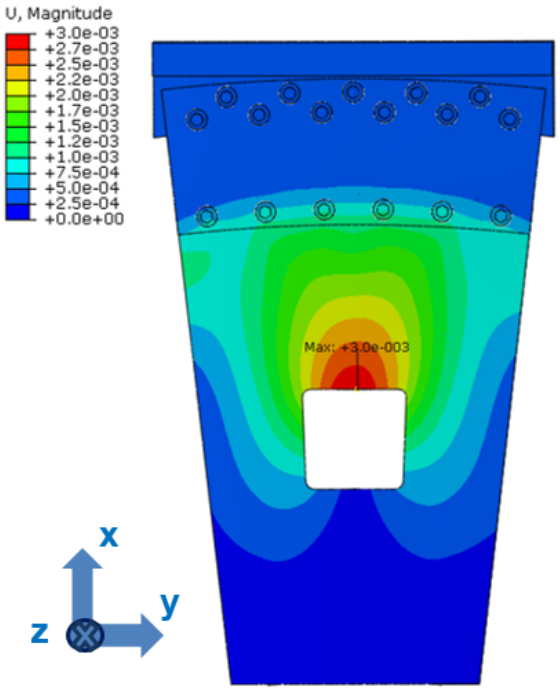

(a) Reaction force 44 kN .

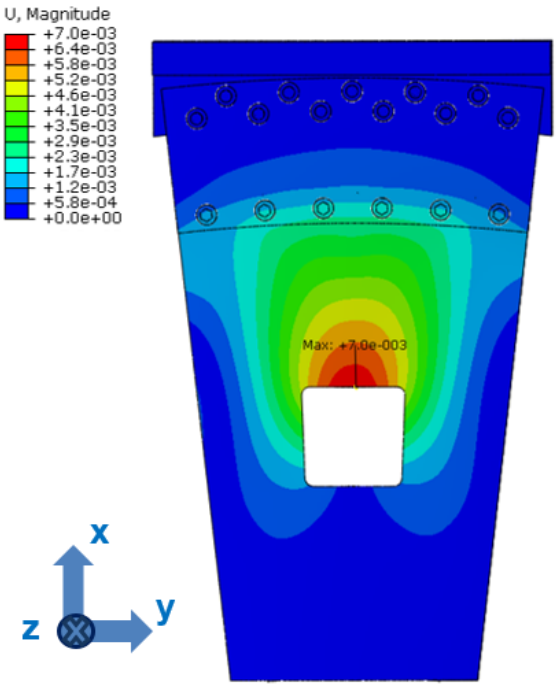

(b) Reaction force 57 kN: end of the analysis .

Figure H.3: Out-of-plane displacement fields of the panel model for two reaction forces measured at the test fixture.

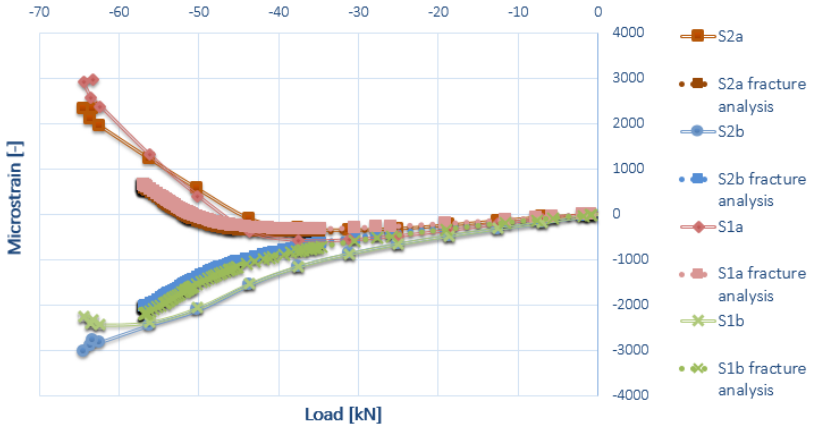

(a) Single strain gauges S1 and S2 results results .

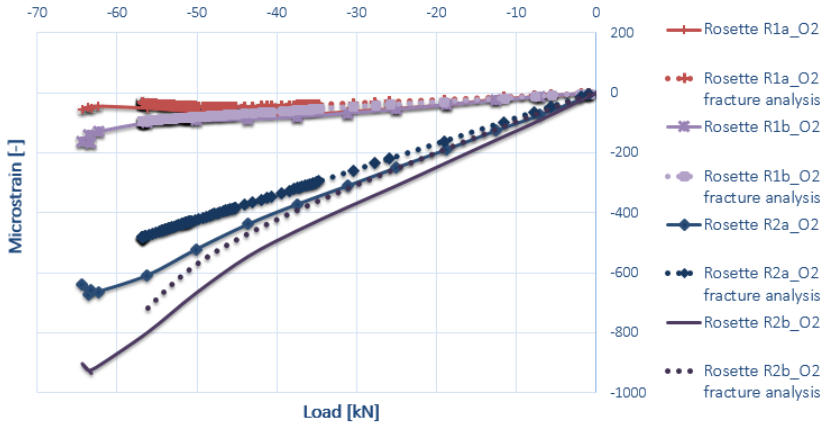

(b) Strain gauges rosettes R1 and R2 along the O2 axis .

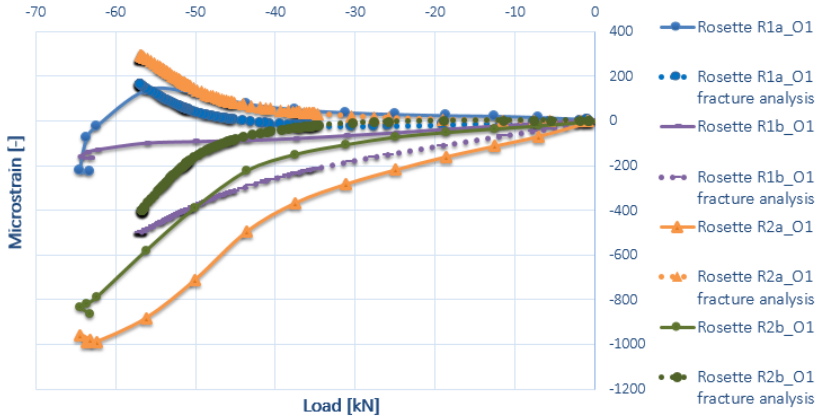

(c) Strain gauges rosettes R1 and R2 along the O1 axis .

Figure H.4: Strain analysis results of the panel model, for the single strain gauges and strain gauges rosettes. "a" indicates the panel stiffeners' side and "b" the opposite side (see Figure 7.4 for the gauges positions and reference orientations).

BIBLIOGRAPHY

[1] P. Feraboli, F. Deleo, B. Wade, M. Rassaian, M. Higgins, A. Byar, M. Reggiani, A. Bonfatti, L. DeOto, and A. Masini, *Predictive modeling of an energy-absorbing sandwich structural concept using the building block approach,* Composites Part A: Applied Science and Manufacturing **41**, 774 (2010).

[2] L. E. Schwer, *Guide for verification and validation in computational solid mechanics,* (2009).

[3] H. Mei, *Fracture and delamination of elastic thin films on compliant substrates: modeling and simulations*, Ph.D. thesis, University of Texas at Austin (2011).

[4] C. Iacomino and S. Ciccarelli, *Potential contributions of commercial actors to space exploration,* Advances in Astronautics Science and Technology **1**, 141 (2018).

[5] K. Schilling, *Perspectives for miniaturized, distributed, networked cooperating systems for space exploration,* Robotics and Autonomous Systems **90**, 118 (2017).

[6] C. Lopes, *Damage and Failure of Non-Conventional Composite Laminates*, Ph.D. thesis, Faculteit Luchtvaart- en Ruimtevaarttechniek, Technische Universiteit Delft (2009).

[7] M. Rouse, D. Jegley, D. McGowan, H. Bush, and W. Waters, *Utilization of the building-block approach in structural mechanics research,* in *46th AIAA/ASME/ASCE/AHS/ASC Structures, Structural Dynamics and Materials Conference* (2005) p. 1874.

[8] M. C. Hill, *Methods and guidelines for effective model calibration,* in *Building Partnerships* (2000) pp. 1–10.

[9] C. Cheyrou, *Literature Report for Damage Models Validation for Composite Materials: Using the Building Block Validation Approach*, Delft University of Technology (2018).

[10] *ABAQUS Version 6.14 User's Manual*, ABAQUS Inc., Pawtucket, RI, USA (2014).

[11] Z. Hashin and A. Rotem, *A fatigue failure criterion for fiber reinforced materials,* Journal of composite materials **7**, 448 (1973).

[12] Z. Hashin, *Failure criteria for unidirectional fiber composites,* Journal of applied mechanics **47**, 329 (1980).

[13] M. Kenane and M. Benzeggagh, *Mixed-mode delamination fracture toughness of unidirectional glass/epoxy composites under fatigue loading,* Composites Science and Technology **57**, 597 (1997).

[14] M. S. Martis, *Validation of simulation based models: a theoretical outlook,* The electronic journal of business research methods **4**, 39 (2006).

[15] *Standard Test Method for Compressive Properties of Polymer Matrix Composite Materials with Unsupported Gage Section by Shear Loading*, ASTM International (2003).

[16] *Compression Testing of Textile Composite Materials*, National Aeronautics and Space Administration (1996).

[17] *Standard Test Method for In-Plane Shear Response of Polymer Matrix Composite Materials by Tensile Test of a ± 45° Laminate*, ASTM International (1995).

[18] D. Lekou and T. Philippidis, *Mechanical property variability in frp laminates and its effect on failure prediction,* Composites Part B: Engineering **39**, 1247 (2008).

[19] D. R. Hufner and M. L. Accorsi, *A progressive failure theory for woven polymer-based composites subjected to dynamic loading,* Composite Structures **89**, 177 (2009).

[20] H. Jeong and R. Shenoi, *Probabilistic strength analysis of rectangular frp plates using monte carlo simulation,* Computers & Structures **76**, 219 (2000).

[21] S. Carbillet, F. Richard, *et al.*, *Reliability indicator for layered composites with strongly non-linear behaviour,* Composites Science and Technology **69**, 81 (2009).

[22] *Standard Test Method for Open-Hole Compressive Strength of Polymer Matrix Composite Laminates*, ASTM International (2014).

[23] B. Chen, T. Tay, P. Baiz, and S. Pinho, *Numerical analysis of size effects on open-hole tensile composite laminates,* Composites Part A: Applied Science and Manufacturing **47**, 52 (2013).

[24] I. HYDER, J. SCHAEFER, B. JUSTUSSON, S. WANTHAL, F. LEONE, and C. ROSE, *Assessment of intralaminar progressive damage and failure analysis methods using an efficient evaluation framework,* in *Proceedings of the American Society for Composites—Thirty-second Technical Conference* (2017).

[25] *Standard Test Method for Short-Beam Strength of Polymer Matrix Composite Materials and Their Laminates*, ASTM International (2000).

[26] M. Moslemi and M. Khoshravan, *Cohesive zone parameters selection for mode-i prediction of interfacial delamination.* Strojniski Vestnik/Journal of Mechanical Engineering **61** (2015).

[27] A. S. for Testing and M. (Filadelfia), *Standard test method for mode i interlaminar fracture toughness of unidirectional fiber-reinforced polymer matrix composites,* (ASTM, 1994).

[28] J. E. Shigley, *Mechanical Engineering Design* (McGraw-Hill, 1977) p. 438.

[29] P. Krolo, D. Grandić, and M. Bulić, *The guidelines for modelling the preloading bolts in the structural connection using finite element methods,* Journal of Computational Engineering **2016** (2016).

[30] L. Cheng and G. Y. Tian, *Comparison of nondestructive testing methods on detection of delaminations in composites,* Journal of Sensors **2012** (2012).

[31] A. Fahr and A. Y. Kandeil, *Ultrasonic c-scan inspection of composite materials,* Engineering Journal of Qatar University **5** (1992).

[32] Y. Shi, T. Swait, and C. Soutis, *Modelling damage evolution in composite laminates subjected to low velocity impact,* Composite Structures **94**, 2902 (2012).